CREVICE CORROSION IN NICKEL ALLOY 625 IN AN OCEAN WATER ENVIRONMENT

A Dissertation
Presented to
The Graduate Faculty of The University of Akron

In Partial Fulfillment
Of the Requirements for the Degree
Doctor of Philosophy

Diana Muñoz Salgado
December, 2017

CREVICE CORROSION IN NICKEL ALLOY 625 IN AN OCEAN WATER ENVIRONMENT

Diana Muñoz Salgado

Dissertation

Approved:	Accepted:
Advisor Dr. Scott Lillard	Department Chair Dr. Michael Cheung
Committee Member Dr. Kevin Kreider	Dean of the College Dr. Donald Visco, Jr.
Committee Member Dr. Rajeev Gupta	Dean of the Graduate School Dr. Chand Midha
Committee Member Dr. Hongbo Cong	Date
Committee Member Dr. Gregory Morscher	

ABSTRACT

In crevice corrosion, the development of a critical crevice solution (CCS) plays an important role in crevice corrosion propagation in nickel alloy 625. In this study CCSs were made from $NiCl_2$, $CrCl_3$, $FeCl_2$, $MoCl_3$, and $NbCl_5$ metal salts following the same stoichiometric ratio as they appear in the alloy and ranging in concentration from 3.0 to 5.0 molal (m). From anodic cyclic potentiodynamic polarization results, it was found that minor elements such as Mo and Nb contributed to lower open circuit potentials (OCP) and increased critical peak current densities (i_{crit}). Solutions that simulated an equivalent chloride content similar to that of the NiCrFeMoNb solutions, but without any Mo and Nb content, presented high OCP values and passive behavior. The active to passive transition in the polarization curves appeared to correlate with a critical concentration of Mo^{3+} in solution, i.e. at $[Mo^{3+}] > 0.09$ m activation occurred. The properties of these CCSs were compared with simulations using OLI software to predict the solution pH and the solid species that precipitate at 25°C. It was found that for concentrations ranging from 3.0 to 5.0 m, all metal solutions presented pH values below 0. Additionally, HCl-based solutions within the range of 0.1 to 5.6 m were studied, and it was found that the i_{crit} values in these solutions were typically lower than in the metal salt solutions at an equivalent pH. This study also presents an equation for preparing HCl solutions to obtain an equivalent i_{crit} to that of the NiCrFeMoNb solutions.

A proposed mechanism for crevice corrosion damage evolution of remote crevice assemblies (RCAs) of nickel alloy 625 exposed to artificial ocean water under anodic potentiostatic control was also presented. Based upon the crevice corrosion morphology, the current vs time (*I vs t*) curves, and the analysis of corroded area over time, it was found that crevice corrosion occurred in three different stages:

Stage I – *CCS development and initiation of crevice corrosion*. During Stage I, two important subsequent events occur: (*i*) the deoxygenation within the crevice and (*ii*) the initiation of crevice corrosion. For an RCA polarized at 200 mV vs SCE, the deoxygenation event was calculated to occur in less than 10 min. Additionally, during this stage, visible damage was minimal, characterized by light etching beginning at the furthest point from the crevice mouth.

Stage II – *Movement of the active front*. During Stage II, the anodic dissolution rate (current) increased and was found to be dependent of the applied potential. The light etching damage moved from the deepest part of the crevice towards the mouth until it reached a critical distance near the crevice mouth (x_{crit}).

Stage III – *Stable crevice corrosion propagation*. Once a critical location from the mouth (x_{crit}) is reached, crevice corrosion propagation rates increase drastically and severe damage (with increased penetration depth) occurs. During this final stage, the current remains constant at an I_{lim} value, and brightened surfaces and deepening damage are observed.

A modified T.H.E. (Tsujikawa-Hisamatsu-Electrochemical) method was used for evaluating crevice corrosion repassivation potentials ($E_{rp,crev}$) in the RCAs. It was found that there is a dependence of $E_{rp,crev}$ on the propagation time and location of x_{crit}. At early times, when the extent of crevice corrosion damage is small and x_{crit} is far from the crevice mouth, the $E_{rp,crev}$ values for 12 and 24 hours were found to be 80 and 150 mV vs SCE, respectively. Once x_{crit} was reached and crevice corrosion transitioned to stage III, $E_{rp,crev}$ stayed at a constant value: for both 36 and 72 hour immersion times, $E_{rp,crev}$ was 190 mV vs SCE.

Additionally, crevice corrosion products were examined at different immersion times during the crevice corrosion process. From Energy Dispersive Spectroscopy (EDS) and Inductively Coupled Plasma (ICP) analyses of the crevice corrosion products and bulk solution, it was found that, over time, the products within the crevice became enriched in O, Mo, and Nb, while the crevice corrosion products formed around the mouth of the crevice (outside of the crevice) became enriched in Ni, Cr, Fe, Mo, and O content. These results suggest that the metal cations diffusing out of the crevice form oxide/hydroxide precipitates due to the drastic pH change from the acidic conditions inside the crevice to the more neutral/alkaline bulk solution at the crevice mouth. The absence of Nb content in the corrosion products outside of the crevice suggests that the Nb exists as a stable precipitate inside the crevice, likely Nb_2O_5.

Finally, X-ray Computed Tomography (X-CT) was used to measure the crevice gap in the RCAs. It was found that the crevice gap varied within a range of 30 to 50 μm. The measurement of the crevice gap allowed the calculation of the *IR*-drop down the length of the crevice. It was found that the *IR* drop is small, and remains nearly constant during the crevice corrosion process.

This work is divided into 4 main chapters. Chapter I is a comprehensive review of the literature regarding crevice corrosion of stainless steels and nickel alloys, especially nickel alloy 625. In this literature review, the different theories for understanding crevice corrosion initiation and propagation mechanisms are described, along with models for predicting pH of highly concentrated solutions, such as critical crevice solutions found within crevices. Chapter II presents in detail the experimental set up and electrochemical techniques used for studying crevice corrosion initiation and propagation stages in this study. Chapter III displays the primary results of the study, which are then discussed in Chapter IV. Chapter V presents the conclusions drawn from this study, addressing the crevice corrosion propagation stage in RCAs, and the effect of metal cations in artificial crevice solutions.

DEDICATION

To my parents, siblings, and to my husband.

ACKNOWLEDGEMENTS

I would like to thank my advisor, **Dr. Scott Lillard**, for motiving me, pushing me to think critically, and providing me the opportunity to challenge myself and grow as a corrosion engineer over the past 4 years. You have been an excellent role model for me, I look up to you and consider myself very lucky to have had you as my advisor.

I want also to thank my committee members, **Drs. Kevin Kreider**, **Hongbo Cong**, **Rajeev Gupta**, and **Gregory Morscher**, for their time and attention during the academic milestones of my candidacy and for the interesting ideas that they have exposed me to during the discussions and classes that I have taken with them.

I would like to thank my colleagues **Andrew Moran**, **Javier Esquivel**, **Elmira Ghanbari**, **Lizeth Sanchez**, **Benjamin Clark**, for the fun that we had together as we struggle to our research and celebrated our achievements.

I am very grateful to **William Imes** for machining materials that I need to conduct my research, for providing practical advice and for being a good friend.

I want to thank my family: my parents, **Luz Stella Salgado** and **Alfredo Muñoz Vargas**, and my siblings, **Jully**, **Andres** and **Lina**. Your love and support has given me the opportunity and the strength to make this dream of mine come true.

Finally, I would like to thank my husband, **Zachary Miller**, for all the proofreading, for dealing with my stress, and for being there for me throughout my studies and research at the University of Akron. I cannot imagine having done this without you by my side.

TABLE OF CONTENTS

LIST OF TABLES

LIST OF FIGURES

LIST OF ABBREVIATIONS

CCS: *Critical Crevice Solution*
CPP: *Cyclic Potentiodynamic Polarization*
CRA: *Corrosion Resistant Alloy*
E_{corr}: *Corrosion Potential*
E_{crev}: *Crevice Potential*
E_{crit}: *Critical potential at which i_{crit} occurs*
EDS: *Energy Dispersive Spectroscopy*
$E_{rp,crev}$: *Crevice Repassivation Potential*
E_{rp}: *Repassivation Potential*
FCC: *Face-Centered Cubic (lattice structure)*
i_{corr}: *Corrosion Current Density*
ICP: *Inductively Coupled Plasma*
i_{crit}: *Critical Peak Current Density*
i_{pass}: *Passive Current Density*
i_{crit} or i_{peak}: *Critical Current Density or Peak Current Density*
IR*: *Critical Potential Drop*
IR: *Potential Drop*
MCA: *Multiple Crevice Assembly*
MSE: *Mixed Solvent Electrolyte*
NiCrFe: *Stoichiometric solution containing $NiCl_2$, $CrCl_3$ and $FeCl_2$ in solution.*
NiCrFeMo: *Stoichiometric solution containing $NiCl_2$, $CrCl_3$, $MoCl_3$ and $FeCl_2$ in solution.*
NiCrFeMoNb: *Stoichiometric solution containing $NiCl_2$, $CrCl_3$, $FeCl_2$, $MoCl_3$ and $NbCl_5$ in solution.*
OCP: *Open Circuit Potential*
RCA: *Remote Crevice Assembly*
SCC: *Stress Corrosion Cracking*
SCE: *Saturated Calomel Electrode*
T.H.E.: *Tsujikawa-Hisamatsu Electrochemical Method*
UNS: *Unified Numbering System*
x_{crit}: *Critical Distance Near the Crevice Mouth*
X-CT: *X-ray Computed Tomography*
η: *Overpotential*

I. BACKGROUND

1.1. Nickel alloys and Passivity

Passive alloys, such as stainless steels and nickel alloys, owe their corrosion resistance to their ability to form a protective passive film [1]–[3]. However, these alloys are susceptible to localized corrosion if the protective passive film is damaged or breaks down [4]. Localized corrosion occurs at faster rates than uniform/general corrosion and, in most cases, cannot be easily detected [5]. Types of localized attack include pitting, crevice corrosion, and stress corrosion cracking (SCC) [6].

The composition of an alloy determines its degree of passivity. The addition of chromium to iron creates many different alloys categorized as stainless steels, e.g. an addition of chromium greater than 13 wt% to iron significantly improves the corrosion resistance of the alloy [7], [8]. The addition of chromium and molybdenum in nickel has also been found to promote passivity and has led to the creation of different NiCrMo alloys [9], [10]. As summarized by Sequeira et al. [10] in their review, nickel and nickel alloys are resistant to corrosion in a wide variety of natural and industrial corrosive environments. The most common nickel alloys used in industry are known by their commercial names such as Hastelloy, Inconel, Monel, and Incoloy, although they have a unique unified numbering system (UNS) number as well. Nickel alloys are usually divided in two groups: high temperature alloys and corrosion resistant alloys. The high temperature alloys are designed to withstand high temperatures and dry/gaseous corrosion, while corrosion resistant alloys (CRAs) are designed to have superior resistance to aqueous corrosion within a moderate range of temperatures [10]. CRAs can be grouped according to their chemical composition: commercially pure Ni, Ni-Cu alloys, Ni-Mo alloys, Ni-Cr-Mo alloys, and Ni-Cr-Fe alloys. Ni-Cu and Ni-Mo alloys do not passivate under oxidizing conditions due to the absence of Cr content. Alloys such as Ni-Cr-Fe and Ni-Cr-Mo do form a passive film under oxidizing conditions, and are considered multipurpose alloys that can be used both in reducing and oxidizing conditions. All of these alloys still retain the face-centered cubic (FCC) lattice structure of the Ni base element, which is the main element responsible for properties such as excellent ductility, malleability, and formability [11]. Nickel alloys are more expensive than stainless steels, and are used only in environments where stainless steels are not suitable.

1.1.1. Nickel Alloy 625

Alloy 625 is widely used in aerospace, chemical, petrochemical, marine service, and nuclear industries for applications where resistance to corrosion and heat are necessary [12]–[18]. The nominal composition of nickel alloy 625 (UNS N06625) is given in Table 1.

Table 1. Chemical composition of nickel alloy 625

Element	wt %	Element	wt %
Ni	58.0 min	**S**	0.015 max
Cr	20.0 -23.0	**Al**	0.40 max
Fe	5.0 max	**C**	0.10 max
Mo	8.0 – 10.0	**Mn**	0.50 max
Nb+Ta	3.15 – 4.15	**Si**	0.50 max
P	0.015 max	**Ti**	0.40 max

The excellent corrosion resistance of this alloy has been attributed to the combined effect of its Cr (20-23 wt %) and Mo (8-10 wt %) content [13], [15], [19]–[24]. Cr and Mo are known to impart high corrosion resistance against both oxidizing and reducing environments [23], [25]. Surface analyses of the passive film formed on alloy 625 suggested the presence of a thick oxide layer structure consisting of an inner Cr–Ni oxide layer and an outer Mo/Cr oxide layer [26]. Lower passive currents are attributed mainly to the Cr-Ni layer; however, after a breakdown event occurs, the presence of Mo in the outer layer helps to maintain low passive currents, suppressing localized corrosion [8], [26]–[29]. Nickel alloy 625's niobium content (Nb ~4wt %) has also been reported to contribute to corrosion resistance; higher Nb content lowers the passive current density values [13].

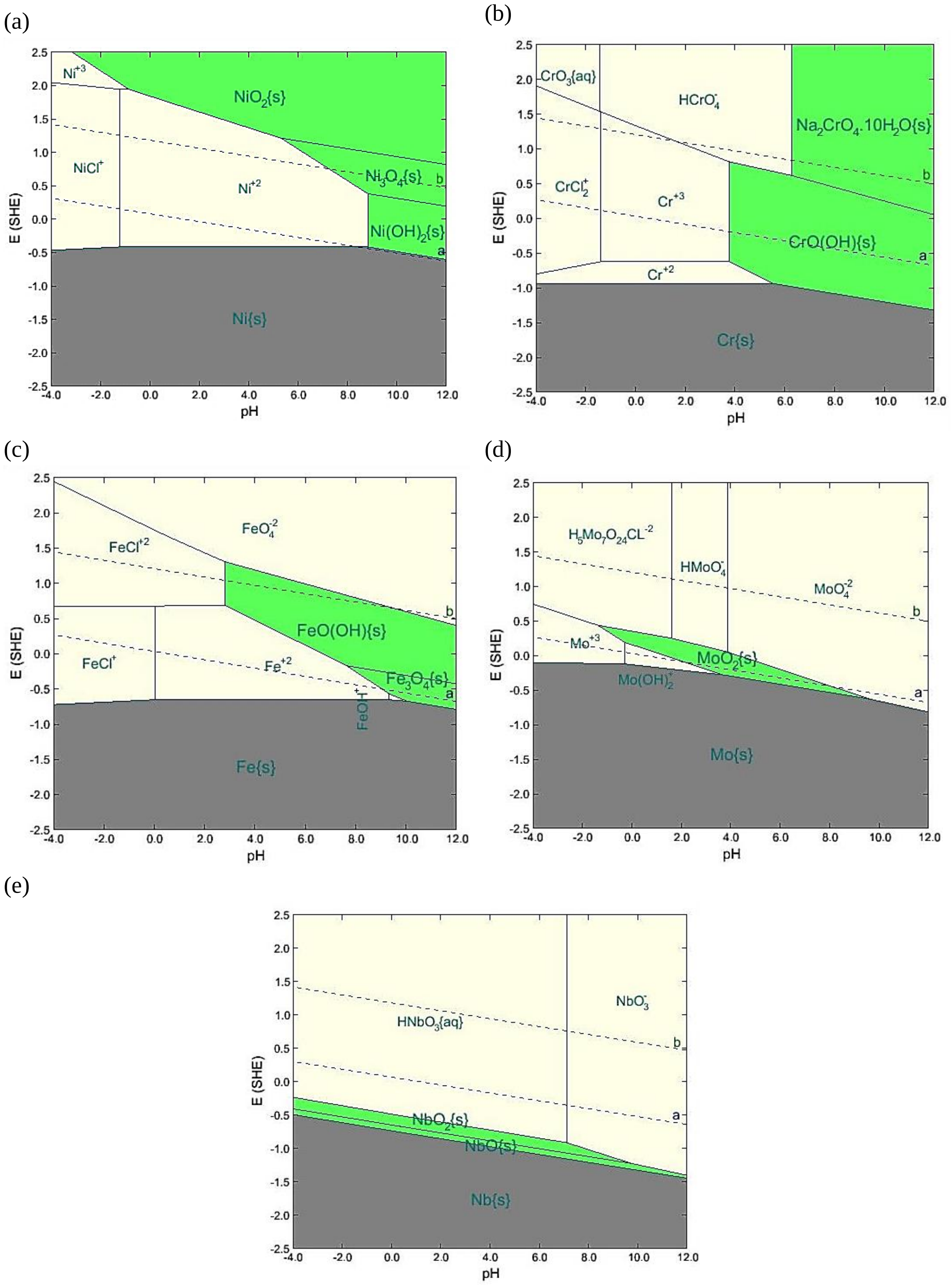

Figure 1. E-pH diagram of (a) Ni, (b) Cr, (c) Fe, (d) Mo and (e) Nb in 1 M NaCl solution at 25ºC. Calculated with Stream Analyzer in OLI software. The activity of trace species is set to 1×10^{-6} m.

Alloy 625 generally has excellent resistance to pitting corrosion, but has been found to be susceptible to crevice corrosion in freshwater and seawater [22], [30]. This susceptibility has been attributed to the formation of an aggressive environment (low pH and high Cl^- content) within the crevice. To evaluate the potential and pH at which nickel alloy losses its passivity, E vs pH diagrams for the main components of nickel alloy 625 in 1 M NaCl at 25˚C are shown in Figure 1. As seen in Figure 1, at potentials above 0 V vs SHE and below 0 pH (characteristic reducing conditions found within a crevice) the most stable oxidation states for Ni, Cr, Fe and Mo are 2+, 3+, 2+, and 3+, respectively, as metal cations. In the case of Nb the most stable oxidation state is 5+ as Nb_2O_5.

1.2. Pitting Corrosion

Passivity and pitting corrosion are closely related to crevice corrosion. Understanding these phenomena help to elucidate the mechanism of crevice corrosion.

Passivity is defined as the state of low corrosion rates under a high anodic driving force or overpotential. These low rates are due to the formation of a thin oxide/hydroxide passive film on the metal surface. The passive state can be explained using a typical potentiodynamic polarization curve, see Figure 2. As the overpotential (η) increases in the anodic direction from $E_{corr,}$ the driving force towards oxidation increases and the rate of oxidation also increases. This increase in oxidation currents typically follows a Tafel behavior (range A-B in Figure 2). At point B, the critical anodic dissolution current (i_{crit}) and the potential of the active to passive transition (E_{crit}) (sometimes referred to as the Flade potential) are reached. When a critical overpotential is reached (E_{crit}), a dramatic decrease in the oxidation current occurs, and the rate of anodic dissolution remains low as the overpotential continues to increase, a low passive current density is reached and becomes nearly independent of potential i.e. the alloy/metal reaches a passive state. Once the overpotential reaches a sufficiently high value, the passive film breaks down and transpassive dissolution of the oxide film occurs (range C-D in Figure 2).

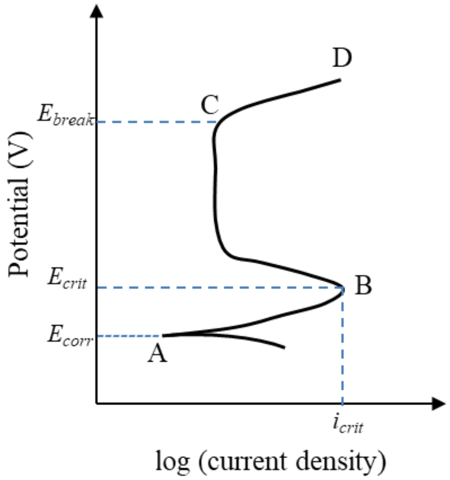

Figure 2. A schematic diagram of a potentiodynamic polarization curve.

Pitting corrosion mostly affects metals which are in the passive state, and occurs in electrolytes containing a critical concentration of halide ions, Cl^- being the most common [31], [32]. Initially, within a pit, the rapid anodic dissolution process increases the metal cation concentration and the pH decreases mainly due to hydrolysis reactions of metal cations, see Equations 1 and 2. Chloride anions migrate into the pit to maintain charge neutrality, making the pit solution more aggressive and causing autocatalytic pit propagation and growth.

$$Me \rightarrow Me^{n+} + ne^- \qquad \text{Equation 1}$$

$$Me^{n+} + H_2O \rightarrow MeOH^+ + H^+ \qquad \text{Equation 2}$$

From anodic polarization curves for studying pitting corrosion (Figure 3), two characteristic potentials had been identified: the pitting potential, E_{pit}, represented by an increase of the current, and the repassivation potential, E_{rp}, represented by a drop in current due to pit repassivation.

Several authors have proposed different definitions for E_{pit}: (1) the potential above which stable pits propagate, (2) the minimum potential to maintain a salt film inside a pit [33], (3) the minimum potential at which pit solution composition is aggressive enough to keep the passive film locally unstable and thus prevent repassivation [34], or (4) a minimum potential needed for metastable pits to become stable [35]. E_{rp} is defined as the potential below which no metastable or stable pitting occurs, and above which metastable pits can form and already existing pits can propagate [36]. It has been also suggested that E_{rp} is the minimum required potential to maintain the critical environment inside of a propagating pit [37].

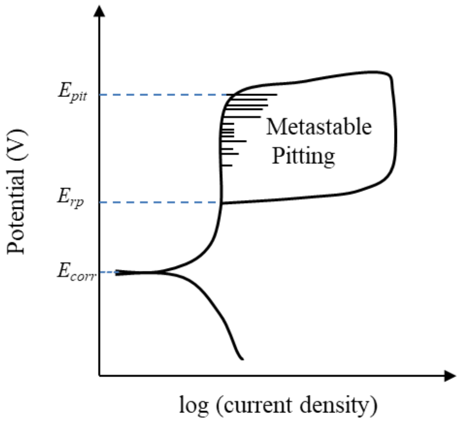

Figure 3. A schematic diagram of a potentiodynamic polarization curve indicating the pitting (E_{pit}) and repassivation potential (E_{rp}).

Gaudet et al. [44] presents at a clear description of the current vs overpotential characteristics found in an artificial pit, which is summarized in Figure 4. In Region I (the activation-controlled region), the anodic dissolution currents are low, and all of the potential is consumed at the metal/solution interface. The anodic dissolution can be predicted by Tafel's law as follows:

$$\eta = a \ln i + b \qquad \text{Equation 3}$$

where a and b are constants and η is the overpotential.

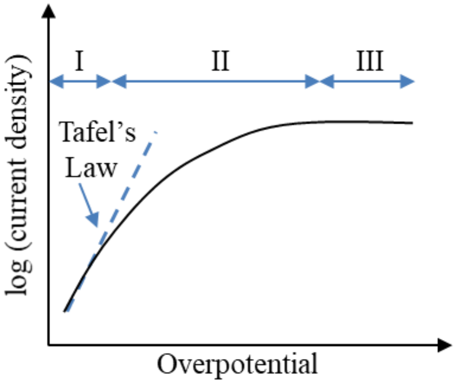

Figure 4. Regions of electrochemical reactions. I. Activation-controlled region, II. IR-controlled region and III. Diffusion controlled region. Taken and modified from Ref. [38]

As the overpotential increases, the anodic dissolution current increases exponentially, as is depicted in Region II. In this region, the IR-drop, given by the solution resistance, needs to be considered. Thus, in region II, the overpotential is consumed by metal/solution interface reactions and the solution resistance, and can be calculated as follows:

$$\eta = a \ln i + b + IR \qquad \text{Equation 4}$$

where R is the solution resistance.

At some point, further increase in the overpotential causes the supersaturation of metal cations in solution resulting in the precipitation of a salt film on the surface of the pit. At this point, the anodic dissolution becomes limited by diffusion and independent of overpotential, as is shown in Region III.

A localized acidification model for explaining pit propagation was proposed by Galvele [39]. This model assumed that metal dissolution at the pit bottom was followed by hydrolysis reactions, allowing the calculation of the minimum degree of acidification (pH_{crit}) to avoid pit repassivation. pH_{crit} corresponds to a critical value of the product of pit depth (x) and pit current density (i) needed for sustained pit dissolution. If there are $(x.i)$ values resulting in a pH lower than pH_{crit}, pits will propagate.

1.3. Crevice Corrosion

Crevice corrosion is a form of localized attack that affects even materials that are otherwise very resistant to corrosion, such as stainless steels, nickel-based alloys, aluminum alloys, and titanium alloys in aerated chloride environments [40]. This type of corrosion occurs in occluded regions characterized by a large aspect (depth-to-gap) ratio and a crevice gap wide enough (a few micrometers) to allow liquid entry but sufficiently narrow to maintain stagnant conditions [41], see Figure 5. These requirements are easily met in natural conditions and are frequently present in engineering equipment and structures. Flange pipes in chemical processing plants, lap joints in aircrafts, and metal surfaces under disbonded coatings are a few examples of occluded regions that may form in metallic engineering structures, inviting susceptibility to crevice corrosion damage . [42], [43]. Within natural conditions, depositions of dirt, dust, corrosion products, and biofouling organisms, among others, can act like a shield, creating the conditions necessary for crevice corrosion to occur.

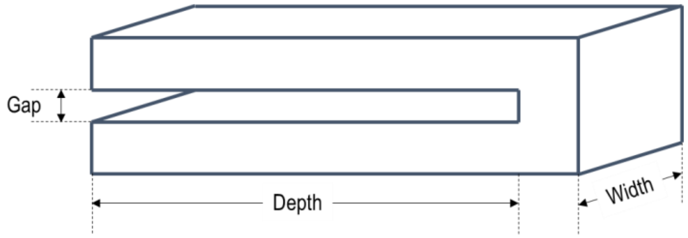

Figure 5. Crevice with respective dimensions. Aspect ratio is defined as depth/gap ratio.

Fontana and Green provided a qualitative explanation for initiation and propagation of a creviced metal/alloy exposed to an aerated, neutral pH and Cl^--containing environment [43]. Initially, oxidation and reduction reactions occur uniformly in the external and internal surfaces of the crevice. Due to the restricted diffusion within the occluded region, the oxygen depletes over time until the oxidation reaction can no longer occur inside the crevice. Dissolution of the metal inside the crevice continues to occur at a rate given by the passive current, i_{pass}. Due to transport restrictions caused by the geometry of the crevice, the metal cations produced by passive dissolution cannot be transported out of the crevice at a sufficient rate to prevent an accumulation of metal cations within the crevice. To preserve electroneutrality within the crevice, chloride ions from the bulk solution migrate into the crevice and subsequently form metallic chlorides, i.e. $Me^{n+} + nCl^- \rightarrow MeCl_n$. Hydrolysis of these metal chlorides results in the formation of both soluble and insoluble oxy-hydroxides and protons, i.e. $MeCl_n + n\,H_2O \rightarrow Me(OH)_n\downarrow + nH^+ + nCl^-$, leading to lower pH-values within the crevice, Figure 6(a). When the concentration of both H^+ and Cl^- increase to a critical concentration, the passive film is no longer stable and active dissolution occurs. The buildup of H^+ and Cl^- ions within the crevice promotes higher rates of corrosion within the crevice, which simultaneously increases the migration of chlorides and the hydrolysis reactions until eventually the corrosion process becomes autocatalytic, see Figure 6(b).

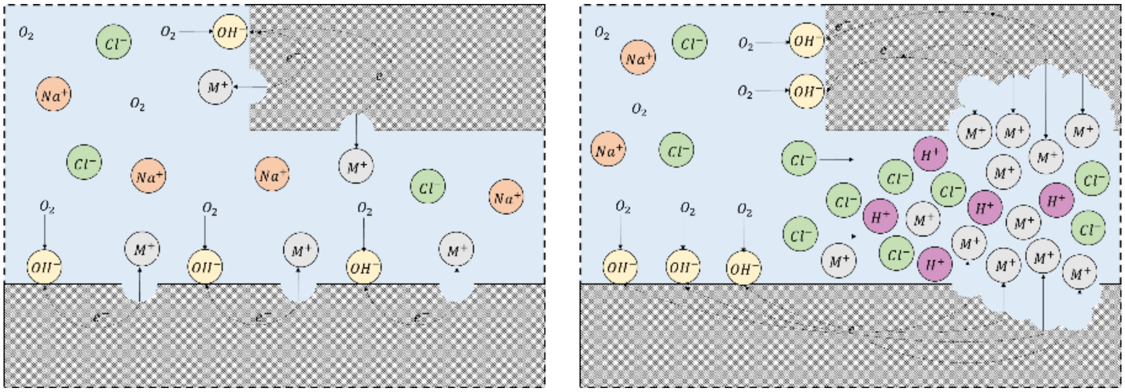

(a) **(b)**

Figure 6. Mechanism of crevice corrosion. (a) Initial stage and (b) Propagation stage.

Following these observations, substantial research has focused on developing a more detailed explanation of crevice corrosion. Two models have been proposed by different authors to describe the phenomenon of crevice corrosion:

1. The critical crevice solution (CCS) model: Development of a CCS.
2. The IR*-model: Development of a critical ohmic potential difference IR*.

1.3.1. *Crevice corrosion models*

1.3.1.1. Critical Crevice Solution (CCS) model

Oldfield and Sutton [44], [45] further developed the Fontana and Green model [43] and presented a more formal crevice corrosion mechanism for stainless steel specimens when exposed to aerated neutral chloride solutions. This mechanism has been extensively used for explaining crevice corrosion initiation and propagation based on the solution chemistry change within crevices. This mechanism consists of an initiation stage, during which a critical crevice solution (CCS) develops over time within the crevice and the attack on the alloy is minimal, and a propagation stage, in which there is a more extensive and severe attack within the crevice, while the external area of the crevice remains passive. According to Oldfield and Sutton, the initiation of the crevice corrosion process is divided into three sub-stages: I) depletion of oxygen, II) hydrolysis-acidification and chloride-migration, and III) formation of a CCS.

Once the crevice corrosion initiates, due to the breakdown of the passive film of the alloy, the propagation stage immediately follows (stage IV). Based on the above stages, Oldfield and Sutton proposed a mathematical model for predicting crevice corrosion initiation in stainless steels. A brief description of the parameters needed in each stage of crevice corrosion initiation and the corresponding outputs of the model are summarized below.

Stage I) Initially, the composition of the solutions inside and outside the crevice are the same. The entire crevice surface, internal and external, passivates, producing a small anodic current (i_{pass}) which transfers metal ions into the surrounding solution. The anodic current is matched by the cathodic current from the reduction of oxygen dissolved into the solution. This exchange takes place all over the surface of the alloy. When these two reactions occur simultaneously, the passive film of the material thickens. These reactions are summarized in Equations 5-7.

$$\boldsymbol{Anode}: M \rightarrow Me^{n+} + n\bar{e} \qquad \text{Equation } 5$$

$$\boldsymbol{Cathode}: H_2O + 2\bar{e} + \frac{1}{2}O_2 \rightarrow 2OH^- \qquad \text{Equation 6}$$

$$\boldsymbol{Overall}: 2M + \frac{n}{2}O_2 + nH_2O \rightarrow 2M(OH)_2 \qquad \text{Equation 7}$$

However, if the crevice specimen has a large aspect ratio (a long path and a narrow gap), the diffusion of oxygen into the crevice becomes slower than its removal via cathodic reaction, and eventually the oxygen in the solution within the crevice is depleted. For Stage I, the Oldfield and Sutton model determines the time of oxygen depletion and the distance into the crevice at which oxygen depletion occurs. It was found that a significant crevice depth must be exceeded for oxygen depletion to occur, as shown in Figure 7. For example, at i_{pass}=1µm/cm^2, the time needed for oxygen depletion was less in a crevice with a 1 µm gap than in a crevice with a 10 µm gap. Based on these results, Oldfield and Sutton identified three important factors governing the deoxygenation stage: passive current value (i_{pass}), oxygen concentration in the bulk solution, and crevice geometry.

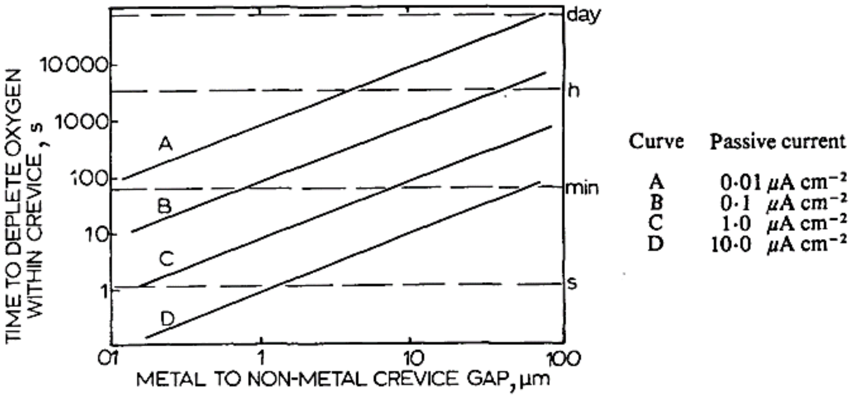

Figure 7.Time to deplete oxygen from within a crevice as function of crevice gap for a series of passive current densities. Taken from Oldfield and Sutton [44].

Stage II) The depletion of oxygen causes the formation of a localized corrosion cell and gives rise to the second stage of the initiation process. The cathodic reaction moves to the external surface while the anodic reaction remains inside the crevice. The anodic reaction continues dissolving material within the crevice, passing cations into the solution that subsequently undergo hydrolysis reactions, producing metal hydroxides. The dissolution of cations into the solution continues until the solubility product of one or more metal hydroxides is exceeded. The precipitation of these metal hydroxides reduces the content of OH^- and increases the concentration of H^+ in the crevice solution, which in turn decreases the pH of the solution. The accumulation of metal cations and the production of H^+ causes the migration of negative charges, in this case chloride anions, into the crevice, and metal cations diffuse out of the crevice in order to reach electroneutrality. Thus, the crevice solution, with low pH and high Cl^-, has become very aggressive towards the passive layer. For Stage II, the mathematical model determines the time required to decrease the pH from its initial value, given by the bulk environment, to the critical value at which the passive film breaks down. The predicted fall in pH over time before the passive film breakdown is shown in Figure 8 for three values of the parameter i_{pass}/x (passive current density / crevice gap). This parameter was chosen by the authors since the fall in pH is directly proportional to i_{pass} and inversely proportional to x. Figure 8 shows that as the ratio i_{pass}/x increases, a longer time for acidification within the crevice is needed. Additionally, as the pH decreases, the Cl^- content of the crevice solution increases.

The factors governing this second stage of the mechanism include the bulk solution composition (*pH* and Cl^- content), the alloy composition (e.g. chromium content, which has been found to decrease the *pH* considerably), and the crevice depth (longer depths facilitate larger concentration gradients).

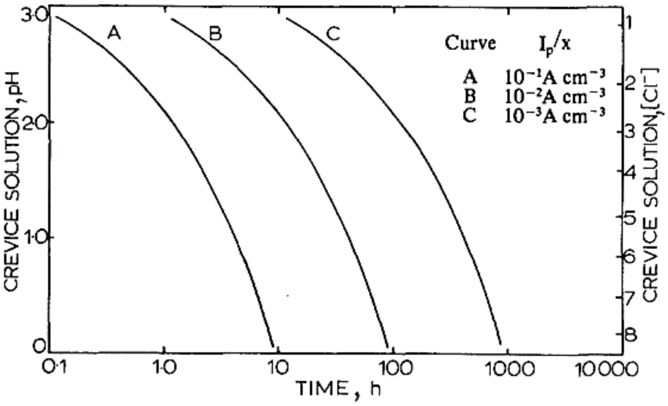

Figure 8. Predicted fall in pH over time in an 18Cr-10Ni-2.5Mo type stainless steel in ambient temperature seawater, assuming the passive film does not breakdown, for three values of the ratio of the passive current to the metal-to-metal crevice gap. Taken from Oldfield and Sutton [44].

Stage III) The critical crevice solution (CCS) forms during the third stage of initiation. In this stage, the solution becomes sufficiently aggressive to cause the breakdown of the passive film on the surfaces inside of the crevice, causing the onset of crevice corrosion. The resistance of the passive layer to aggressive solutions containing high concentrations of metal ions, chloride ions, and hydrogen ions determines the time which is necessary to create a sufficiently aggressive crevice solution. The time taken for the formation of a CCS leads to the concept of incubation time. For Stage III, the Oldfield and Sutton model predicts the time required for breakdown of the passive film and the onset of crevice corrosion. Results of the predicted effect of crevice gap and crevice depth on the onset of the crevice corrosion are summarized in Figure 9. Curves from A to D represent the pH of the CCSs used for the modeling. Above a given curve, crevice corrosion will not initiate, and below the curve crevice corrosion will initiate. For a given pH, as the crevice gap decreases a shorter crevice depth is needed for crevice corrosion to initiate.

For the model, the major parameters affecting the time to breakdown are the composition of the alloy and its associated CCS, passive current values (i_{pass}), the concentration of Cl^- in the bulk solution, and the crevice geometry. This third stage marks the end of the crevice corrosion initiation phase, and leads directly to the propagation of crevice corrosion.

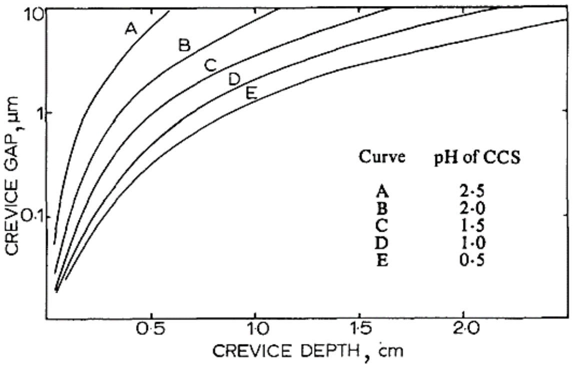

Figure 9. Predicted effect of crevice gap and depth in determining whether crevice corrosion will occur for an 18Cr-10Ni-2.5Mo type stainless steel in ambient temperature seawater assuming a value of $i_{pass}=1\mu A/cm^2$*. Above a given line crevice corrosion will not occur, below the line it will occur. The curves correspond to different pH values of the critical crevice solution (CCS).Taken from Oldfield and Sutton [44].*

Stage IV) Propagation is characterized by the rapid dissolution of the alloy inside the crevice, balanced by the cathodic reactions happening outside the crevice. In a separate study by Oldfield et. al. [46], based on their crevice corrosion immersion tests of alloy 316 in artificial sea water, Oldfield et al. described the propagation stage in terms of another multistage mechanism, as is illustrated in Figure 10. They proposed that after the breakdown of the passive film occurs due to the formation of an aggressive CCS within the crevice, the first stage of crevice corrosion propagation is identified by a rapid increase of the corrosion current, which very quickly becomes limited by the IR voltage drop down the length of the crevice. The second stage of propagation corresponds to the growth of the corroding area moving towards the crevice mouth. During this stage, the current gradually increases until an anodic current limit is reached, indicating that the corroding area has reached the crevice mouth. At the third stage of propagation, the crevice specimen has reached an anodic current limit and rapid corrosion occurs since the reaction now is controlled only by the anodic process within the crevice itself, or by the available cathodic reaction. The fourth and final stage of propagation involves the stifling of crevice corrosion due to the formation of solid corrosion product buildup at the crevice mouth, introducing a resistance between the anodic (internal) and cathodic (external) reactions.

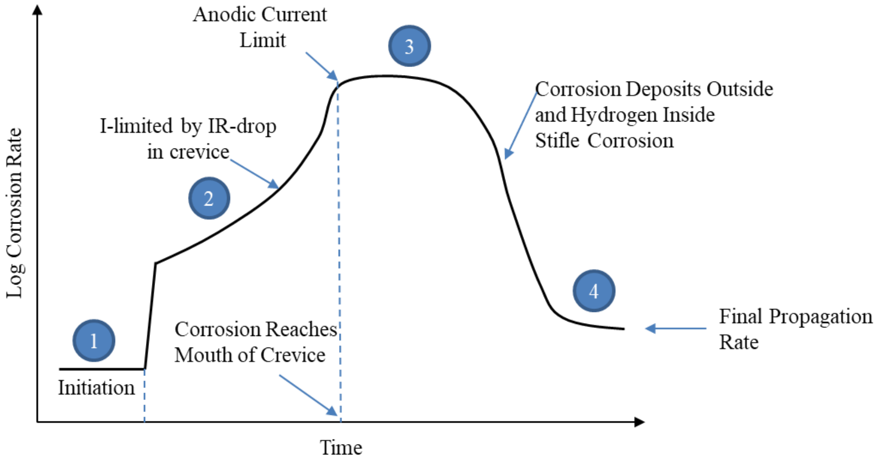

Figure 10. A schematic of the mechanism of crevice corrosion propagation proposed by Oldfield et. al.[46].

Oldfield and Sutton [47] extended the use of their mathematical model for predicting crevice corrosion initiation to more alloys than just 316. They developed a ranking, based on six different materials, covering a wide range of Ni and Mo content, which can be used as guidance for material selection in seawater environments. The ‘times to breakdown’ were used to form the basis of the alloy ranking: the longer the time predicted by the model, the better the alloy’s resistance to crevice corrosion initiation. Severe crevice situations, such as very narrow gaps, long depths, and completely restricted diffusion, were incorporated into the mathematical model together with the alloy and bulk environment’s composition. All alloys were subjected to the same conditions. For each alloy, the passive current (i_{pass}) and the CCS were determined by experimentation and were used as inputs to the model. The passive current supplies metal cations whose hydrolysis causes the pH in the crevice to fall while mass transfer via migration causes the concentration of Cl^- to increase. Eventually, the composition of the crevice solution becomes sufficiently aggressive (i.e. a CCS is formed) and causes the breakdown of the passive film. They defined a CCS as a solution of pH and Cl^- concentration sufficient to produce an anodic current of at least 10 µA/cm^2, and determined that for alloy 625 the critical crevice solution required a pH in the range of -0.25 to 0.50 and 6 M Cl^- [45]. The results of the model gave a ranking of resistance to crevice corrosion initiation, from lowest to the highest. This ranking can help indicate those alloys likely to be immune to crevice corrosion, those which may corrode, and those which will definitely corrode, under the conditions being considered. Based on this ranking, it was found that crevice gap and alloy composition played an important role in crevice corrosion initiation times. Crevice corrosion initiation times decreased when the crevice gap was decreased, meaning that for initiating crevice corrosion in resistant alloys, tighter crevices are needed. Also, it was observed that the effect of individual alloying constituents played a role on crevice corrosion resistance. From the six alloys studied, it was found that Ni, Cr, and Mo content seemed to be beneficial in increasing resistance to crevice corrosion.

Thus, in the Oldfield and Sutton model, the passive current density (i_{pass}) and the crevice geometry (depth-to-gap ratio) are the key parameters that aid the development of a CCS. Their model predicted that, for a constant i_{pass}, the narrower the crevice gap, the shorter the crevice depth required for crevice corrosion initiation. Thus, occluded regions with large depth-to-gap ratios have increased susceptibility to crevice corrosion damage. As depletion of oxygen results from restricted mass transport, crevice corrosion initiates in the region of the crevice furthest from the crevice mouth, and, according to the model, this is where the crevice damage becomes most severe. The Oldfield-Sutton-model does not, however, consider the effect of the *IR*-drop within the crevice (i.e. the electrode-potential variation between the cavity and the outer surface), nor does it predict the rate of the crevice damage that occurs within the crevice.

1.3.1.2. Critical Ohmic Potential Difference (IR) model*

A model based solely on *IR*-drop as the cause for initiation and propagation of crevice corrosion, the *IR**-model, was proposed by Pickering [48], [49]. This mechanism considers the effects of the *IR* drop that exists between the mouth and the sites deeper in the crevice, and the potential distribution of the crevice wall, *E(x)*, that results [50], [51]. This difference in potential is referred to as *IR*-drop. Crevice corrosion occurs when the voltage-drop (*IR*) down the length of the crevice is sufficient to place a portion of the metal in the active region of the polarization curve. This critical value, *IR**, is equal to the difference between the corrosion potential of the boldly exposed surface (E_{corr} or E_{app}) and the critical potential (E_{crit}) (also referred as the passivation potential, E_{pass}), and can be calculated as the product of the peak current density in the active to passive transition (critical current density, i_{crit}) and the crevice resistance ($R=\rho L/A$). This means that at some distance within the crevice, the crevice-wall will reside in the active region where the passivity is destroyed, and active dissolution of the metal occurs. Thus, the criterion for stable crevice corrosion is that $IR > IR^*$.

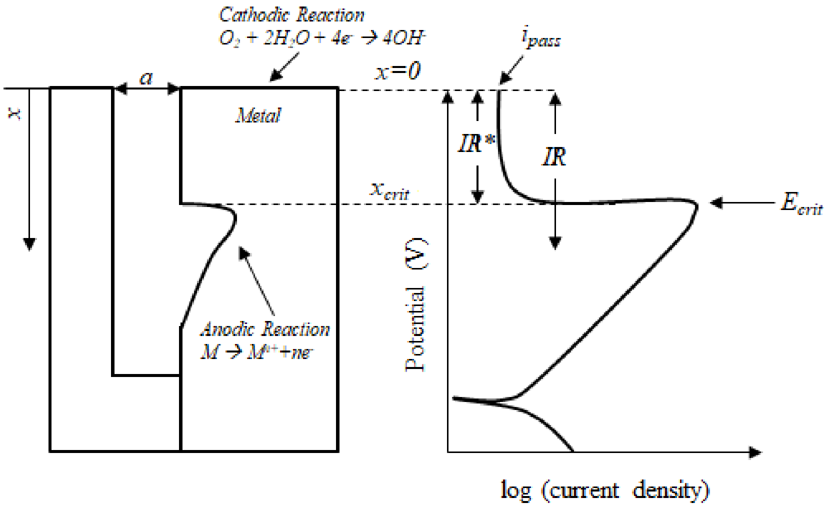

Figure 11. Schematic of a metal with a crevice (left) and its matching polarization curve (right).

The critical requirement for crevice corrosion in the *IR**-model is the presence of an active-to-passive transition in the polarization curve for the material in the bulk environment. While the active dissolution of the cavity occurs at high rates, the outer surface is at a more noble potential (in the passive region) and dissolves at the low passive rate, i_{pass}, in aerated solutions, as is depicted in Figure 11. The distance into the crevice where the potential reaches E_{crit} is referred to as x_{crit}. In theory, the most negative potential that the cavity can reach is given by the mixed potential between the metal oxidation and hydrogen evolution reactions. At this mixed potential, there is not net oxidation current available to flow through the crevice electrolyte to the outer surface, thus without a net current to increase the magnitude of the *IR* voltage, there cannot be further shift of the electrode potential in the negative direction.

Evidence for supporting the *IR*-mechanism, where the electrode potential plays an important role in localized corrosion, was obtained from studies done by Valdes [49]. The system used by Valdes was comprised of an iron specimen mounted in a Plexiglas plate to form a crevice 10 mm deep with an opening 0.5 by 5 mm. A fine Luggin capillary connected to a reference electrode was inserted at different crevice locations in order to obtain the potential gradient from the top to the bottom of the crevice, through the crevice mouth opening. This experimental setup made it possible to directly measure the electrode potential of the cavity, observe the occurrence of electrochemical reactions that only occur at potentials different than that of the outer surface (e.g. hydrogen evolution reaction), and observe the morphology of the crevice damage on the crevice walls, see Figure 12.

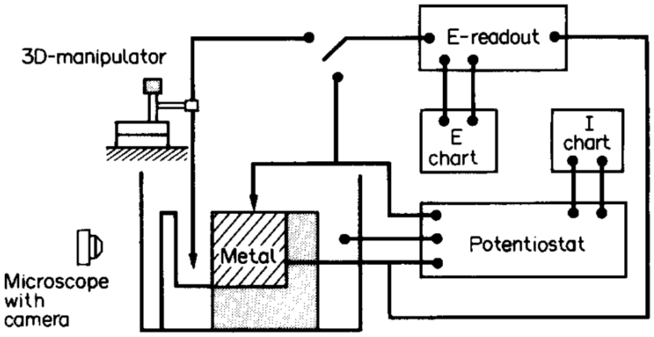

Figure 12. Schematic of the specimen arrangement and experimental setup used by Valdes [50].

Valdes [49] studied four different pH-values, divided into three categories: Acidic solutions (pH 3 and 5), buffered acidic solutions (pH 3 and 5) to minimize acidification within the crevice, and alkaline solutions (pH 9 and 12). Crevice corrosion occurred only in the acidic conditions. Measurement of the crevice electrode potential confirmed that after a critical distance (x_{crit}) was exceeded, the crevice electrode was less oxidizing than E_{crit}. Crevice wall observations also confirmed the formation of an active to passive transition. It was found that the electrode potential at the bottom of the crevice was over 1V less oxidizing that the outer potential (E_{app}), and hydrogen gas bubbles were growing in this region due to the occurrence of the hydrogen evolution reactions (h.e.r). The crevice wall morphology was found to be divided into three different regions: passive, severely attacked, and etched, see Figure 13. The passive region started from the crevice mouth and extended to x_{pass}, i.e. $0 \leq x \leq x_{crit}$; the severely attacked region, where active corrosion occurs, was between x_{crit} and x_{lim}; the lightly etched region extended from x_{lim} to the bottom of the crevice. Crevice corrosion did not occur in the alkaline conditions or in the buffered acidic solutions (pH 3 and 5) – the specimens in these solutions remained passive. The measured electrode potentials everywhere in the crevice were found to be within a few tens of millivolts of the applied potential at the crevice mouth.

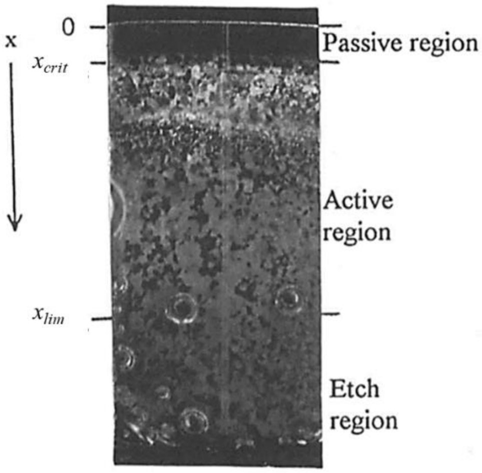

Figure 13. In situ photograph of the iron crevice wall through the Plexiglas with the location of x_{crit} and the different metal dissolution regions, during anodic polarization of the outer surface at 600 mV vs SCE in a buffered acidic solution at pH= 4.6. From Cho et. al [52].

Valdes [49] proposed that the strong pH dependence of E_{crit} and i_{crit} had a direct effect on the IR^* value, and, as a result, affect the $IR>IR^*$ criterion, as is illustrated in Figure 14. In the acidic environment where active corrosion occurred, i_{crit} increased and E_{crit} moved to more oxidizing potentials. Additionally, the crevice geometry provided a large current path, and high currents (in the mA range) were measured. Thus, the IR^* became smaller while the IR down the length of the crevice became larger. Therefore, the $IR>IR^*$ criterion was more easily met in the acidic conditions. The inactivity of crevice corrosion for the alkaline and buffered acidic solutions was attributed to the different polarization response of iron under these conditions. Increasing the pH or the buffer concentration shifts E_{crit} in the less oxidizing direction and decreases i_{crit} (see Figure 14). Thus, alkaline or buffered solutions had a direct effect on increasing the IR^* value. Additionally, the maximum available current in these two environments also decreased, making IR-drop smaller and the $IR>IR^*$ criterion more difficult to be reached.

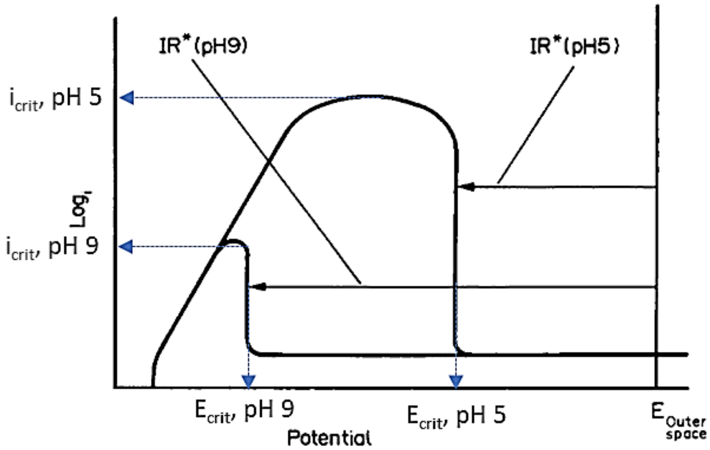

Figure 14. Schematic illustrating the variation of IR as a function of pH since IR* has a strong pH-dependence on E_{crit} and i_{crit}. From Pickering [50].*

Studies evaluating the effect of the applied potential to the outer surface of the crevice [53] and the role of the crevice opening dimension a [54] on the potential distribution within the crevice and its relation to the polarization curve had been studied by Abdulsalam and Pickering [53]. Pure nickel in 1N H_2SO_4 solution at 24°C, a metal/electrolyte system that presents an active/passive peak, was selected for this study, see Figure 15. Abdulsalam and Pickering used an electrochemical cell, similar to the one described in Valdes work [49], with the following dimensions: depth: L=1 cm, width: w=0.5 cm, outer surface: 0.5×2 cm. The solution electrolyte inside the crevice was kept constant during the experiment, so the polarization curve is the same. Thus, the measured polarization curves of the bulk electrolytes are the same as for the crevice electrolytes. The electrode potential and current distributions inside the crevice were measured and calculated respectively.

To study the effect of applied surface potential, E_{app}, on the potential distribution within the crevice ($E(x)$), the outer surface of the crevice specimens were anodically polarized at three different applied potentials (E_{app}), all within the passive region of the nickel/1N H_2SO_4 polarization curve: 250, 300, and 400 mV vs SCE (see Figure 15).

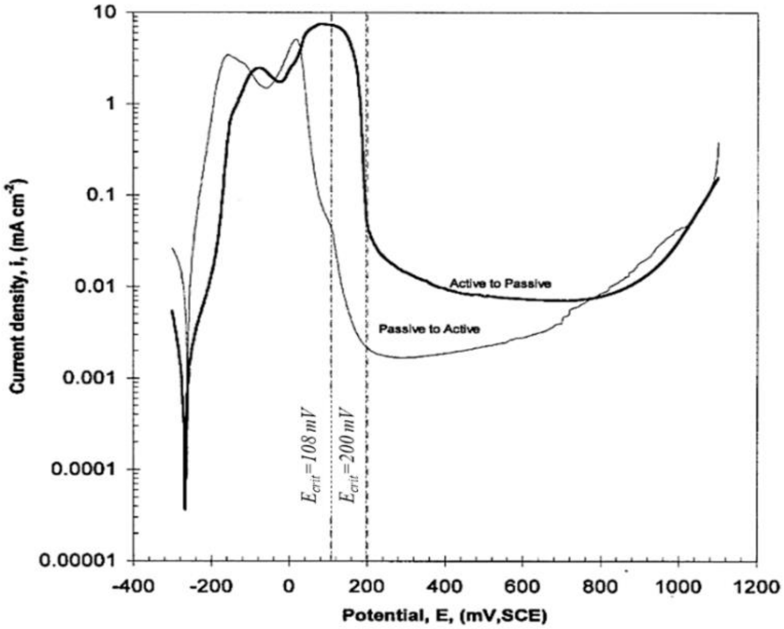

Figure 15. Potentiodynamic polarization curves for Ni in deareated 1 N sulfuric acid at 24°C for scans in the active-to-passive and passive-to-active directions. Scan rate 0.08 mV/s. From Abdulsalam and Pickering [53].

From the electrode potential measurements of the crevice wall, it was found that for all three applied outer potentials, the critical potential (E_{crit}) at x_{crit} was found to be fairly constant with time ($E_{crit} \cong$ 108-112 mV vs SCE), and the x_{crit} location was strongly dependent on the applied potential at the surface E_{app} and very weakly dependent on time (x_{crit} slowly decreases with time) (see Figure 16). From these observations the authors concluded that x_{crit} becomes larger as the potential applied to the outer surface becomes more noble. Thus, x_{crit} was proposed as another way of measuring susceptibility to crevice corrosion. When a low potential is applied to the outer surface (E_{app}), x_{crit} decreases, making a crevice with a given geometry more susceptible to crevice corrosion than the same crevice would be if a higher potential (E_{app}) were applied. At high E_{app}, x_{crit} magnitude increases, making it more difficult to reach the $IR>IR^*$ criterion. From the IR^*-mechanism point of view, higher applied potentials require a long current path to be able to exceed the IR^* necessary for stable crevice corrosion.

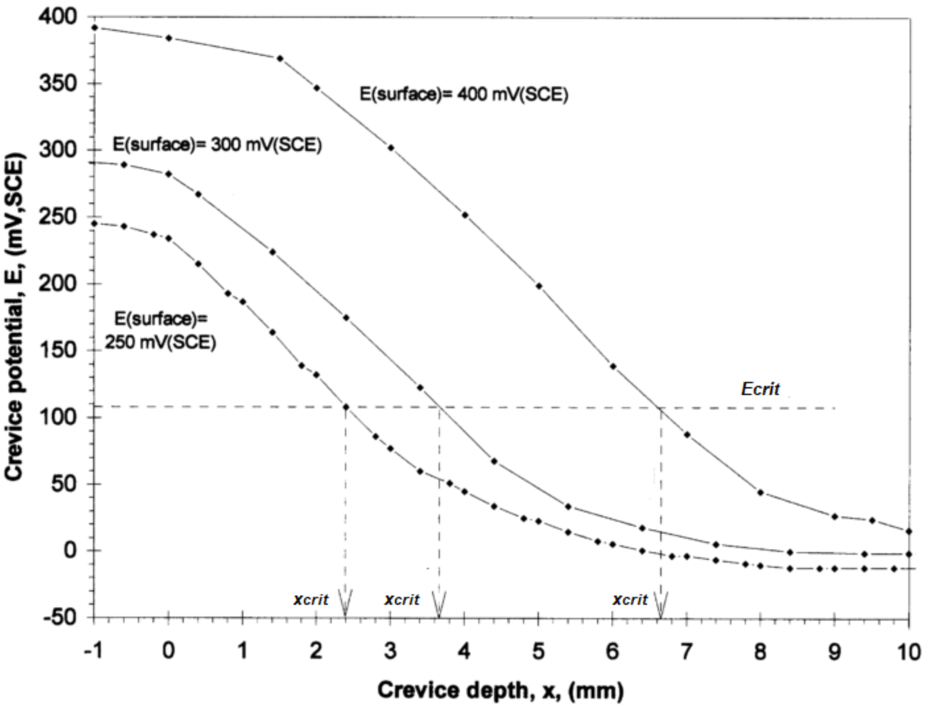

Figure 16. The initially measured potential distributions for the three applied outer surface potentials, x_{crit} is shown by an arrow at the in situ measured $E_{crit} \cong 108$ mV vs SCE. From Abdulsalam and Pickering [53].

The effect of crevice gap on the distribution of potential within the crevice and the stability of crevice corrosion was studied by Abdulsalam and Pickering [54]. Five different crevice gaps were studied, a = 0.5, 0.4, 0.35, 0.25, and 0.165 mm in the Ni/1 N H_2SO_4 system. A single applied potential, i.e. E_{app}=300 mV vs SCE, was used for studying all crevice gaps. The measured electrode potentials obtained are shown in Figure 17. The authors found that crevice gap had a direct effect on the electrode potential distribution ($E(x)$) and the x_{crit} location. As is shown in Figure 17, when decreasing the crevice gap, the x_{crit} location moves towards the crevice mouth; conversely, a wider gap places x_{crit} deeper into the crevice. For crevice gaps $a \geq 0.4$ mm, crevice corrosion did not initiate, and the crevice potential distribution inside the crevice remained at nearly the same applied potential E_{app} = 300 mV vs SCE. From this observation, a crevice gap limiting value a_{lim}, for a given crevice depth and solution composition, was defined as the value above which crevice corrosion does not occur. Based on these observations, the authors proposed that as the aspect ratio (depth/gap) of the crevice increases, i.e. as the crevice becomes more restricted, the resistance R of the crevice solution increases according to the following relationship: $R=\rho L/A$, where A is the cross-sectional area of the crevice. Therefore, as the aspect ratio of the crevice increase, the magnitude of the IR increases, more easily satisfying the $IR>IR^*$ criterion. Additionally, crevices with large depth/gap ratios can place E_{crit} and the corresponding i_{crit} closer to the crevice mouth.

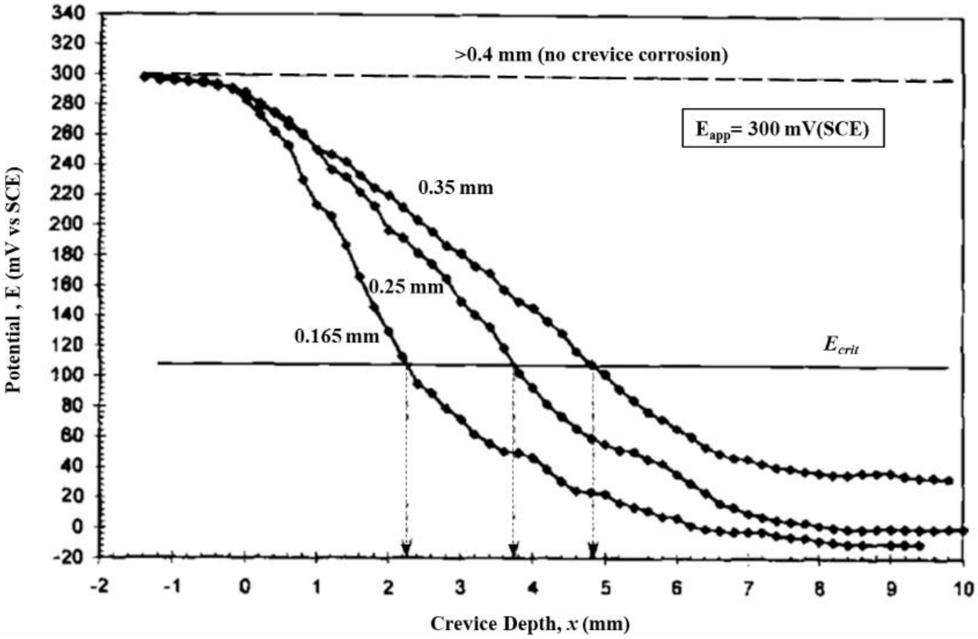

Figure 17. Effect of crevice opening dimension, a, *on the initial potential distribution inside the crevice for Ni in 1N sulfuric acid.* E_{app}*=300 mV vs SCE. From Abdulsalam and Pickering [54].*

In summary, the IR^*-mechanism is affected by several factors such as acidification of the bulk solution, chloride presence, crevice gap, presence of hydrogen bubbles, solid crevice corrosion products, and salt films, to name a few, which increase the likelihood of crevice corrosion [48], [55]. These factors can modify the IR and IR^* magnitudes, enabling crevice corrosion to occur more readily, or to not occur at all. Acidification of the bulk solution facilities the initiation of crevice corrosion as acidification has a direct influence on the critical potential E_{crit}, moving it to more oxidizing potentials and causing the IR^* criterion to be more easily attained [49]. Specifically regarding the effect of chloride ions on the IR^* criterion, it was found that an increased concentration of chloride ions corresponded with an increase in the current flowing out of the crevice, thus causing an increase in IR such that the $IR>IR^*$ criterion for stable crevice corrosion was met more readily [56]. Conversely, alkaline solutions prevented acidification of the crevice electrolyte and had an effect on the polarization response, shifting E_{crit} to less oxidizing values and decreasing i_{crit}, therefore increasing the magnitude of IR^*, making it more difficult to reach the IR required for the $IR>IR^*$ criterion. Generation of hydrogen bubbles were also found to have an influence on the magnitude of IR, since this increases the resistance of the solution R, causing IR to increase.

1.3.1.3. Unification of the CCS and IR models*

The behavior of metal/alloys that do not exhibit an active-to-passive transition in the bulk solution, but do show such behavior when an aggressive chemistry (low pH and high Cl^- content) is developed within the crevice, cannot be explained by either the *CCS* or the *IR**-model alone. Shaw and Moran [28] unified the concepts of the Oldfield-Sutton and Pickering models to explain the crevice corrosion mechanism in alloy 625 using crevice-like solutions and the mixed potential theory. The authors proposed that crevice corrosion in alloy 625 occurred in two stages. (*i*) The development of a CCS inside the crevice that results in a polarization curve with an active-to-passive transition (initiation), and (*ii*) the propagation stage, which occurs if the geometry of the crevice is such that it places a portion of the crevice in the active-to-passive transition of the polarization curve in the crevice environment [57].

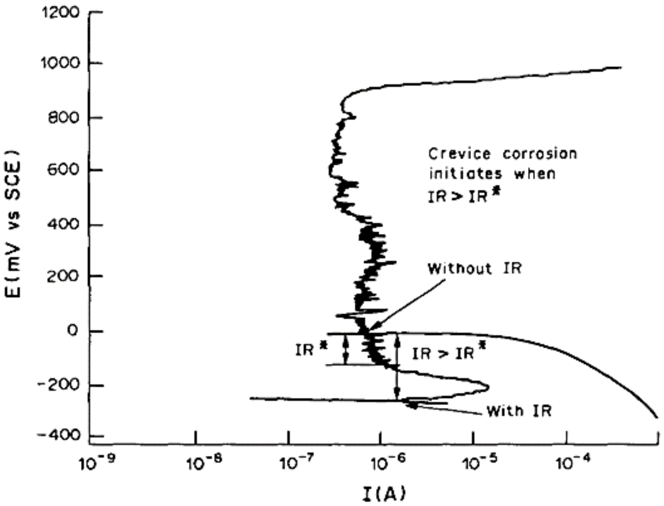

Figure 18. Mixed potential analysis of crevice couple in natural seawater illustrating IR induced crevice corrosion. From Shaw et. al. [28].

Shaw and Moran demonstrated these concepts by generating data for alloy 625 exposed to different artificial crevice solutions simulating the CCS. It was shown that artificial seawater saturated with NaCl and acidified to pH= -0.25 was sufficient to produce an active to passive transition in alloy 625 [28]. Cathodic polarization data was also generated in aerated natural seawater, with pH=8.2 and $[Cl^-]$=0.5 M, to perform the mixed potential analysis (See Figure 18).

Based on Figure 18, the authors proposed that an *IR*-drop through the crevice electrolyte may cause the alloy to reside in the active region of the polarization curve, thus inducing crevice corrosion initiation [28]. The authors calculated an *IR*-drop of approximately 300 mV using a crevice gap of 0.1 μm, a crevice solution resistivity of 7.5 Ω.cm., a passive current density $i_{pass}=8\times10^{-7}$ A/cm^2, and a crevice depth of 1 cm. It was found that the calculated *IR* drop is larger than the *IR**, thus the *IR* forces some portion of the crevice wall to reside at a potential below E_{crit}, in the active region of the polarization curve, causing active dissolution of the alloy. A more descriptive explanation of the proposed mechanism for crevice corrosion initiation in nickel alloy 625, given by Shaw and Moran [28], is shown in Figure 19.

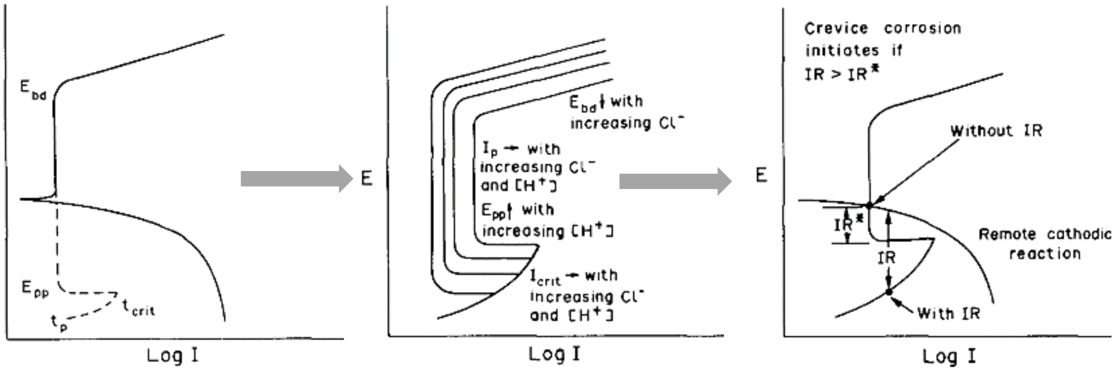

Figure 19. Schematic illustration of IR induced crevice corrosion mechanism for a corrosion resistant metal, such as alloy 625, in an aerated seawater environment. (a) Anodic and cathodic polarization curves for a corrosion resistant metal in seawater. (b) Changes in anodic polarization behavior of alloy 625 resulting from the formation of a CCS. (c) Mixed potential analysis of the crevice coupled formed by the anodic curve in the aggressive crevice solution and the cathodic curve for the metal outside of the crevice. From Shaw et. al. [28].

Initially, when the crevice is exposed to the bulk environment, the anodic polarization curve of the alloy is self-passivating and shows a low passive current value and a relatively high breakdown potential. The cathodic polarization curve shows a limiting current density before experiencing hydrogen evolution reduction, as is shown in Figure 19 (a). As time increases, the solution within the crevice becomes more aggressive, and the anodic polarization response of alloy 625 starts to change, see Figure 19 (b). This figure shows that when the Cl^- concentration increases and the pH of the crevice solution decreases, E_{crit} shifts positively (towards more oxidizing potentials), the breakdown potential (E_{bd}) shifts negatively, and i_{crit} and i_{pass} increase. Figure 19 (c) shows the mixed potential analysis performed between the anodic polarization curve obtained in the CCS and the cathodic polarization curve obtained in the bulk environment. The intersection point lies in the passive region of the anodic curve. In this figure, it can be noticed that the magnitude of IR exceeds the critical IR^* value, i.e. $IR>IR^*$. Thus, the IR drop is responsible for placing the potential of the crevice wall below E_{crit}, in the region of active dissolution, where the passive film is no longer stable and crevice corrosion initiates.

Lillard and Scully [58] developed a mathematical model to describe the crevice corrosion initiation and propagation of alloy 625, which only presents an active to passive transition once a CCS within the crevice has been formed. As such, this mathematical model considers the importance of addressing both mass transport and ohmic resistance within the crevice simultaneously. The systems under study were nickel alloy 625 in chlorinated and non-chlorinated ocean water. Current and potential distribution were calculated as a function of crevice depth. Since both the CCS and the IR*-drop are key parameters for modeling the initiation of crevice corrosion in alloy 625, the following criteria were used in the model: *(i)* $E<E_{flade}$, *(ii)* $i_{diss}=10\ \mu A/cm^2$, *and (iii)* $pH= -0.46$ *at the site where the first two criteria are met* [58]. These criteria are met only if a crevice with a large aspect ratio is considered since this *(i)* restricts transport and promotes the development of a CCS, and *(ii)* provides a sufficient potential drop down the length of the crevice to exceed the IR* voltage required for initiation, i.e. $E<E_{flade}$. Additionally, the model considers that the current density at the initiation site must be high enough to reach significant metal dissolution: as such the Oldfield-Sutton criterion of 10 $\mu A/cm^2$ was incorporated into the model. The current and potential distribution at any position within the crevice predicted by this model, for both chlorinated and non-chlorinated ocean water, are shown in Figures 20 and 21.

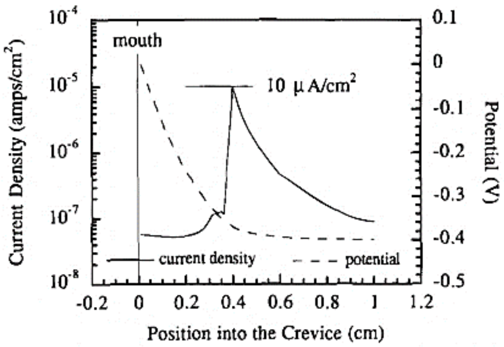

Figure 20. Results from the SCPDM of an alloy 625 crevice (gap=0.1μm) in chlorinated ASTM artificial ocean water, E_{cell}=0.400 V. The current/potential at any one position is that of the crevice wall at that position. Initiation occurs at position 0.40 cm. From Lillard and Scully [58].

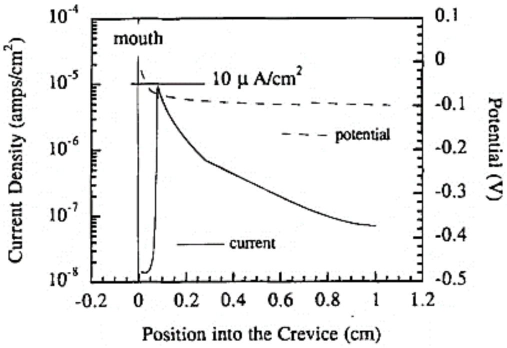

Figure 21. Results from the SCPDM of an alloy 625 crevice (gap=0.1μm) in non-chlorinated ASTM artificial ocean water, E_{cell}=0.100 V. The current/potential at any one position is that of the crevice wall at that position. Initiation occurs at position 0.07 cm. . From Lillard and Scully [58].

From the modeling results, the authors found that the crevice corrosion initiated deeper into the crevice for the chlorinated system than for the non-chlorinated system. Chlorinated systems raise the OCP of the boldly exposed material which in turn increases the driving force for crevice corrosion initiation. In the two cases of study in this model, the chlorinated and non-chlorinated systems had OCP values of 0.4 V and 0.1 V, respectively. A larger driving force requires a larger IR-drop, i.e. $IR^* = E_{app} - E_{crit,}$ as shown in Figure 20, which requires a longer diffusion path within the crevice for the potential to shift into the active corrosion region of the polarization curve (where high anodic dissolution occurs) by means of solution resistance down the length of the crevice. From the mass transport perspective, a long diffusion path between the crevice mouth and the active site is also required for the formation of a CCS. On the other hand, a small driving force, as shown in Figure 21, provides a small diffusion length between the crevice mouth and the active site where the 10 μA/cm^2 criterion is reached. This distance is not long enough to restrict mass transport sufficiently to cause the formation of the CCS. Hence, the driving force provided by the non-chlorinated solutions is not sufficient to initiate crevice corrosion within the mass-transport context.

Other mathematical models combining both the CCS and IR*-model, also including transport processes such as migration and diffusion and calculating concentration profiles of chemical species within the crevice, have been proposed by Watson and Postlethwaite [59] and Kennell, et. al [60].

1.3.2. Crevice Corrosion Initiation and Propagation

Stockert and Böhni [61] determined that for stainless steels, crevice corrosion initiation follows from metastable pitting within the crevice. This research was extended to nickel alloy 22 and nickel alloy 625 by Kehler and Scully [62]–[64], who suggested that metastable pitting contributes to the acidification of the solution inside of the crevice at a critical distance from the crevice mouth x_{crit}. The occluded region and restricted mass transport within the crevice prevent the repassivation of the metastable pits once they have been formed, unlike typical metastable pits on open surfaces which will repassivate due to their inability to maintain the pit cover, which allows the pit anolyte to be diluted rapidly. Within a crevice, as the metastable pits lose their covers as the geometry of the occluded region prevents the metal cations and the hydrolysis products that had formed within the metastable pits from diffusing out of the crevice. Thus the coalescence of metastable pits at a critical distance from the crevice mouth (x_{crit}) contributes to local acidification, causing an increase in the local passive current [64]. A similar phenomenon, referred to as micropitting, was observed in stainless steel by Oldfield and Sutton [45], who documented the formation and coalescence of micropits in the deepest region of the crevice, where mass transport is most restricted. This coalescence of metastable pits was observed on the electrode surfaces prior to crevice corrosion propagation. It must be noted that this mechanism applies only to crevice corrosion in passive metals and in alloys which undergo pitting in chloride solutions [9].

Crevice corrosion initiation, propagation, and damage of nickel alloy 625 under potentiostatic conditions in natural sea water has been evaluated by Martin et al. [65], [66]. The authors found that under potentiostatic tests the current vs time response of nickel alloy 625 exposed to natural sea water shows an initial decay in current, indicating the passivation of the alloy, until it reaches a minimum. Once this minimum point is reached the current starts to increase rapidly as corrosion initiates and begins to propagate. The current eventually reaches a maximum value at which it plateaus, indicating the stabilization of crevice corrosion.

Shan and Payer [67] found a similar current vs time (*I vs t*) response in nickel alloy C-22. The authors studied the crevice corrosion performance of alloy 22 held at -0.150 V vs SCE, a value more positive than the crevice repassivation potential ($E_{rp,crev}$), in 4 M NaCl solution at 100 ºC. Under this aggressive environment, crevice corrosion occurred in four different stages based on the *I vs t* behavior: initiation, propagation, stifling, and repassivation (see Figure 22). At the beginning of the experiment, it was found that the current decreased over time and the specimen remained in the passive state. After a certain time, or incubation period, there was an increase in the current indicating that crevice corrosion has initiated. The current values continued increasing with time due to the propagation of crevice corrosion, until a maximum current value was reached. The current stayed constant at this maximum value for several hours, after which the current started to decrease, indicating entry into the stifling stage. Finally, the current dropped to values even lower than the ones obtained in the incubation period, indicating that the specimen had repassivated.

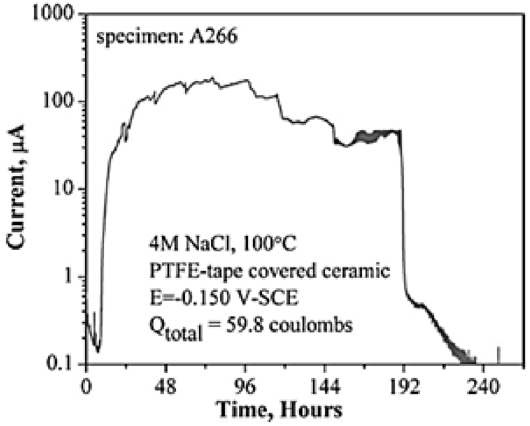

Figure 22. Current-time behavior during constant potential test of alloy 22, E=-0.150 V vs SCE, PTFE-tape-covered ceramic crevice former, and test duration 252 h. From Shan and Payer [67].

While these studies of both nickel alloy 625 and alloy 22 have established this current vs time response, there have not yet been studies proposing the mechanisms causing the appearance of this *I vs t* curve.

Martin et. al. found that crevice corrosion initiation times were dependent on applied potential and temperature. The higher the applied potential, the shorter the initiation times and the deeper the crevice corrosion attack [65], as is shown in Table 2. In addition, higher temperatures required less applied potentials for crevice corrosion initiation to occur. At room temperature it was found that a minimum applied potential of 300 mV vs Ag/AgCl was necessary for crevice corrosion initiation to occur [66].

Table 2. Alloy 625 crevice testing results, from a single series of specimens in natural seawater at 65 ˚C. Taken and modified from Martin et al. [65].

Potential mV vs Ag/AgCl	Initiation time Hours	Crevice Depth Mils
0	N/D	0.2 (etch)
100	9.5	7.8
200	3.5	10
300	1.7	24
400	1.2	49

Martin et al. also found that crevice-free specimens of nickel alloy 625 exposed to natural sea water at ambient temperature would, over time, undergo ennoblement, reaching a potential exceeding 300 mV vs Ag/AgCl after approximately 30 days of exposure, see Figure 23. Similar results were obtained by Shawn et al [28]. The studies conducted by Martin et al. were designed to study the effect of applied potential and temperature on the initiation of crevice corrosion, and did not, due to short observation periods, study the propagation stage of crevice corrosion nor the morphology of crevice corrosion damage.

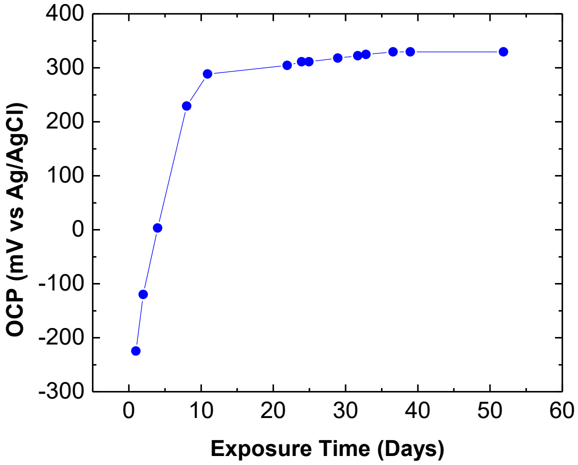

Figure 23. Corrosion potential ennoblement on Alloy 625 during exposure to ambient temperature seawater. Taken from Martin et. al. [65].

The progression of crevice corrosion in nickel alloy 625 was studied by Bocher et al. [68]–[70]. The authors developed a multielectrode array that simulated a flush-mounted planar electrode, with 100 close-packed electrodes, each 250 µm in diameter (see Figure 24). This array was designed to monitor the anodic current evolution as a function of position during the crevice corrosion process. In 0.6 M NaCl at 50˚C, crevice corrosion damage in alloy 625 initiated at 18 hours, appearing first near the tip of the crevice (at a critical distance x_{crit}) and then propagating out towards the mouth.

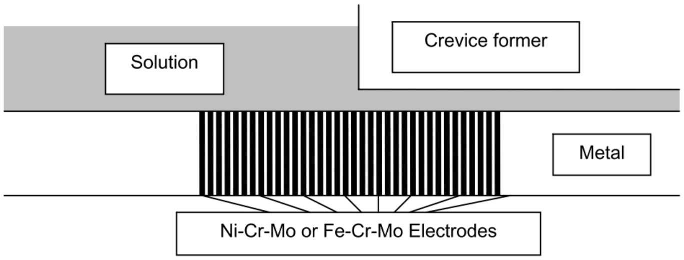

Figure 24. A schematic diagram of the cross section of a multi-electrode array in conjunction with a crevice former. Taken from Ref. [69].

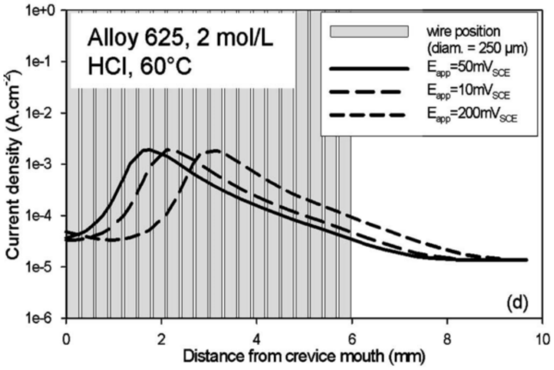

Figure 25. Anodic polarization behavior of alloy 625 in 2 M HCl at 60 °C. The derived evolution of current density with distance from the crevice mouth at various potentials are shown assuming a 3 µm gap. Taken from Ref. [69].

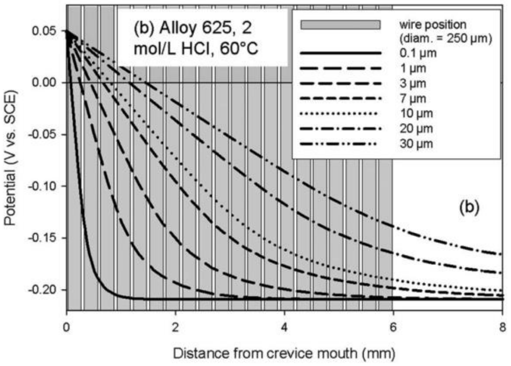

Figure 26. Evolution of potential with distance from the crevice mouth calculated for various crevice gaps for alloy 625 in 2 M HCl at 60 °C at E_{app}=0.05 V vs SCE. Taken from Ref. [69].

The initiation of crevice corrosion was explained by the authors using the mixed *IR-CCS* model [28]. Using a 2 M HCl-based solution at 60 °C as a simulated CCS, Bocher et al. found that nickel alloy 625 had an active to passive transition. Based on this polarization curve, and assuming a 3 µm crevice gap, the evolution of current density and the potential drop along the crevice length were calculated (as shown in Figures 25 and 26). As predicted by the *IR*-model, $E_{crit} \approx -0.13$ V vs SCE was lower than $E_{app} = 0.05$ V vs SCE, and the IR drop within the crevice was significant, causing crevice corrosion to initiate at x_{crit}. The calculated x_{crit} was consistent with the experimental x_{crit}.

Regarding the measured current densities, Bocher et al. found that the closer the electrodes are to the crevice mouth, the higher the current densities. Consequently, a deeper attack was obtained near the crevice mouth. The authors attributed this to the observation that as the propagation of crevice corrosion occurs, the CCS changes to a nearly saturated chemistry, and current density increases. The authors also found that as active crevice corrosion moved, the area left behind immediately repassivated.

1.3.3. *Predicting the pH of CCSs*

Previous researchers have used a variety of empirical and theoretical methods to calculate the pH of simple HCl-based solutions as well concentrated metal salt solutions [14], [22], [45], [71]. Real crevice solutions are characterized by high metal cation and chloride concentrations. As a result, as proposed by Oldfield and Sutton, H^+ ions in the solution may have a much higher activity coefficient than their concentration in the solution would suggest [44]. The higher activity coefficient results in a lower pH value. In order to take this into consideration Oldfield and Sutton proposed and empirical relationship for calculating the pH of solutions containing Ni^{2+}, Cr^{3+}, Fe^{2+}, Mo^{3+}, and Cl^- in solution, based on the work of Mankowski and Szlarka-Smialowska [72]. These empirical relationships are shown in the following equations:

For $[CrCl_3] \leq 2N$ (Cl):

$$pH = pH_{calc} + 0.60(2 - [CrCl_3]) - 0.23([FeCl_2] + [NiCl_2] + [MoCl_3]) \qquad \text{Equation 8}$$

For $[CrCl_3] \geq 2N$ (Cl):

$$pH = pH_{calc} - 0.33([CrCl_3] - 2) - 0.23([FeCl_2] + [NiCl_2] + [MoCl_3]) \qquad \text{Equation 9}$$

where,

$$pH_{calc} = 1.53 - \frac{1}{3} log[CrCl_3] \qquad \text{Equation 10}$$

The concentrations of $CrCl_3$, $NiCl_2$, $FeCl_2$ and $MoCl_3$ are in normality, where normality is the product of molarity and valence. The concentration of $CrCl_3$ in the pH_{calc} equation is in molarity. These calculations were taken into consideration for pH corrections in their mathematical model. Oldfield and Sutton proposed that acidification and Cl^- are the most important values for defining a CCS, and so defined a CCS as a solution of pH and Cl^- concentration sufficient to produce an anodic current of at least 10 $\mu A/cm^2$. For alloy 625, they determined that the CCS required a pH and Cl^- concentration of 0 and 6 M, respectively.

Following these findings, Lillard et al. [22] prepared a variety of simulated crevice solutions using a range of HCl concentrations. For calculating the pH of these solutions, Lillard et al. used the general definition of pH, where the hydronium activity coefficient is a function of the ionic strength of the solution:

$$pH = -\,log(\gamma_{HCl}\, m_{HCl}) = -0.153\, I - log(m_{HCl}) \qquad \text{Equation 11}$$

where $I = 0.5 \sum C_i Z_i^2$ is the ionic strength of the electrolyte solution that is equal to the concentration of HCl for this 1:1 electrolyte. Bocher et al. [71] also simulated crevice solutions using HCl ranging from 0.1 – 10 M. They further refined their simulated crevice solutions based on the below empirically derived equation to calculate the activity coefficient. Based upon their research the activity coefficient was more negative at higher HCl concentrations. Bocher et al. also used the general definition for calculating the pH:

$$pH = -\log\left(\gamma_{H^+}^{m}\, m_{H^+}\right) \qquad \text{Equation 12}$$

where,

$$\gamma_{H^+}^{m} = 0.004[Cl^-]^4 - 0.0426[Cl^-]^3 + 0.2458[Cl^-]^2 - 0.3043[Cl] + 0.8809 \qquad \text{Equation 13}$$

Another methodology for calculating thermodynamic properties, such as pH, of concentrated solutions is by using OLI software. OLI software employs the model for the calculation of thermodynamic properties in mixed-solvent electrolyte (MSE) systems established by Wang et al. [73]–[75]. This model combines the standard properties of all species that are present in the system and the formulation of the excess Gibbs energy which accounts for the solution nonideality. In an MSE system, the partial molal Gibbs energy of species i is given by:

$$\overline{G_i} = \overline{G_i}^0 + \overline{G_i}^{ex} \quad \text{Equation 14}$$

Where, $\overline{G_i}^0$ and $\overline{G_i}^{ex}$ are the standard partial and excess Gibbs energy, respectively. Thus, the computation of $\overline{G_i}^0$ and $\overline{G_i}^{ex}$ become very important to describe the electrolyte thermodynamics.

In the MSE model, the standard partial Gibbs energy is calculated by using the HKF (Hengelson-Kirkham-Flowers) equation of state.

In real solutions, the activity coefficient deviates from ideality due to several ionic interaction phenomena, such as electrostatic interactions, specific ion-ion, ion-molecule, and molecule-molecule interactions, hydration, and solvation phenomena, among others [73], [74], and this non-ideality of a solution is defined by the excess Gibbs energy. The contribution to the total excess Gibbs energy due to the different interactions in the solution are usually separated into long-range ionic interactions and short-range interactions between all species, ions, and molecules. Long and short-range terms are typically sufficient for representing the thermodynamic properties of moderately concentrated solutions, and different models considering only these two interactions have been proposed by different authors [76]–[80]. For systems that may reach very high concentrations, i.e. fused salts or pure acids, a more complex approach for representing the thermodynamic properties is necessary. In these systems, total excess Gibbs energy is modeled using an additional middle range interaction term [73], [81]. In the MSE model, the long-range term, which reflects only electrostatic effects, is calculated by the Pitzer-Debye-Hückel formula. The middle-range interaction term, which incorporates several ion interaction terms, is calculated by using the ionic strength-dependent symmetrical second virial coefficient type. The short-range interactions and structural effects are accounted for using the local composition model defined by UNIQUAC. Considering these forces, the expression of the total excess Gibbs energy for a mixed-solvent electrolyte is constructed as a sum of these three terms:

$$\frac{G^{ex}}{RT} = \frac{G_{LR}^{ex}}{RT} + \frac{G_{MR}^{ex}}{RT} + \frac{G_{SR}^{ex}}{RT} \qquad \text{Equation 15}$$

where G_{LR}^{ex}, G_{MR}^{ex}, and G_{SR}^{ex} represent the long, middle, and short-range contributions, respectively. As an example of the parameters that are used to calculate these energies, consider the long range free energy G_{LR}^{ex}. This contribution considers the sum of the ionic strength of all the species as well as their hard-core collision diameters. Subsequently, the individual activity coefficient for any species i, G^{ex}, is calculated by differentiating with respect to the number of moles at a constant temperature and pressure:

$$\ln(\gamma_i) = \frac{1}{RT}\left(\frac{\partial G^{ex}}{\partial n_i}\right)_{T,P,n_{j\neq i}} \qquad \text{Equation 16}$$

Thus, the activity coefficient of species i is given by:

$$ln\,\gamma_i = ln(\gamma_i^{LR}) + ln(\gamma_i^{MR}) + ln(\gamma_i^{SR}) \qquad \text{Equation 17}$$

For calculating the pH, the general definition of pH is applied, and the pH for different molal concentrations of the mixed solvent electrolyte can be predicted:

$$pH = -\log(m_{H^+}\,\gamma_{H^+}) \qquad \text{Equation 18}$$

1.3.4. Crevice Corrosion Products

The study of the corrosion products is of significant importance because it provides information about the stability of the main metal cations under the crevice conditions and also helps to provide a plausible mechanism for crevice corrosion damage evolution.

Shan and Payer [67] studied the crevice corrosion performance of alloy 22 under anodic potentiostatic conditions in 4 M NaCl solution at 100 ºC. The composition of the corroded metal surfaces and the corrosion products after the potentiostatic experiments were used by Shan and Payer in order to have a better understanding of the localized process and to propose a mechanism of crevice damage evolution. The authors analyzed two different areas were corrosion products precipitated out. The first area was within the crevice, characterized by having lose black corrosion products. It was found that this area was depleted in Ni, Cr, and Fe, enriched in Mo and W, and contained high amounts of oxygen, suggesting that the corrosion products within the crevice were metal oxides/hydroxides. The second area where corrosion products were found was located outside and along the edges of the crevice mouth and were characterized by a dark green color. It was found that the Cr/Ni, Fe/Ni, and Mo/Ni ratios were higher than those in the bulk alloy. This precipitate also contained a high amount of oxygen. Furthermore, the authors also analyzed the corrosion products that precipitated in solution. These were characterized by a light green color, and also contained Cr, Fe, and Ni. The Cr/Ni and Fe/Ni ratios were higher than those in the bulk alloy. Mo content was low, and there was no detection of W or Co. Finally, an analysis of the bulk solution was performed, showing Ni, as Ni^{2+} or Ni chloride complex, as the main soluble species in the test solution. The authors suggested that Alloy 22 followed a congruent dissolution in the active regions within the crevice and not a preferential dissolution. They explained that the different distribution of the elements in the corrosion products was due to precipitation and transport processes. Based on Pourbaix diagrams generated in the same aggressive conditions of the experiment, 4M and 100ºC, the authors provided an explanation of the distribution of the corrosion products in this study. It was found that in the aggressive crevice solution Ni, Cr, Co, and Fe form acid-soluble species, either as soluble ions or metal-chloride complexes, and move out the crevice by migration or diffusion processes. W and Mo remained in the corroded area within the crevice as oxide/hydroxides.

Jakupi et al.[24] studied crevice corrosion products of alloy 22 specimens in 5 M NaCl at 120ºC under galvanic conditions, and also focused on the effect of Mo content on the propagation and repassivation of crevice corrosion. It was observed that the insoluble corrosion products were prone to accumulate within the corrosion-damage region, preferentially within corroded grain boundaries. These corroded regions were enriched in Mo, W, and O and depleted in Ni and Cr relative to the undamaged regions of the crevice specimens. These insoluble corrosion products were analyzed via Raman Spectroscopy and were identified as the oxide MoO_3, and the polymeric species $Mo_7O_{24}^{6-}$ and $Mo_8O_{26}^{4-}$. The formation of the polymeric species was attributed to the thermodynamic instability of MoO_4^{2-} at low pH values. The authors also suggested that polymeric tungstates may have been formed from WO_4^{2-}, though to a lesser extent than molybdates. Based on this study, Jakupi et al. have suggested that alloying Mo and W play an important role in lowering crevice damage propagation rates due to the formation of these insoluble polymeric molybdates and tungstates on the actively corroding surfaces.

Martin et al. [82] have studied the corrosion products of nickel alloy 625 under potentiostatic conditions. Shan et al. [67] and Jakupi et al. [24] have studied the crevice corrosion products of alloy 22 under galvanostatic and potentiostatic conditions, respectively. Despite differences in the alloy and the experimental methodology, insoluble corrosion products rich in Mo and Nb for alloy 625 and Mo and W for alloy 22 were found on the corroded surfaces. These studies evaluated the crevice corrosion products after a predetermined period of time had passed, and did not investigate changes in the corrosion products over time.

1.3.5. Test techniques for evaluating crevice corrosion

Several tests have been developed over the years to determine the crevice corrosion resistance of alloys. The usual reasons for testing a material are to determine whether it will perform satisfactorily in a given environment and to see how it compares with other material in this respect. In some other cases, tests are used for evaluating and understanding the mechanism by which crevice corrosion initiation and propagation occur. When testing for the purpose of predicting performance of an alloy in a given environment it is important that the test, the environment, and the crevice assembly correspond to the practical situation to which it is being related [83]. Crevice corrosion testing types fall into two broad categories: accelerated tests and natural exposure tests. Within the accelerated tests, there are again two types: electrochemical and chemical tests. Both natural exposure and accelerated tests frequently use artificial crevice assemblies so as to control the dimensions and characteristics of the crevice specimens.

There are several types of crevice assembly that have been developed; some of these will be described below.

1.3.5.1. Crevice Former Devices

1.3.5.1.1. Multiple Crevice Assembly (MCA)

A common type of MCA, which is described in the ASTM Standard G-78 [84], consists of two nonmetallic segmented washers, each with an number of grooves and plateaus on their face (see Figure 27). These washers are tightened against a test-panel (made of the alloy under study) using a nut and bolt. A torque wrench is typically used to guarantee a similar tightness across the specimens. Each of the non-metallic washers provides sites for initiation of crevice corrosion were the washers' plateaus touch the surface of the metal. The materials susceptibility to initiation can be determined by the number of the crevice sites that display damage. The crevice propagation can be studied by measuring the crevice corrosion penetration depth.

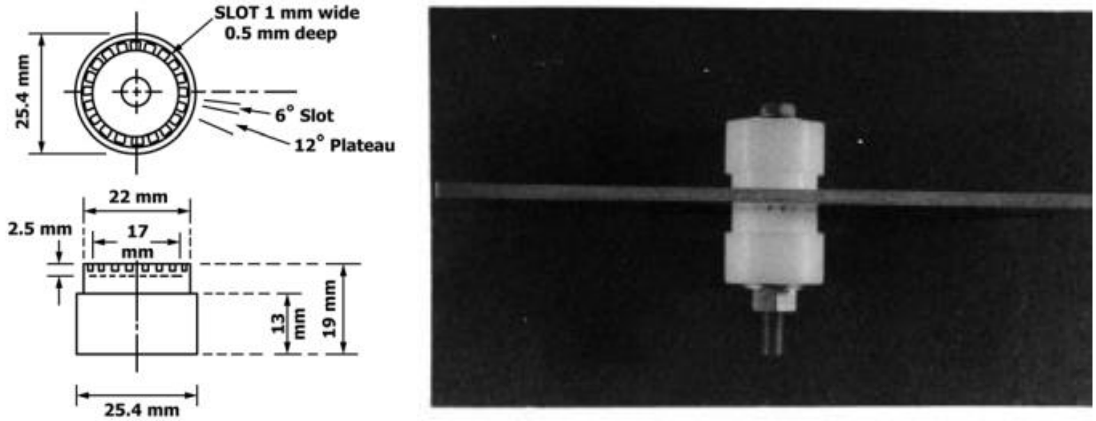

(a) (b)

Figure 27. (a) Details of multiple crevice washer (not to scale) and (b) Multiple crevice assembly with sheet specimen. Taken from ASTM Standard G-78 [84].

1.3.5.1.2. Single Crevice Assembly

Single crevice assemblies have also been developed in attempt to quantify the effect of crevice gap and depth, providing a fixed area of study with one possible crevice site per specimen (see Figure 28). As with the MCA, the SCA is tightened against the test panel with a nut and a bolt at a determined torque (to guarantee a consistent tightness across the specimens). Like the MCA, the SCA provides information about the material’s susceptibility to crevice corrosion initiation and propagation [65]. Modifications of these assemblies have been constructed using a transparent material such as Perspex, allowing the initiation site to be observed and identified during the test [85].

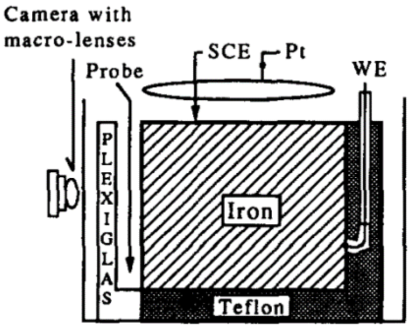

Figure 28. Single crevice design from Pickering et. al. experiment [55].

1.3.5.1.3. Remote Crevice Assembly (RCA)

This tests was developed so that the anode and the cathode could be studied individually during an exposure test [86], [87]. The anode and the cathode are physically separated but electrically connected. The anode (crevice) is formed by sandwiching the specimen between two acrylic plates. Both the creviced anode and the uncreviced cathode are exposed in the environment of interest, see Figure 29. This electrochemical tests can be conducted at open-circuit potential conditions by galvanically coupling the creviced specimen to the uncreviced specimen and measuring the current flow using a zero-resistance ammeter [22], [87]. Initiation of crevice corrosion can be detected when a rapid increase in current occurs. The rate of crevice corrosion propagation is indicated by the magnitude of the current.

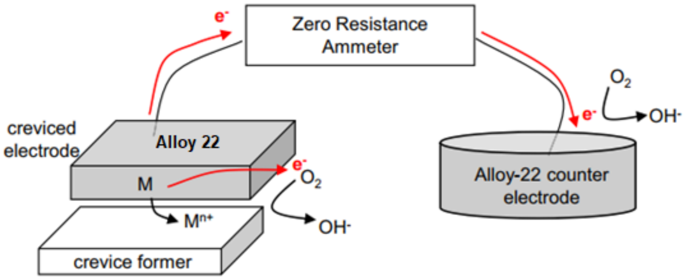

Figure 29. Schematic illustration (not to scale) of the galvanic coupling of a creviced Alloy-22 electrode and a large counter electrode of the same material. Taken from Jakupi et. al. [88].

1.3.5.2. Accelerated tests

1.3.5.2.1. Electrochemical tests

When studying crevice corrosion through electrochemical testing, two different potentials have been established as a measure of crevice corrosion resistance: Crevice initiation potential (E_{crev}) and crevice repassivation potential ($E_{rp,crev}$). It has been suggested by several authors [6], [89]–[91] that at a potential below $E_{rp,crev}$, the alloy will not develop crevice corrosion under the tested conditions, and that if a potential above $E_{rp,crev}$ is applied, crevice corrosion may initiate. E_{crev} and $E_{rp,crev}$ are dependent on the electrochemical technique used, so it is difficult to use this parameter to predict long term performance of a given alloy in a natural environment [92], [93]; however these parameters are useful for purposes of comparison. Descriptions of some of the most used electrochemical techniques for studying crevice corrosion are given below.

1.3.5.2.1.1. Cyclic Potentiodynamic Polarization (CPP) Method

The CCP technique uses a continuous change of potential at a fixed scan rate, and measures the current response as a function of potential ($I=f(E)$). Both forward (increasing potential) and reverse (decreasing potential) scans are performed to obtain the CPP curve. A detailed standard procedure for carrying out this method can be found in the ASTM standard G-61[94], which recommends a scan rate of 0.6 V/h. From a CPP curve, the crevice repassivation potential $E_{rp,crev}$ will be determined as the potential at which the crossover of the reverse and forward scans occurs. A main difficulty of using this technique is that it is strongly dependent on the potential scan rate [92], [93].

1.3.5.2.1.2. Potentiostatic Method

A more conservative estimate of crevice initiation potentials (E_{crev}) can be obtained by using a potentiostatic technique in which a constant potential is applied, and the current is recorded as a function of time. At electrode potentials below E_{crev}, the current decays to a constant value over time. At E_{crev}

and above, the current increases with time as crevice corrosion initiates and propagates [95]. A new specimen is used with each current vs time response. Potentiostatic techniques are preferable over potentiodynamic techniques, but they require more specimens and longer experiments.

1.3.5.2.1.3. Tsujikawa-Hisamatsu Electrochemical (T.H.E) Method

The Tsujikawa-Hisamatsu Electrochemical (T.H.E) test method is an anodic polarization method that combines potentiodynamic, galvanostatic, and potentiostatic electrochemical test techniques [96]. This method was developed for studying alloy 22, but recently has been used for studying other corrosion resistant alloys as well [97]. A brief summary of this technique is given below; a more detailed description of this method is presented in ASTM standard G-192 [98].

The T.H.E method consists of anodically polarizing an artificially creviced specimen in three steps:

- <u>Step 1 (Potentiodynamic Mode):</u> The artificially creviced specimen is polarized potentiodynamically at a rate of 0.6 V/h starting a few millivolts below E_{corr} until reaching a predetermined current density, e.g. 2μA⁄cm^2. After this initial anodic potentiodynamic polarization, the polarization control is changed to galvanostatic mode (Step 2).
- <u>Step 2 (Galvanostatic Mode):</u> The predetermined current density is kept constant for a 2 h period in order to initiate and propagate crevice corrosion. During this galvanostatic mode, the potential is monitored over time. Once the galvanostatic hold is finished, the polarization control is shifted to the potentiostatic mode.
- <u>Step 3 (Potentiostatic Mode):</u> A potentiostatic hold immediately follows the galvanostatic hold, at a potential 10 mV lower than the last read at the end of the galvanostatic hold. The initial potentiostatic hold is carried out during a 2 h period, and the current vs time output is monitored during this time. Successive 2 h potentiostatic holds follow, each at 10 mV lower than the previous one, until reaching the crevice repassivation potential ($E_{rp,crev}$). $E_{rp,crev}$ is reached at the potential at which the current density ceases to increase as a function of time.

1.3.5.2.2. Chemical tests

Chemical tests, using an activator such as Cl^- and an oxidizing agent at a known concentration [83], can be used for ranking alloys according to their resistance to crevice initiation. The most commonly used chemical test uses ferric chloride solution (6 wt% $FeCl_3 \cdot 6\ H_2O$) as an oxidizing chloride environment (ASTM Standard G-48 [99]). This test involves immersing a standard creviced specimen for a predetermined time period to initiate crevice corrosion; a reasonable time suggested by the standard is around 72 h. Information such as weight loss and crevice damage penetration depth are reported as indicators of susceptibility to crevice corrosion. Ferric chloride solution used in this test is similar to, but not the same as, the crevice solution that would form inside crevices of ferrous alloys in chloride environments. This test cannot be used to predict crevice corrosion resistance in natural environments.

1.3.5.3. Exposure tests

Exposure tests were developed to simulate the conditions found in natural environments. These tests were designed to rank the behavior of different alloys exposed under the same conditions. Creviced specimens are immersed for long periods of time, in the order of months or years, and the ranking of the alloys is based on the time required for crevice corrosion to initiate. Periodic monitoring of the corrosion potential allows the detection of any increase in the corrosion rate, signaling that the initiation of active corrosion in the crevice has commenced [30], [83].

II. EXPERIMENTAL METHODS

Crevice corrosion damage in RCAs was studied using potentiostatic tests at various immersion times and potentials. The polarization response of nickel alloy 625 in ASTM artificial ocean water was evaluated by means of cyclic potentiodynamic polarization (CPP) tests. The polarization response of nickel alloy 625 in simulated CCSs, solutions simulating the chemistry found within occluded regions, was also evaluated by means of CPP technique. A detailed description of the specimen preparation, solutions, and electrochemical techniques will be provided in this section.

OLI simulation software was used in this research for studying the thermodynamic properties of the artificial simulated metal salt solutions. A detailed description of the main assumptions and the parameters used for performing these simulations will also be presented in more detail in this section.

2.1. Cyclic Potentiodynamic Polarization Response of Nickel Alloy 625

2.1.1. Specimen Preparation

Two different specimens were used for obtaining the electrochemical response in the simulated bulk solutions (ASTM artificial ocean water) and the critical crevice solutions (metal salt or HCl-based solutions).

Alloy 625 discs supplied by Rolled Alloys Inc., with the dimensions shown in Figure 30, were mounted in epoxy and submerged in the simulated bulk solution (ASTM ocean water). Specimens for polarization tests in artificial crevice solutions were prepared from a 0.3 cm thick plate of alloy 625 (Metalmen, New York). The chemical analysis of the discs and the plate as supplied by the manufacturer are listed in Table 3. For the polarization tests in artificial crevice solutions, the plate was machined into a “lollipop” shaped specimen with the geometry and dimensions shown in Figure 31. This geometry was chosen to eliminate the possibility of crevices potentially formed by interfaces with epoxy mounts. Additionally, the specimen's long stem allowed the potentiostat to be connected directly to the specimen above the liquid/air interface. After cutting, the specimens were degreased with acetone and ethanol and rinsed in DI water. Each specimen was then abraded by successive use of 400, 600, 800, and 1200 grit silicon carbide paper on the two faces and the sides of the specimens. As a final cleaning step, the abraded surfaces were again degreased and rinsed in DI water. The time elapsed between the preparation of the specimen and the beginning of the experiment was usually between 10-15 min. A similar polishing and cleaning procedure was used for the mounted (discs) specimens.

Table 3. Chemical Analysis of Nickel Alloy 625 in wt%.

	Ni	**Cr**	**Fe**	**Mo**	**Nb**	**Ta**	**Ti**	**Al**	**S**	**P**	**Si**	**C**	**Co**	**Mn**
Plate	60.10	21.71	4.73	9.01	3.54	<0.01	0.28	0.19	<0.001	0.007	0.12	0.02	0.18	0.11
Disc	61.54	21.63	3.49	8.56	3.82	<0.05	0.24	0.22	<0.002	0.006	0.16	0.023	0.25	0.27

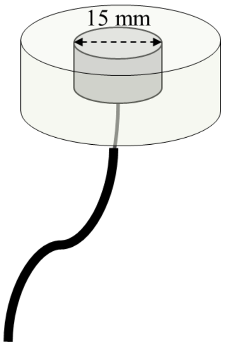

Figure 30. Discs specimens of Nickel alloy 625 mounted in epoxy.

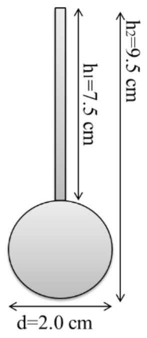

Figure 31. Lollipop shaped specimen of Nickel alloy 625 and its dimensions.

2.1.2. Solutions

ASTM D1148-981 artificial ocean water was prepared from a commercially available sea salt, containing elements found in natural seawater in quantities greater that 0.0004% (Lake Products) [13]. After mixing the salt in deionized water (18.2 MΩ·cm at 25ºC) the pH was adjusted to 8.2 using 0.1 M solution of NaOH or HCl. The density of artificial ocean water is 1.025 g/cm3 at 15 °C.

Simulated crevice solutions were prepared from metal chloride salts or HCl-based solutions. For the metal salt solutions, five alloying elements from nickel alloy 625 were considered: Ni, Cr, Fe, Mo, and Nb. The solutions were prepared by dissolving $NiCl_2 \cdot 6H_2O$, $CrCl_3 \cdot 6H_2O$, $FeCl_2 \cdot 4H_2O$, $MoCl_3$, and $NbCl_5$ salts in deionized water (18.2 MΩ·cm at 25°C) based on the alloy stoichiometry in Table 4. The underlying assumption for using these soluble metal chlorides, is that the hydrolysis reactions and any precipitation that occur in these solutions would also occur inside the crevice. Table 5 lists the composition of the different solutions investigated. The first solution represents a full simulant and is referred to as NiCrFeMoNb. To study the effect of cations on the polarization response, this solution was modified by removing the $NbCl_5$ – this modified solution is referred to as NiCrFeMo in the text. A third solution that removed both $NbCl_5$ and $MoCl_3$ (NiCrFe, or " equivalent chloride solution ") was also prepared. In this solution, sufficient $NiCl_2$ was added such that the Cl^- concentration was equivalent to that of NiCrFeMoNb. The concentration of these metal chloride solutions was also varied (stoichiometrically) between 3.0 molal and 5.0 molal, as summarized in Table 5.

Table 4. Alloy 625 nominal compositions in wt% and mol fraction.

Element	**Ni**	**Cr**	**Fe**	**Mo**	**Nb**	**Total**
wt %	61.01	21.71	4.73	9.01	3.54	100.0
mol fraction	0.6210	0.2495	0.0506	0.0561	0.0228	1.0

Table 5. Concentration in molality of artificial crevice solutions.

	Stoichiometric Solutions					**Equivalent Chloride Solutions**	
Total molality (m)	**3.0**	**3.5**	**4.0**	**4.5**	**5.0**	**3.0**	**5.0**
Ni^{2+}	1.863	2.174	2.484	2.795	3.105	2.286	3.811
Cr^{3+}	0.748	0.873	0.998	1.123	1.247	0.748	1.247
Fe^{2+}	0.152	0.177	0.202	0.228	0.253	0.152	0.253
Mo^{3+}	0.168	0.196	0.224	0.253	0.281	-	-
Nb^{5+}	0.068	0.080	0.091	0.103	0.114	-	-
Cl^- *(NiCrFeMoNb)*	7.122	8.309	9.496	10.683	11.869	7.122	11.869

From a practical standpoint, mixing these metal salt solutions was very difficult and a copious amount of precipitate remained in the bottom of the flask of these solutions. Prior to use, concentrated solutions were stirred for as long as one week. Although this did not appear to have an effect on the amount of precipitate, it did have an effect on the polarization response of the specimen, with solutions that were unstirred being less aggressive. To avoid absorption of CO_2 from the environment all solutions were stirred in a seal volumetric flask.

2.1.3. Electrochemical Techniques

The experimental set-up for evaluating the cyclic potentiodynamic polarization (CPP) electrochemical response of nickel alloy 625 in simulated CCSs and HCl-based solutions was a standard three-electrode system consisting of a working electrode, a saturated calomel reference electrode, and a niobium mesh counter electrode. A diagram of this set up is shown in Figure 29.

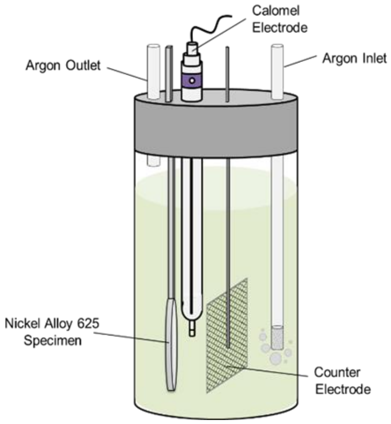

Figure 32. Electrochemical Cell Set Up for evaluating the polarization response of alloy 625 in simulated CCSs.

All the experiments were carried out at room temperature. Solutions were deareated with argon for 12 hours prior to the experiment to ensure depletion of oxygen. The open circuit potential (OCP) was measured for at least 6 hours for each experiment or until steady state was reached, i.e. a change of less than 5 mV/h. The parameters used for CPP tests were: Initial potential E_i = -0.02 V vs OCP, maximum potential E_{Apex}= 1V vs Ref, final potential E_f = 0 V vs OCP, and maximum current density I_{Apex} = 100 mA/cm^2. The scan rate used was 0.6 V/h for both forward and reverse scan, following the ASTM G61standard [94]. No noise in the current due to condensation in the non-immersed part of the specimen were observed.

A standard three-electrode system was also used to study the polarization response of the disc specimens in ASTM ocean water under aerated conditions at room temperature. The parameters used for the CPP were similar to the parameters used on the simulated CCSs, except I_{Apex} = 1mA/cm^2.

2.1.4. ICP Analysis of Critical Crevice Solutions

During the preparation of metal salt artificial crevice solutions, adding Mo and Nb into solution caused some solids to precipitate out to the bottom of the electrochemical cell. Even after mixing these solutions up to 1 week, the separation of two phases was found: a dark red precipitate at the bottom of the electrochemical cell, and a dark green solution at the top. ICP analysis of the precipitates (bottom) and solution (top) was performed. The results obtained from these analyses were compared to the concentration of crevice corrosion products from RCA experiments.

2.2. Potentiostatic tests in RCAs

2.2.1. Specimen preparation

The artificial remote crevice assembly (RCA) consisted of a bolt, a nut, and two washers, all made of nickel alloy 625. In this assembly, the crevice of interest is the metal-metal crevice formed by the two adjoining washers, positioned such that the opposing faces were parallel to one another. These washers were prepared from a 1.5” rod of alloy 625. The original rod was machined into washer-shaped specimens with the geometry and dimensions shown in Figure 33. The nominal composition for the alloy 625 washers is given in Table 6 (Metalmen, NY). The dimensions of the nut and bolt are shown in Figure 34 and 35. Specimens were polished by successive grits of SiC paper 320, 400, 600, 800, and 1200 on the two faces and the outside edge of the washer. As a final cleaning step, the polished surfaces were again degreased.

Table 6. Nominal composition of 1 ½” 625 Rod

Ni	**Cr**	**Fe**	**Mo**	**Nb**	**Ti**	**Al**	**Si**	**Mn**	**C**	**Co**	**P**	**Ta**	**S**
60.56	22.36	3.74	8.76	3.56	0.03	0.18	0.06	0.05	0.05	0.03	0.02	0.01	0.01

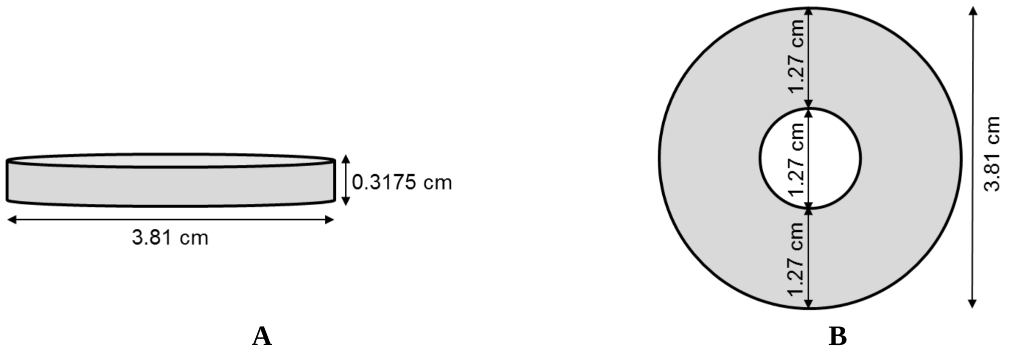

Figure 33. Nickel alloy 625 washer dimensions

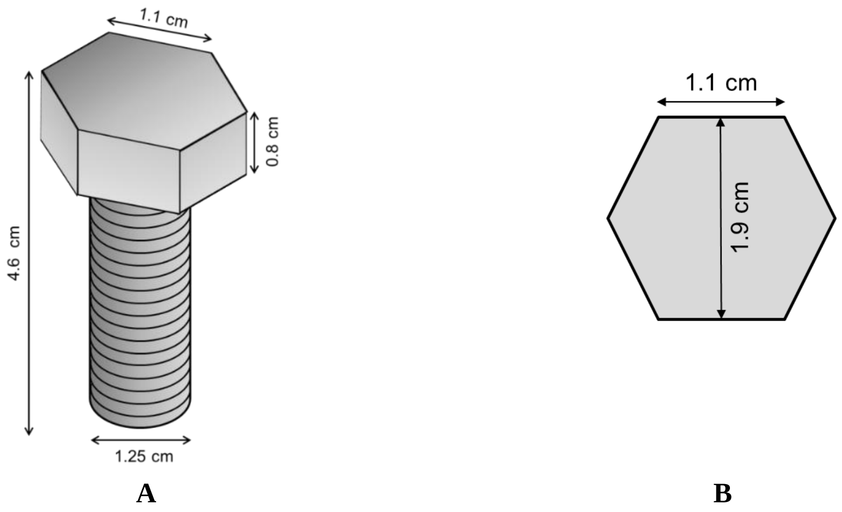

Figure 34. Nickel alloy 625 bolt dimensions

Figure 35. Nickel alloy 625 nut dimensions

The arrangement of the RCA is shown in Figures 36 and 37. The bolt provided electrical contact to the specimen while the nut was separated from the washer by an acetal washer that was used to apply uniform pressure to the washer. A PTFE sheet served to eliminate crevice corrosion between the acetal and 625 washers. Before the assembly was tightened, the nickel alloy washers were wetted with the ASTM ocean water electrolyte. Fixed applied torques were applied to the RCAs in attempt to recreate the same crevice gap in each experiment. Two applied torques were studied: 5 and 10 ft-lb. ASTM artificial ocean water [100] previously described in section 2.1.2 was used for all RCA potentiostatic tests. All experiments were carried out at room temperature.

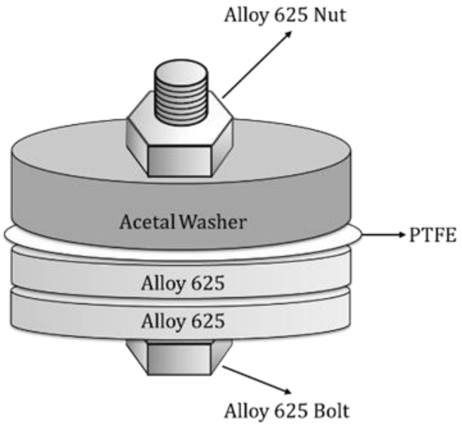

Figure 36. RCA configuration

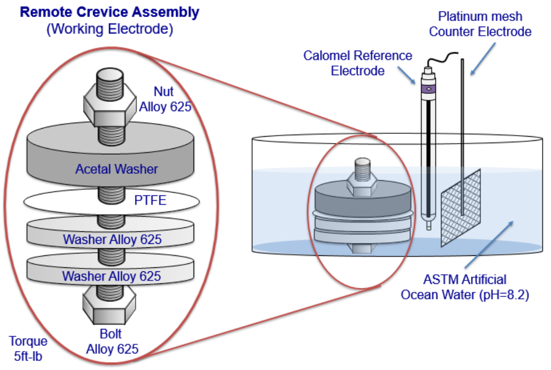

Figure 37. Experimental set-up for anodic potentiostatic experiments.

2.2.2. Electrochemical techniques

Once assembled, the RCA was used to study crevice corrosion damage during potentiostatic holds. In these tests, the RCA was held at OCP for 1 hour, followed by an anodic potentiostatic hold for a predetermined period of time. To study the effect of applied potential on crevice corrosion phenomena, three different anodic potentials were used: 100, 200, and 300 mV vs. SCE. These potential values were chosen because they are in the passive region of the alloy 625 polarization curve in ASTM ocean water at room temperature. At each potential, the RCA was exposed for times of: 12, 24, 36, 48, 60, 72, 168, and 336 hours. Corresponding current vs. time data were collected at a rate of 0.1 points/s (360 points/h).

A summary of the experimental matrix of the experiments performed at different applied potentials and applied torque is presented in Table 7. It is important to mention that for each immersion a new set of washers were polished and assembled for the test.

Table 7. Experimental Matrix for RCA-experiments.
Applied torques: 10ft-lb (~13.56 N.m) and 5ft-lb (~6.78 N.m)

Potential (V_{SCE})	**Time Period (h)**									**Torque (ft-lb)**
100	6	12	24	36	48	60	72	168	336	10
200	-	10	24	36	48	60	-	-	-	5
200	-	12	24	36	48	60	72	168	336	10
300	-	12	24	36	-	-	72	-	-	10

2.2.3. Surface Analysis Techniques

At the conclusion of the test period, the surface morphology of the specimens was examined using a 3D-microscope, a stereomicroscope, and Scanning Electron Microscopy (SEM).

2.2.4. ICP and EDS Analysis of Crevice Corrosion Products

In this study, crevice corrosion products for different immersion times of RCAs during the crevice corrosion process were examined using Inductively Coupled Plasma (ICP) and Energy Dispersive Spectroscopy (EDS) analysis techniques. The evolution of the composition of these crevice corrosion products were studied over time.

2.3. Modified T.H.E Method in RCAs

The repassivation potential of crevice corrosion ($E_{rp,crev}$) in RCAs was evaluated using a modified T.H.E method. The modified T.H.E method uses the same RCA configuration presented in section 2.2.1. All RCAs used for modified T.H.E were tightened to a torque of 10 ft-lb.

2.3.1. Electrochemical Techniques

The solution used for the modified T.H.E method was ASTM artificial ocean water, described in section 2.1.2. All experiments were carried out at room temperature. The modified T.H.E method is a variation of the traditional T.H.E method presented in the ASTM Standard G192 [98]. In the modified T.H.E method, the initiation and propagation of crevice corrosion is induced potentiostatically rather than galvanostatically, and the RCA assembly is anodically polarized in 2 steps:

- Step 1: Crevice corrosion is initiated and propagated in an RCA at 200 mV vs SCE for a predetermined period of time. Five different immersion periods were studied: 12, 24, 30, 36, and 72 hours. During the initiation and propagation period, the current vs time response is monitored. Once the predetermined immersion time is reached, Step 2 follows.

- Step 2: In this step, the potential is stepped down by 10 mV every two hours, and the current response is monitored for the two hours following each step down. This pattern (step down followed by a 2 hour potential hold) is continued until the crevice repassivation potential ($E_{rp,crev}$) is reached.

Before performing the modified T.H.E technique on the RCA, the open circuit potential was measured for 1 hour. A summary of all modified T.H.E experiments, with different Step 1 exposure times, is presented in Table 8. Crevice corrosion repassivation potential ($E_{rp,crev}$) from the T.H.E. data can be obtained for each immersion time. These results show whether or not the repassivation potential depends on the extent of crevice corrosion damage.

After each test period, the surface morphology of the specimens was examined using a 3D-microscope, a stereomicroscope, and Scanning Electron Microscopy (SEM).

2.4. Real Time Video Imaging of Damage in RCAs

This new RCA consisted of a washer made of alloy 625 and a clear acrylic washer as the crevice former. In this assembly, the crevice of interest is the metal-acrylic crevice formed by the two adjoining washers. The RCA was tightened with a bolt and a nut made of nickel alloy 625. The nickel alloy washer was polished by successive use of 320, 400, 600, 800, and 1200 grit silicon carbide paper on the two faces and the outside edge of the washer. As a final cleaning step, the polished surfaces were again degreased.

The arrangement of the parts in the assembly is shown in Figure 38. The bolt provided electrical contact to the specimen. Before the assembly was tightened, the nickel alloy washer was wetted with the ASTM ocean water electrolyte. A fixed applied torque of 10 ft-lb was applied to the RCAs in attempt to recreate the same crevice gap in each experiment.

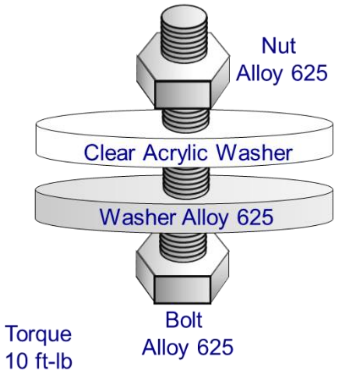

Figure 38. RCA configuration for video recording

The solution used for the modified T.H.E. method was same ASTM artificial ocean water described in section 2.1.2. All experiments were carried out at room temperature. This modified RCA was used to study crevice corrosion damage during potentiostatic holds. In these tests, the RCA was held at OCP for 10 min, followed by an anodic potentiostatic hold of 300 mV vs SCE for 48-60 hours at a data collection rate of 0.1 points/s. At the conclusion of the test period, the surface morphology of the specimens were examined using a 3D-microscope for obtaining crevice corrosion damage profiles.

Crevice corrosion damage evolution was recorded in a time lapse video, collecting 1 image/5 min, with the aid of an Olympus SZX16 Stereoscope at 0.7 X. The experimental set up is shown in Figure 39.

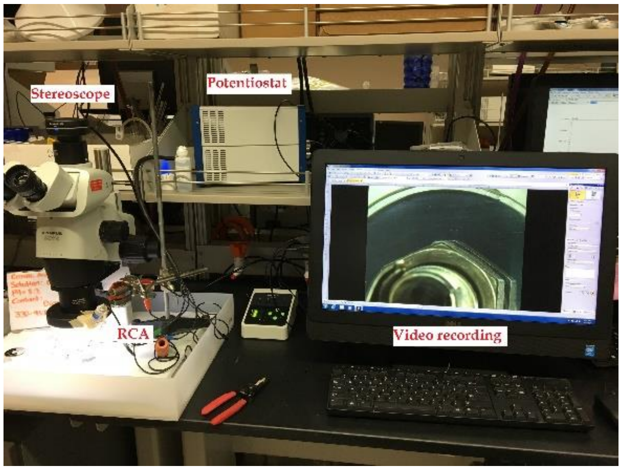

Figure 39. Experimental set-up for video recording.

2.5. X-ray Computed Tomography Inspection of RCAs

X-ray computed tomography (X-CT) machines consist of an X-ray source tube, a detector, and a rotatory table. The rotatory table, which sits between the X-ray source and the detector, rotates 360 degrees while the detector takes radiographic images of the object under different angular positions [101]. With the help of a reconstruction software, the CT system is able to generate a 3D model form the two-dimensional X-ray images for both the interior and the exterior of the part [101], [102].

X-ray Computed Tomography Inspection (X-CT) was used to scan pre-corroded specimens in order to measure the crevice gap of the specimen.

2.5.1. Specimen Preparation and Experimental Set-up

The RCA used for X-CT analysis differs from the RCAs described above in that the traditional circular washer was modified into the shape shown in Figure 40 (a), and only the area delimited by the red square was scanned. The reason that only this portion of the specimen was scanned is that a shorter path length allows more X-rays to penetrate the specimen, and a sharper image can be obtained [102]. The specimen preparation was performed in the same manner as described in section 2.2.1. This modified RCA was studied using metal-metal and metal-acrylic crevices. To tighten the specimens together a bolt and a nut made of Teflon were used, as this allowed for more X-ray passage, and therefore higher resolution images, than could be obtained if an alloy 625 bolt were used as in the other RCAs. The electrical connection for the experimental set up was given by a wire of nickel alloy 625.

(a) (b)

Figure 40. (a) Modified RCA for X-ray Computed Tomography Scanning, and (b) CT image of modified RCA

The modified RCAs were anodically polarized to induce crevice corrosion, then taken out of the solution and prepared for the subsequent X- ray and CT inspection without opening the RCAs. The X-CT machine used was a Nikon XTH 320 CT, see Figure 41. XTH 320 features a multi-voltage X-ray source that is able to run highly accurate inspection on dense materials such as metals. The specimen was placed into the large cabinet, and scanned using a 225-kV reflection target with the aid of Inspect X software, Figure 42. The total scanning time lasted approximately 8 hours. After the scanning of the specimen, the CT datasets were constructed into a 3D CT volume file with the aid of CT-Agent reconstruction software. The reconstructed volume then is visualized and analyzed in a VGStudio 3.0 volume graphics software (see Figure 40 (b)).

The solution used for pre-corroding the specimens was ASTM artificial ocean water, described in section 2.1.2. All experiments were carried out at room temperature. All the modified RCAs were initially held at OCP for 1 hour, followed by an anodic potentiostatic hold for a predetermined period of time. The exposure times range between 1 week up to 2 weeks of exposure. At the conclusion of the test period, the surface morphology of the specimens was examined using a 3D-microscope for obtaining crevice corrosion damage profiles.

Figure 41. X-CT machine

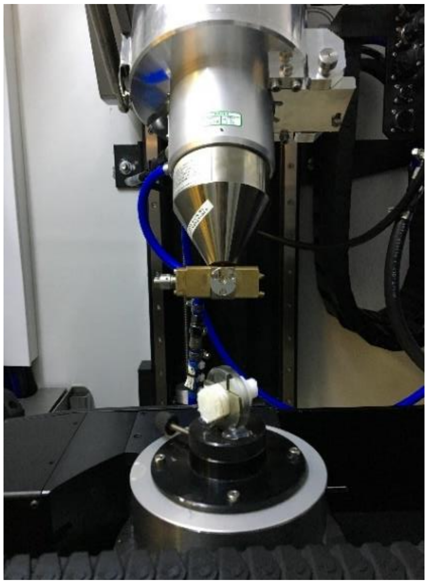

Figure 42. X-CT specimen set up

2.6. Simulation in OLI Software – Stream Analyzer

A commercially available software package (OLI Studio 9.2) was used to calculate the thermodynamic properties of the stoichiometric and HCl-based solutions studied in this investigation [73].

The Mixed Solvent Electrolyte (MSE) model [73], [75] in OLI software was used to simulate the behavior of stoichiometric crevice solutions. A crevice solution is a very reducing environment that promotes the oxidation of metals to the lowest oxidation state. These stable oxidation states under reducing conditions can be easily identified by the aid of Pourbaix diagrams (Figure 1). For the main components of alloy 625, which are Ni(II), Cr(III), Fe(II), Mo(III), and Nb(IV), and the lowest stable oxidation states are: +2, +3, +2, +3, and +5, respectively. Once the stable oxidation states have been identified, it is important to relate them to chemical reagents that can be used as inputs (inflows) for the OLI-simulation. For the case of Ni, Cr, Fe, and Mo metals, their anodic dissolution can be written as:

$$Me \rightarrow Me^{n+} + n\bar{e} \qquad \text{Equation 19}$$

where the electrons n, are consumed by the cathodic process.

This anodic dissolution creates an accumulation of positive charges within the crevice, causing the migration of chlorides into the crevice in order to reach electroneutrality, after which metallic chlorides are formed:

$$Me^{n+} + nCl^{-} \rightarrow MeCl_n \qquad \text{Equation 20}$$

Thus, metal chlorides such as $NiCl_2$, $CrCl_3$, $FeCl_2$, and $MoCl_3$ are chemical reagents that can be used as inflows for the simulation of crevice solutions.

For the metal salt solutions, the chemical reagents considered were: $NiCl_2$, $CrCl_3$, $FeCl_2$, and $MoCl_3$. Nb_2O_5 was used as the reagent for Niobium as the OLI software does not have Nb_2Cl_5 in its database. The most probable stable oxidation state of Nb in acidic reducing conditions is Nb(V), and the only stable form of Nb(V) is Nb_2O_5. Thus, the oxidation reaction for Nb can be written as:

$$NbCl_5 + \frac{5}{2}\,H_2O \rightarrow \frac{1}{2}Nb_2O_5 + 5\,HCl \qquad \text{Equation 21}$$

This indicates that the dissolution of Niobium can be treated as the combination of [0.5 Nb_2O_5 + 5 HCl] for the simulation in OLI software. Thus, the anodic dissolution products of the individual alloy components for this study have been assumed to be $CrCl_3$, $NiCl_2$, $FeCl_2$, $MoCl_3$, and [Nb_2O_5+5HCl], which were used to simulate the anodic dissolution of Ni, Cr, Fe, Mo, and Nb as individual components.

The simulations were performed by varying the number of moles of dissolution products, in steps of 0.5 moles of the alloy per 1 kg of water, in proportion to the mole fractions given in Table 5, and ranging from 0.5 to 9.0. The inputs to the simulation software were: Temperature at 25 °C, pressure of 1 atm, moles of solvent: 1 kg of water equal to 55.5082 moles. All calculations were carried out under the '*single point calculation*' in the software.

III. RESULTS

3.1. Cyclic Potentiodynamic Polarization Response of Nickel Alloy 625

3.1.1. ASTM Artificial Ocean Water

The polarization response of a crevice-free specimen of nickel alloy 625 when immersed in ASTM ocean water is shown in Figure 43. The average OCP = -0.214 V vs SCE This polarization response shows that alloy 625 has a wide passive region, ranging from ~ 0 to ~ 0.3 V vs SCE, and a passive current density $i_{pass} \approx 6.8\times10^{-7}$ A/cm^2. The passivity region was followed by a transpassivity region up to 0.8 V vs SCE. Above the transpassive potential (E_T), the current increased due to (*i*) dissolution of the passive film and (*ii*) oxygen evolution without pitting corrosion. E_T was determined at the inflection point between the passive region and the transpassive region, with a value of 0.32 V vs SCE. When the scan direction was reversed, the specimen showed a negative hysteresis (not shown), indicating that no pitting has occurred on the specimen.

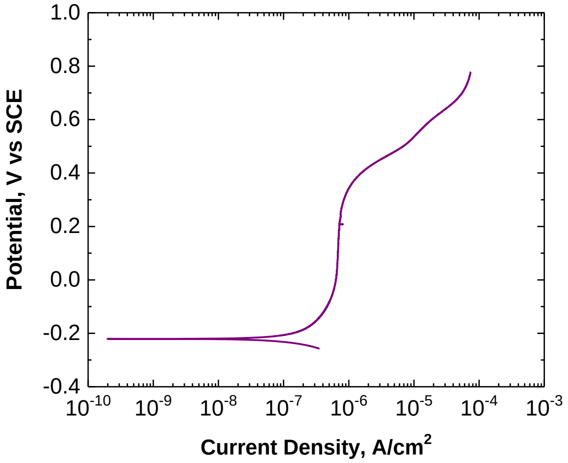

Figure 43. Polarization response of nickel alloy 625 in ASTM artificial ocean water.

3.1.2. Metal Salts Artificial Crevice Solutions

Figure 44 shows the characteristic polarization responses of nickel alloy 625 at different concentrations of NiCrFeMo solutions ranging from 3.0 to 5.0 molal. The polarization response of the 3.0 m solution has an OCP value of 0.12 V vs SCE. Increasing the concentration of the solutions from 3.0 m to 3.5 m resulted in a significant decrease in the value of the OCP. In addition, at concentrations of 3.5 m and greater an active to passive transition was observed. For the 3.5 m solution, i_{crit}=(1.55±0.35)×10^{-5} A/cm^{2} , and at 4.5 m i_{crit} increased to (9.37±0.02)×10^{-5} A/cm^{2}. The average values of peak current densities (of three different measurements) and pH for the concentration of 3.0 m to 5.0 m are summarized in Table 8. Two different pH values are reported: the measured pH or pH$_{meas}$, which is obtained experimentally, and the pH$_{OLI}$, which is calculated using OLI software.

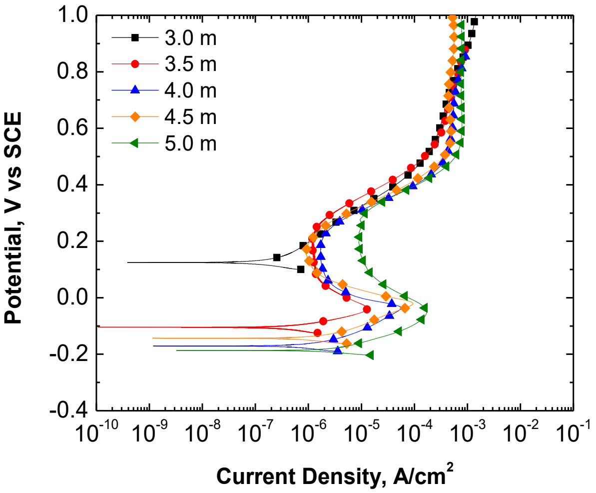

Figure 44. Polarization response of nickel alloy 625 at different concentrations of NiCrFeMo solutions.

Table 8. Average electrochemical parameters of polarization responses at different concentrations in molality of NiCrFeMo solutions.

m	i_{crit} **A/cm^{2}**	E_{crit} **V vs SCE**	**OCP V vs SCE**	**pH$_{meas}$**	**pH$_{OLI}$**
3.0	NA	NA	0.133 ± 0.018	0.25	-0.18
3.5	(1.55 ± 0.35)×10^{-5}	-0.035 ± 0.004	-0.110 ± 0.007	-0.08	-0.28
4.0	(5.22 ± 0.53)×10^{-5}	-0.034 ± 0.001	-0.167 ± 0.001	-0.69	-0.34
4.5	(9.37 ± 0.02)×10^{-5}	-0.012 ± 0.001	-0.132 ± 0.014	-1.08	-0.36
5.0	(1.59 ± 0.14)×10^{-4}	-0.051 ± 0.001	-0.179 ± 0.006	-1.11	-0.36

Figure 45 shows the polarization response of alloy 625 in the NiCrFeMoNb solution at concentrations of 3.0, 3.5, and 4.5 m. Unlike the NiCrFeMo solution, the NiCrFeMoNb solutions had an active to passive transition at all concentrations investigated. In addition, the OCPs in this solution were approximately 0.10 V lower than the NiCrFeMo solutions, consistent with activation. Values of i_{crit} increased significantly with concentration. For example, from $i_{crit} = (1.15\pm0.06)\times10^{-5}$ A/cm^2 at the 3.0 m concentration and $i_{crit}=(2.96\pm0.12)\times10^{-3}$ A/cm^2 at the 4.5 m concentration. Similarly, the pH$_{OLI}$ values of the solutions became more aggressive as the concentration of the solutions increased. pH$_{meas}$ values were more negative than the pH$_{OLI}$ values, and did not follow a linear decrease. Table 9 presents a summary of the electrochemical parameters of polarization responses from 3.0 m to 5.0 m concentrations for the NiCrFeMoNb solutions.

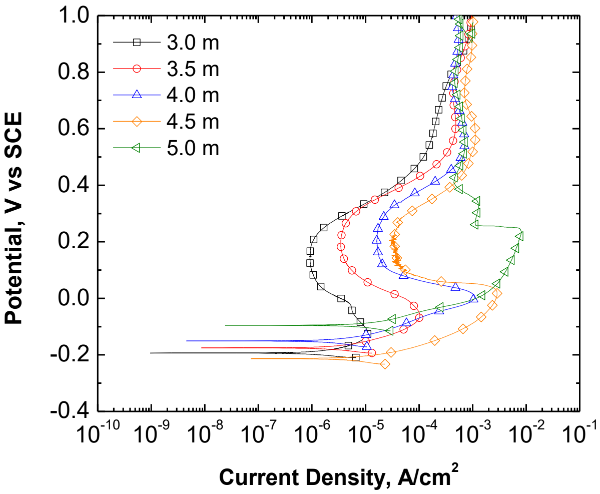

Figure 45. Polarization response of nickel alloy 625 at different concentrations of NiCrFeMoNb solutions.

Table 9. Average electrochemical parameters of polarization responses at different concentrations in molality of NiCrFeMoNb solutions.

m	**i_{crit} A/cm^2**	**E_{crit} V vs SCE**	**OCP V vs SCE**	**pH$_{meas}$**	**pH$_{OLI}$**
3.0	$(1.15 \pm 0.06)\times10^{-5}$	-0.117 ± 0.006	-0.192 ± 0.004	-0.96	-0.327
3.5	$(1.12 \pm 0.11)\times10^{-4}$	-0.061 ± 0.002	-0.174 ± 0.001	-0.69	-0.489
4.0	$(1.11 \pm 0.06)\times10^{-3}$	-0.024 ± 0.005	-0.192 ± 0.005	-1.36	-0.622
4.5	$(2.96 \pm 0.12)\times10^{-3}$	0.015 ± 0.003	-0.217 ± 0.006	-1.25	-0.740
5.0	$(7.36 \pm 1.09)\times10^{-3}$	0.227 ± 0.013	-0.107 ± 0.017	-1.64	-0.857

Figure 46 presents the polarization data for the NiCrFe equivalent chloride solutions at concentrations of 3.0 m and 5.0 m. The OCP values of the 3.0 m and 5.0 m solutions were found to be within the range of 0.320 to 0.350 V vs SCE, and the pH_{meas} values were within the range of ~0.03 to ~0.78, as summarized in Table 10. No active to passive transition was observed.

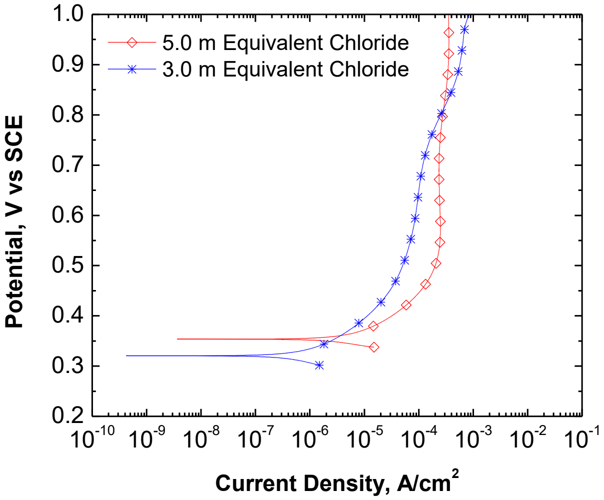

Figure 46. Comparison between 3.0 m and 5.0 m NiCrFe Equivalent Chloride Solutions

Table 10. Average electrochemical parameters of polarization responses at different concentrations in molality of NiCrFe equivalent chloride solutions.

m	i_{crit} A/cm²	E_{crit} V vs SCE	OCP V vs SCE	pH_{meas}	pH_{OLI}
3.0	NA	NA	0.321 ± 0.018	-0.03	0.388
5.0	NA	NA	0.354 ± 0.007	-0.78	0.479

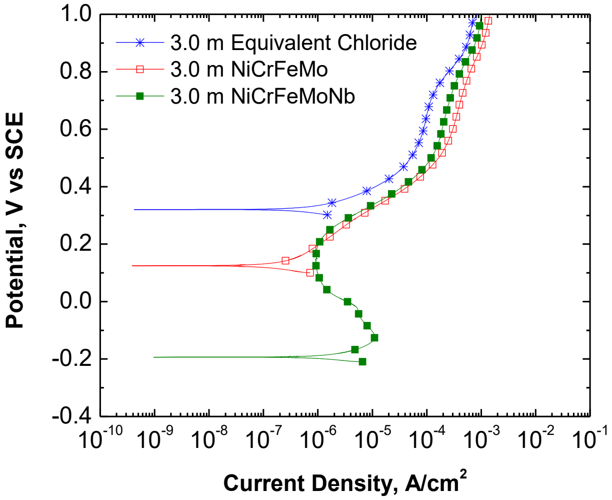

Figure 47. Comparison between 3.0 m NiCrFeMo and NiCrFeMoNb solutions and 3.0 m NiCrFe equivalent chloride solutions.

All three solutions, NiCrFe, NiCrFeMo, and NiCrFeMoNb, are compared in Figure 47 for a concentration of 3.0 m. Figure 44 shows that the addition of $MoCl_3$ and $NbCl_5$ to the solution results in a decrease in OCP and reveals an active to passive transition. The mechanism responsible for this increase in peak current density will be one of the focuses of the discussion.

3.1.3. ICP Analysis of the 3.0 m Stoichiometric Crevice Solution

During the preparation of artificial crevice solutions, some solids precipitated out when adding Mo and Nb to the solution. Even after mixing these solutions up to 1 week, the separation into two phases was found: a dark red precipitate at the bottom of the electrochemical cell, and a dark green solution at the top. ICP analysis of these two phases (as formed in a 3.0 m stoichiometric solution) was performed, and results in wt% are shown in Figure 60. The composition of the dark green solution was found to be rich in Ni and Cr, with a small amount of Mo dissolved in solution. The precipitate composition was also rich in Ni and Cr content, but also showed higher Mo than the solution, and nearly 25wt% Nb. The results of the solid precipitates agree with a high precipitation of Mo and Nb within the RCA specimens (Figure 48).

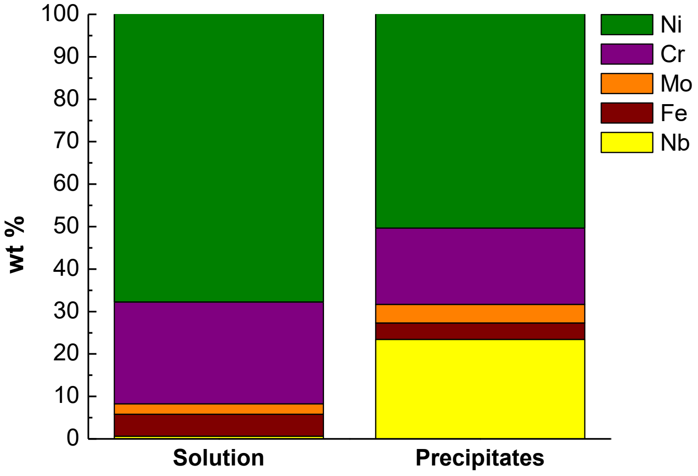

Figure 48. Results from ICP analysis of the solution and the precipitates that formed in the 3.0 m NiCrFeMoNb metal salt solution.

3.1.4. HCl-based Solutions

To account only for the acidification (low pH) effect on the polarization responses, HCl-based solutions were also studied. The polarization responses for a variety of HCl molal concentrations ranging from 0.10 m to 5.60 m are shown in Figure 49. Table 11 shows the corresponding OLI calculated values for these different concentrations and the corresponding critical peak current densities (i_{crit}).

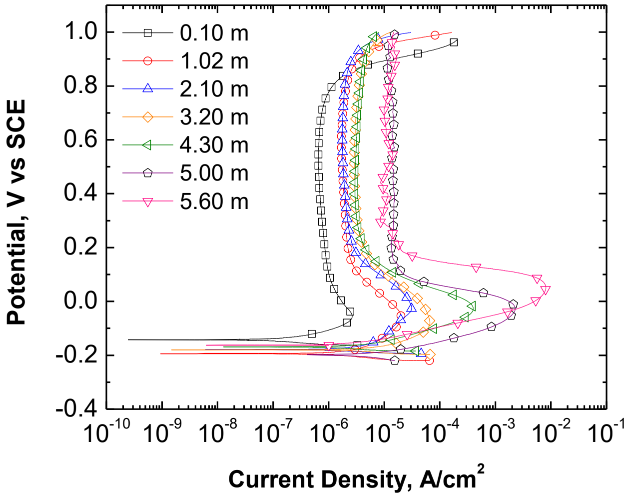

Figure 49. Polarization responses of nickel alloy 625 in a variety of HCl-based solutions ranging from 0.1 to 5.6 molal.

Table 11. Electrochemical parameters of polarization responses at different concentrations of stoichiometric NiCrFeMoNb solutions.

m	**i_{crit} A/cm^2**	**E_{crit} V vs SCE**	**i_{pass} A/cm^2**	**OCP, V vs SCE**	**pH$_{OLI}$**
0.10	2.65×10^{-6}	-0.054	7.36×10^{-7}	-0.142	1.10
1.02	2.08×10^{-5}	-0.057	1.71×10^{-6}	-0.200	0.07
2.10	3.12×10^{-5}	-0.024	1.78×10^{-6}	-0.174	-0.37
3.20	6.62×10^{-5}	-0.079	3.01×10^{-6}	-0.176	-0.70
4.30	3.99×10^{-4}	-0.027	3.14×10^{-6}	-0.164	-1.00
5.00	2.27×10^{-3}	-0.026	1.12×10^{-5}	-0.199	-1.20
5.60	8.08×10^{-3}	-0.051	1.46×10^{-5}	-0.143	-1.28

In Figure 49, it is important to note that the appearance of an active to passive transition occurred between 0.1 m and 1.0 m. Active to passive transitions in a 0.1 M HCl-based solution have also been reported for alloy 625 and alloy 22 [22], [71]. As it is summarized in Table 11, it was found that by increasing the molal concentration of HCl-based solutions, the pH values decreased and the i_{crit} values increased, as was reported by Lillard et. al [22]. The increase of i_{crit} with the molal concentration of HCl obeyed the relationship $i_{crit}=2\times10^{-6}\ e^{1.33m}$. The E_{crit} values appear to remain unchanged as the concentration of HCl increases. The average E_{crit} was -0.045±0.021 V vs SCE. The passive current densities (i_{pass}) were found to be dependent on the molal concentration of the HCl-based solutions. The lowest i_{pass} observed was at 0.1 m HCl, as is expected since this is the solution with the lowest pH and Cl^- content. At concentrations from 1.02 to 4.3 m, the passive current densities were within the same order of magnitude $\sim10^{-6}$ A/cm^2. An increase of almost one order of magnitude in i_{pass} was seen at 5.0 and 5.6 m, reaching currents on the order of $\sim10^{-5}$ A/cm^2.

3.2. OLI Calculation Results

3.2.1. OLI Calculations for Metal Salt Solutions

OLI software was used for predicting the pH-values and the speciation of the metal salts simulants at different concentrations. Concentrations ranging from 0.5 to 9.0 m, in steps of 0.5 m, were selected for this study. Figure 50 shows the solid species that precipitate at 25 °C. The majority of Mo(III) added in solution precipitated as MoO_2 from the 0.5 to 3.0 m range. As the concentration of the metal solution increased from 3.5 up to 7.0 m, the precipitation of MoO_2 decreased significantly. Based on the Pourbaix diagram (Figure 1), the decrease in MoO_2 was consistent with a critical pH of -0.283, moving from the MoO_2 to the Mo^{3+} region. Similarly, the majority of Nb(V) added in solution appeared as Nb_2O_5 precipitation over the full range of dissolved alloy. Although there is some precipitation of MoO_2 and Nb_2O_5 during the full range of concentration, the solubility limit of the metal salt solution was associated with the precipitation of $NiCl_2{\cdot}6H_2O$. The solubility limit is reached when the amount of dissolved alloy reaches 5.5 m, as it is illustrated in Figure 50. The solution's calculated pH decreases rapidly and reaches negative pH when exceeding more than 2.0 m concentration of metal salt solution.

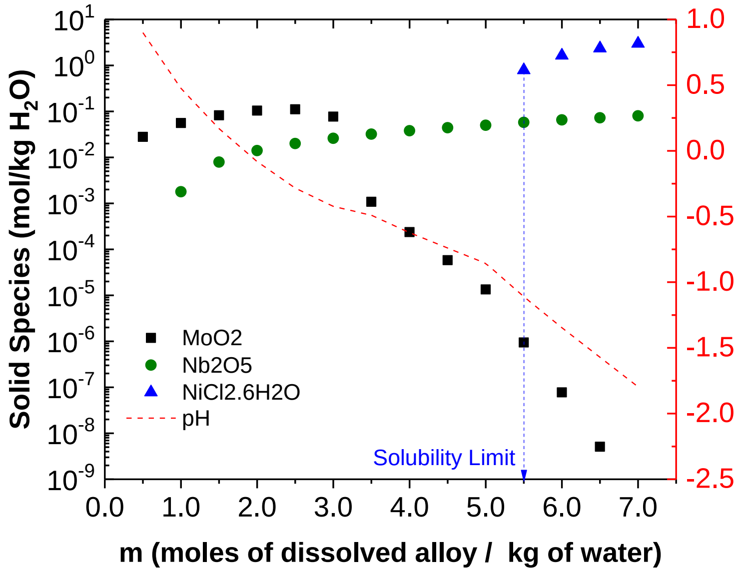

Figure 50. Predicted solid species of metal salts, containing $NiCl_2$, $CrCl_3$, $NiCl_2$, $MoCl_3$ and [0.5 Nb_2O_5+5 HCl], that follow a stoichiometric dissolution to that of alloy 625 at 25°C.

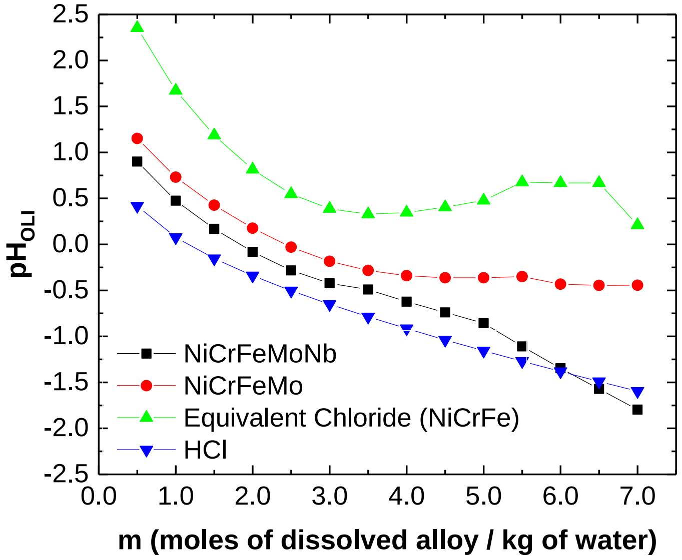

Figure 51. Calculated pH for NiCrFeMoNb, NiCrFeMo and NiCrFe equivalent chloride content solutions as a function of molal concentration using OLI software.

The predicted pH values for stoichiometric (NiCrFeMoNb and NiCrFeMo) solutions and equivalent chloride (NiCrFe) solutions from the OLI software are shown in Figure 51 as a function of metal salt concentration. For any given concentration, e.g. 4.0 m, NiCrFe solution has the lowest pH. Addition of $MoCl_3$ to the solution decreases the pH, for example at 4.0 m the NiCrFeMo solution pH is approximately 0.25 while the NiCrFe solution pH is approximately 0.5. Addition of niobium (V) chloride, as [Nb_2O_5+5HCl], decreases further the pH to ~ -0.6. These results suggest that the speciation of metal cations, the increase of chloride content, or both are directly affecting the aggressivity of the metal salt solution. The pH values of the HCl-based solution at different molar concentrations are also illustrated in Figure 51 as a comparison. Within the range of 3.0 m and 5.0 m concentration, the pH of the HCl-based solutions is lower than the pH of the metal salt solutions at the same molal concentrations.

The speciation of each metal salt was studied separately to identify its contribution to the overall pH. The calculations for $CrCl_3$, $NiCl_2$, $FeCl_2$, $MoCl_3$, and [0.5 Nb2O5 + 5HCl] at 25°C are shown in Figures 52-56. The number of moles of the element used for each simulation is based on the percentage of alloy 625 that is made of each element. For example, alloy 625 is 62 %mol Ni, so the "1 mole" simulation of Ni was run using 0.62 m of Ni. Likewise, as alloy 625 is 6 %mol Mo, the "2 mole" simulation for Mo was run using 2*0.06 m of Mo, or 0.16 m. As seen in Figure 52, as the concentration of the $CrCl_3$ increases, the pH approaches zero. The hydrolysis reaction that creates the hydrolyzed form of Cr, $CrOH^{+2}$, also creates H_3O^{+1}, which causes the rapid decrease of pH in this solution. In Figure 53, a weaker tendency to lower the pH is observed since the hydrolyzed form of Ni, $NiOH^+$, is several orders of magnitude lower than $CrOH^{+2}$. The pH stays at an average value of 5. These results suggest that the hydrolysis of Ni^{2+} does not contribute significantly to the pH of the environment. The solubility limit of this solution is reached at ~5.3 m with the precipitation of $NiCl_2{\cdot}6H_2O$. In figure 54, a similar trend to that of $NiCl_2$ was obtained for the speciation of $FeCl_2$. Since Fe^{+2} has less tendency to hydrolyze, Fe^{2+} does not contribute significantly to the decrease of pH in the solution. As shown in Figure 55, most of the $MoCl_3$ precipitated as MoO_2; however, a small amount of Mo^{3+} hydrolyzed and contributed to lowering the pH to negative values. Finally, for the anodic dissolution of Nb in Figure 56 (which was approximated by the formation of [0.5 Nb_2O_5 +5 HCl] as described above), the aqueous $HNbO_3$ and the solid Nb_2O_5 are the only two calculated stable species. The formation of [0.5 Nb_2O_5 + 5 HCl] leads to a substantial decrease of pH. These results suggest that during the dissolution of alloy 625, there is no single species that can be attributed for solution acidification within an occluded region.

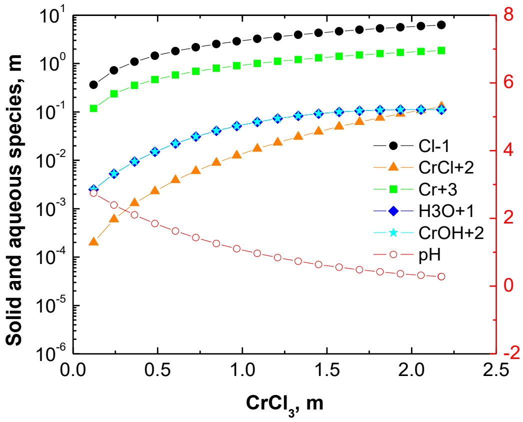

Figure 52. Speciation of $CrCl_3$ at different molal concentrations.

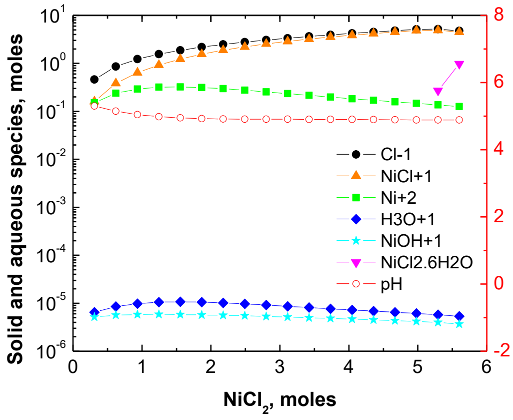

Figure 53. Speciation of $NiCl_2$ at different molal concentrations.

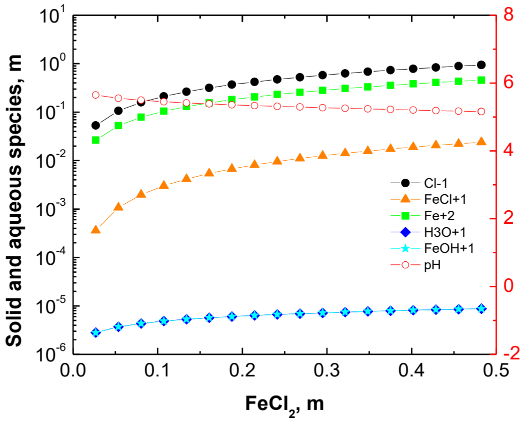

Figure 54. Speciation of FeCl2 at different molal concentrations.

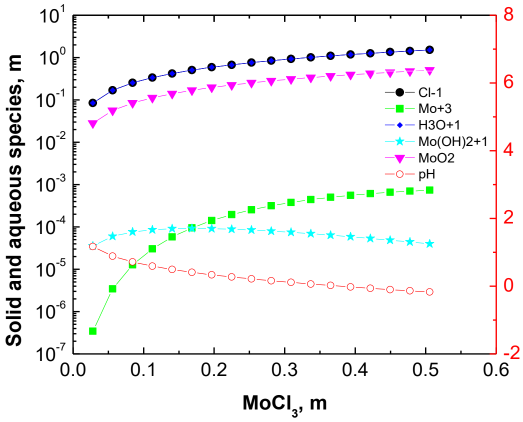

Figure 55. Speciation of MoCl3 at different molal concentrations.

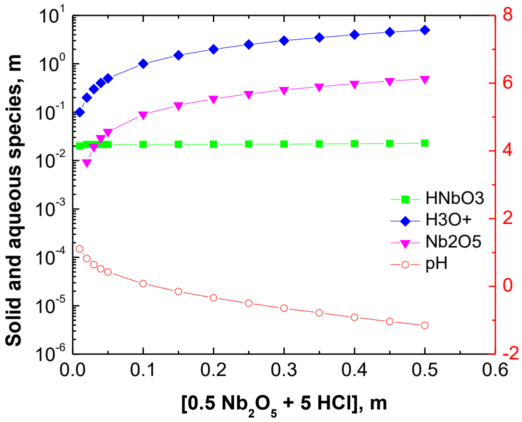

Figure 56. Speciation of the pseudo NiCl5 at different molal concentrations.

The speciation of all three metal salt solutions under study, i.e. the NiCrFe, NiCrFeMo, and NiCrFeMoNb solutions, were also run to obtain an estimation of the different aqueous species in solution, as well as information regarding the activity coefficients and pH values as the metal concentration increases. Some of the main results from the NiCrFeMoNb speciation are summarized in Figures 57-60.

Figure 57 shows the H_3O^+ concentrations for each of the metal salt solutions. The concentration of H_3O^+ is directly related to the hydrolysis reactions given by Cr, Mo, and Nb cations in solution. The H_3O^+ concentration is highest in the NiCrFeMoNb solution, followed by NiCrFeMo, and then the equivalent chloride NiCrFe solution, which displayed the lowest H_3O^+ concentration values. These results suggest that the addition of $MoCl_3$ and $NbCl_5$ in solution increase the H_3O^+ as a result of hydrolysis reactions.

The activity coefficient of H_3O^+ for all metal salt solutions is shown in Figure 58. The activity coefficients of the metal salt solutions remain nearly the same at concentrations below 2.5 m, after which they begin to deviate. At concentrations above 2.5 m, NiCrFeMoNb presents a higher predicted activity coefficient than the other solutions.

Figure 59 compares the calculated free Cl^- content in solution, this being the chloride content that is not tied up in the form of metal complexes. The NiCrFeMoNb shows the highest free Cl^- content in solution, followed by the NiCrFeMo solution and then the equivalent chloride content NiCrFe solution. Even though the NiCrFeMoNb and the equivalent chloride solution have the same amount of total chloride, the free chloride is higher in the NiCrFeMoNb solution. Free chloride dissolved in solution increases as Mo and Nb are added to the solution. The pH also decreases as Mo and Nb are increased, as was shown above. These results suggest that as the pH decreases in these solutions, the cation forms e.g. Ni^{2+}, Cr^{3+}, Fe^{2+} become more stable than their respective chloride forms, and an increase in the free chloride values is observed. The sudden decrease of chloride content at 5.5 m is due to the $NiCl_2 \cdot 6H_2O$ precipitation.

Results from Figure 51 and 56 shows that the equivalent chloride solution has less free Cl in solution and higher pH values; conversely the NiCrFeMoNb solution has the highest free Cl^- content in solution and the lowest pH values from within the metal salt solutions. Of all metal cations in solution, the concentration of Mo^{3+} showed the most significant changes in its molal concentrations, as is illustrated in Figure 60. In the case of the NiCrFeMo solution, the concentration of Mo^{3+} in solution started to increase at 2.5 m, while for the NiCrFeMoNb solution the Mo^{3+} concentration started to increase at 2.0 m. These results suggest that a critical pH value had been reached at these two concentrations, where the Mo^{3+} becomes stable. As will discussed later in this study, it was found that a critical concentration of Mo^{3+} in solution plays a key role in the manifestation of an active to passive transition in nickel alloy 625.

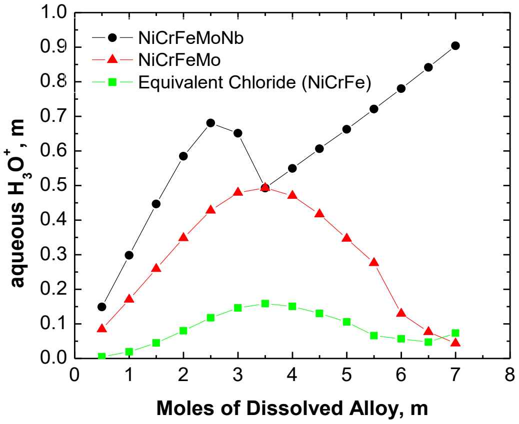

Figure 57. Moles of H_3O^+ in solution.

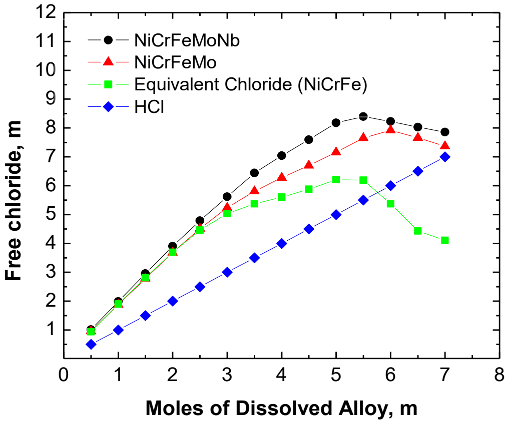

Figure 59. Free chloride concentration in the different metal salt solutions.

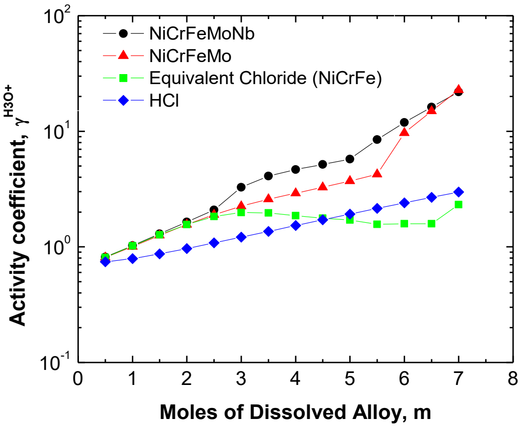

Figure 58. Activity coefficient of H_3O^+

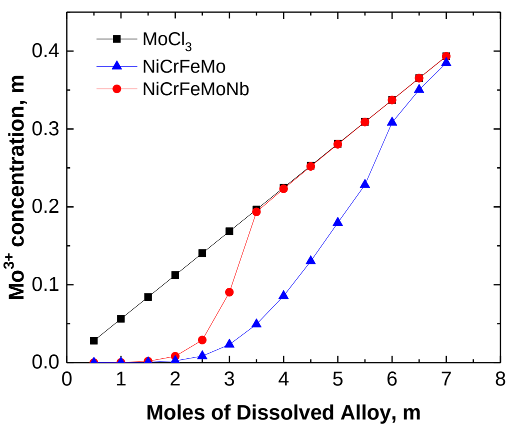

Figure 60. Mo^{3+} content.

3.3. Crevice Damage Propagation and Current vs Time Responses over Time

3.3.1. Recording Crevice Corrosion Damage in RCAs

A time-lapse video was recorded for a specimen that was polarized at 300 mV vs SCE for a total period of 60 hours, and the corresponding *I vs t* curve is shown in Figure 61. The evolution of the crevice corrosion damage is shown in a sequence of images in Figure 62, and the corresponding current values are shown by the red data points in Figure 61.

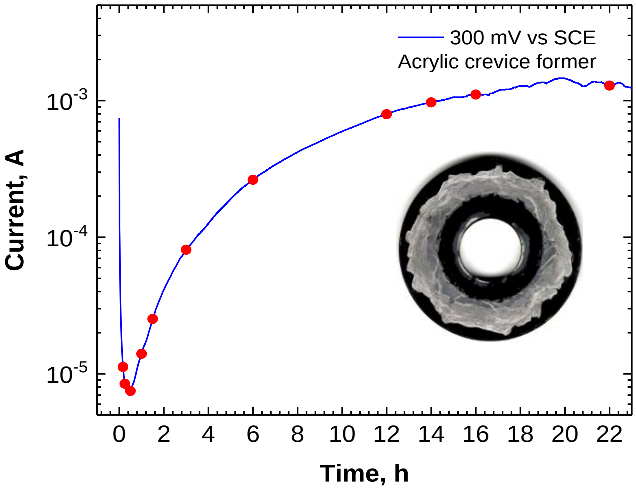

Figure 61. Current vs time curve obtained at 300 mV vs SCE and 60 hours. Only the first 23 hours of anodic polarization are shown.

As it is shown in Figure 58, the *I vs t* curves are characterized by three different time periods. At early times, the current decays rapidly from a relatively high value of the order of 10^{-3}A to a relatively constant value of the order of 10^{-5} A. This decrease in the total current can be attributed to the thickening of the passive film. This behavior would be also expected in a non-creviced specimen, since on the entire surface anodic and cathodic reactions occur, making possible the formation of passive film. The current produced by the specimen will be the passive current density i_{pass}. As is illustrated in the sequence of images in Figure 59, during this first period, the development of a CCS and the activation of crevice corrosion occurred near the crevice tip. By 10 min of immersion, minimal crevice corrosion attack was observed in the back of the crevice (it is difficult to observe this on the micrograph).

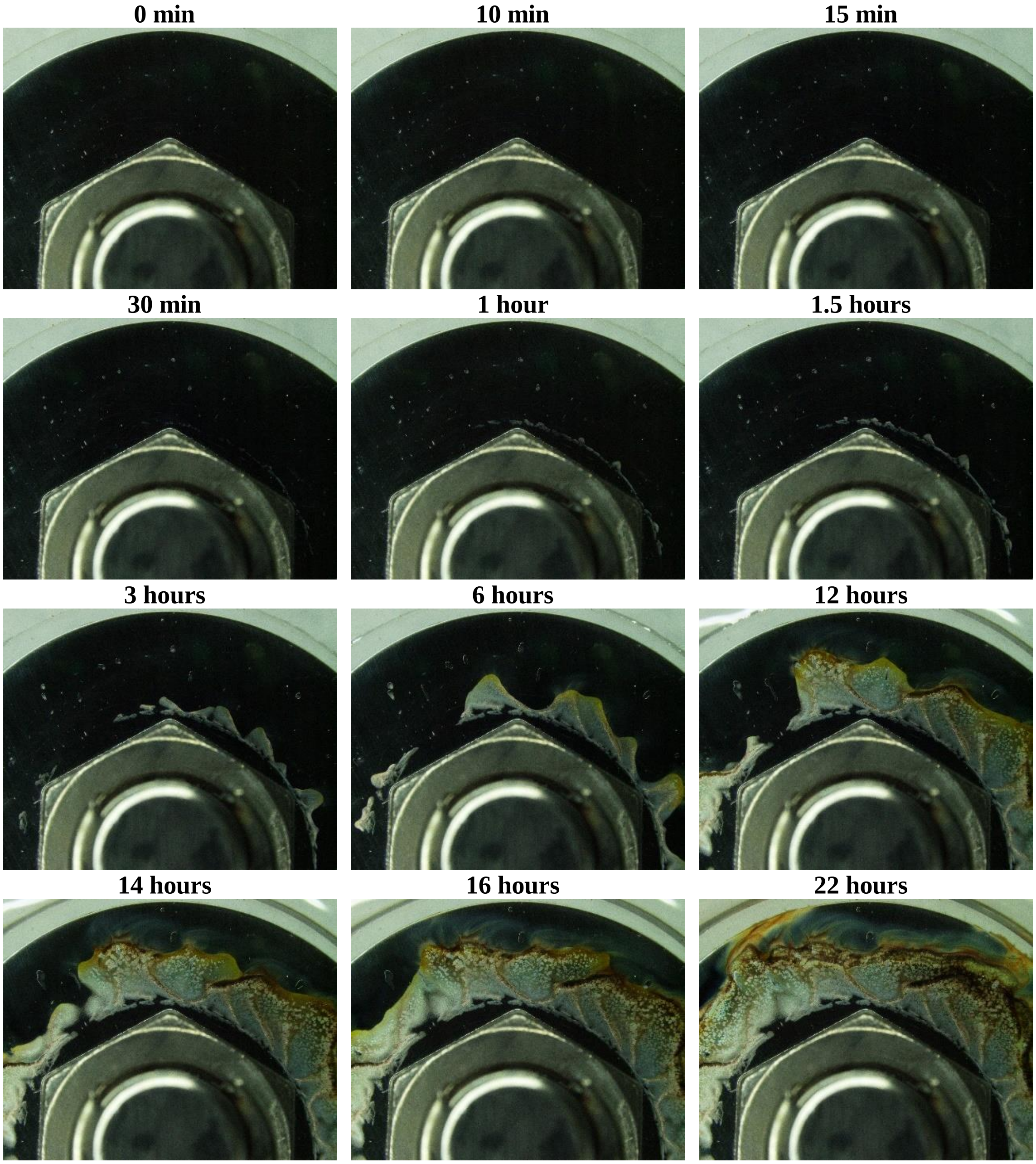

0 min **10 min** **15 min**

30 min **1 hour** **1.5 hours**

3 hours **6 hours** **12 hours**

14 hours **16 hours** **22 hours**

Figure 62. Sequence of crevice corrosion in clear RCA. The specimen was anodically polarized at 300 mV vs SCE for 60 hours.

From 10 to 30 minutes of immersion, a decrease in the total current is still observed, even though crevice corrosion has already initiated. This observation implies that the total anodic current produced by the initiation event is not large enough to overcome the passive current density value (i_{pass}) given by the alloy. Thus, during this first period of decrease in current, the passivation of the specimen occurs, followed by the breakdown of the passive film. At 30 min immersion, the total current *I* reached a minimum value, and an increase of current was detected on the *I vs t* curve. In the second period, the total current increases with time. From 30 minutes up to around 16 hours of immersion, the active front moves towards the crevice mouth and the current increases correspondingly, for example the current increased from 1.4×10^{-5} A at 1 hour to 2.64×10^{-4} A at 6 hours. After a critical distance near the crevice mouth is reached, at approximately 22 hours of immersion, crevice corrosion stops its outward movement and a maximum current value of 1.46×10^{-3} A is obtained. The average critical distance (x_{crit}) reached was 2665 μm from the crevice mouth. A third period follows, characterized by a relatively constant current value of the order of 10^{-3} A, and from 22 hours up to 60 hours, crevice corrosion starts to move in the opposite direction back towards the crevice tip. From the sequence of images shown in Figure 62, the corroded area over time was calculated with the aid of image processing software.

3.3.2. Current vs time Curves at Different Applied Potentials

The current vs time (*I vs t*) responses for the set of metal-to-metal RCA experiments performed at 200 mV vs SCE and 5 ft-lb torque, run at exposure times ranging from 10 hours up to 1 week, are summarized in Figure 63. As was discussed above, these curves are characterized by three different time periods. At early times, the current decays rapidly from a relatively high value of the order of 10^{-2}A to a minimum current value (I_{min}) of the order of 10^{-5} to 10^{-4}A. In the second period, the current increases with time until the third period, characterized by a relatively constant current value (I_{lim}) of the order of 10^{-3} A, is reached. The current then appears to remain constant for the rest of the testing period, as shown by the red curve (1 week of exposure) in Figure 63. At some shorter immersion times, I_{lim} was not reached, and the highest current value recorded in the *I vs t* response is called the maximum current, I_{max}. A descriptive explanation of I_{min}, I_{max}, and I_{lim} are illustrated in Figure 63 (a).

The general features of this current response output were also observed for the other 3 sets of experiments, see Figures 61-63; however, there were differences in current magnitude and period timing between each of the sets (see Tables 12-15). For example, for the set of experiments performed at 100 mV vs SCE and 10 ft-lb, the first period typically lasted an average of 10.2 hours. For the 200 mV vs SCE and 10 ft-lb set, the first period lasted an average of 4.2 hours. For the 300 mV vs SCE and 10 ft-lb set, the first period lasted an average of 3.9 hours. During the third period, the current value over time remained relatively constant for the 200 mV vs SCE and 5ft-lb set and the 200 and 300 mV vs SCE and 10 ft-lb sets. For the 100 mV vs SCE and 10 ft-lb set, the current continued to increase over time in the third period, although to a much lesser extent than in the second period.

A summary of the critical parameters of the *I vs t* curves at different applied potentials and torque, such as the duration of each period, the average values of I_{min}, I_{max}, and I_{lim}, and the total charge passed (Q) are summarized in Tables 12-15.

Additionally, at times approaching the minimum current shown in the *I vs t* response, current transients were observed, see Figures 63-66. These current spikes were observed when sampling at a rate of one reading per every 10-100 seconds. At a higher sample acquisition rate (50 readings per second), the frequency of current spikes went down.

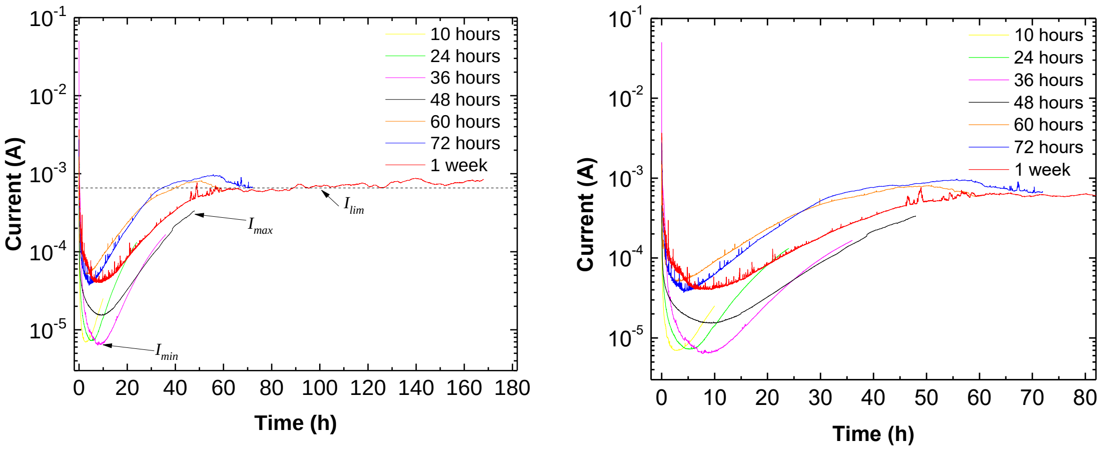

(a) (b)

Figure 63. I vs t *response of RCAs anodically polarized at 200 mV vs SCE at different exposure times. Applied torque 5 ft-lb. (a) All current vs time curves and (b) zoom in within the first 80 hours.*

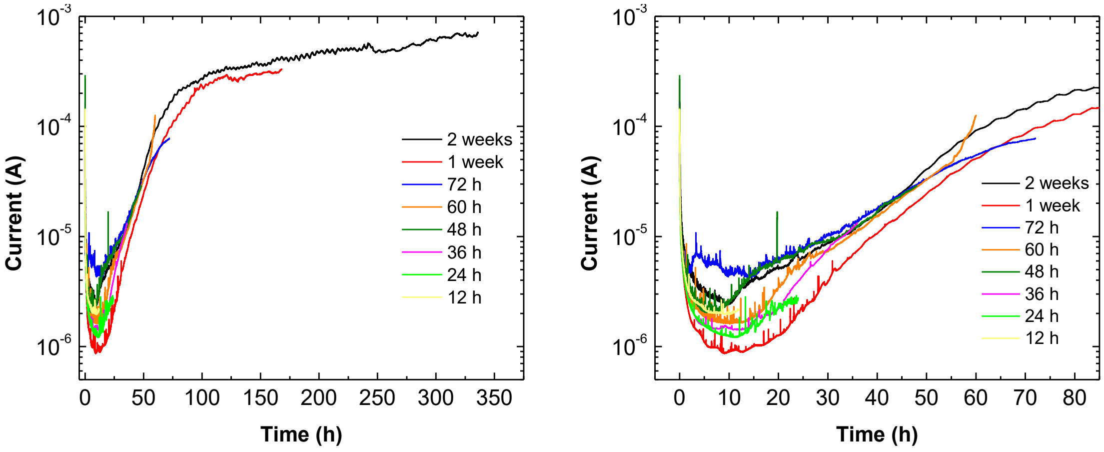

(a) (b)

Figure 64. I vs t *response of RCAs anodically polarized at 100 mV vs SCE at different exposure times. Applied torque 10 ft-lb. (a) All current vs time curves and (b) zoom in within the first 80 hours.*

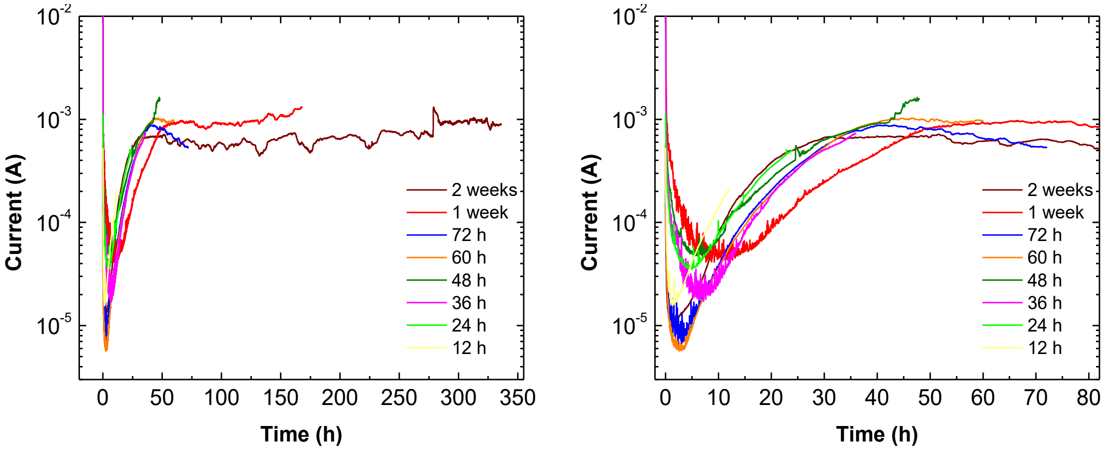

(a) (b)

Figure 65. I vs t *response of RCAs anodically polarized at 200 mV vs SCE at different exposure times. (a) All current vs time curves and (b) zoom in within the first 80 hours.*

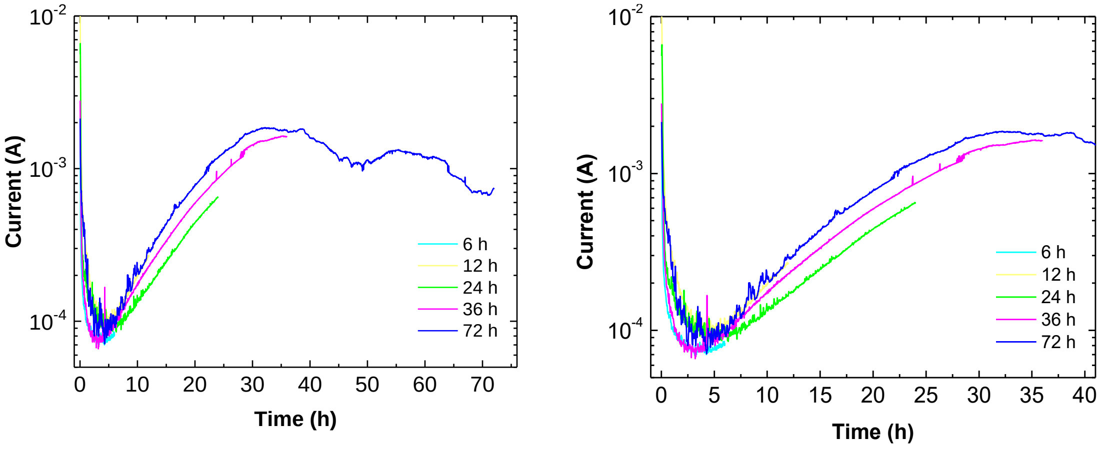

(a) (b)

Figure 66. I vs t *response of RCAs anodically polarized at 300 mV vs SCE at different exposure times. All current vs time curves and (b) zoom in within the first 40 hours.*

Table 12. Critical parameters of the I vs t responses for 200 mV vs SCE and 5 ft-lb at different immersion times.

Exposure time	**First Period**	**Second Period**	**Third Period**	I_{min}	I_{max}	I_{lim}	**Charge Passed**
h	**h**	**h**	**h**	**A**	**A**	**A**	**Q(C=A.s)**
10	2.9	7.1	0.0	6.98×10^{-6}	2.52×10^{-5}	-	0.30
24	5.3	18.7	0.0	7.23×10^{-6}	1.32×10^{-4}	-	3.20
36	7.7	28.3	0.0	6.36×10^{-6}	1.67×10^{-4}	-	5.40
48	9.3	38.7	0.0	1.53×10^{-5}	3.36×10^{-4}	-	15.70
60	5.0	41.6	13.4	5.08×10^{-5}	-	8.15×10^{-4}	46.30
72	4.1	42.5	25.4	3.70×10^{-5}	-	9.76×10^{-4}	137.80
168	9.3	54.2	104.5	4.03×10^{-5}	-	6.34×10^{-4}	332.10
Average	6.2±2.5	46.1±7.0		$(2.34\pm1.87)\times10^{-5}$	-	$(8.08\pm1.71)\times10^{-4}$	

Table 13. Critical parameters of the I vs t responses for 100 mV vs SCE and 10 ft-lb at different immersion times.

Exposure time	**First Period**	**Second Period**	**Third Period**	I_{min}	I_{lim}	I_{lim}	**Charge Passed**
h	**h**	**h**	**h**	**A**	**A**	**A**	**Q(C=A.s)**
12	9.8	2.2	0.0	1.95×10^{-6}	2.16×10^{-6}	-	0.13
24	11.2	12.8	0.0	1.21×10^{-6}	2.75×10^{-6}	-	0.19
36	12.2	23.8	0.0	1.42×10^{-6}	1.33×10^{-5}	-	0.54
48	5.4	42.6	0.0	2.04×10^{-6}	2.88×10^{-5}	-	1.66
60	10.1	49.9	0.0	1.62×10^{-6}	1.26×10^{-4}	-	3.67
72	14.5	57.5	0.0	4.24×10^{-6}	7.78×10^{-5}	-	6.58
168	9.1	89.1	69.8	8.64×10^{-7}		3.31×10^{-4}	90.64
336	9.6	95.9	230.5	2.35×10^{-6}		7.14×10^{-4}	437.40
Average	10.2±2.6	92.5±4.8		$(1.96\pm1.04)\times10^{-6}$		$(5.23\pm2.71)\times10^{-4}$	

Table 14. Critical parameters of the I vs t responses for 200 mV vs SCE and 10 ft-lb at different immersion times.

Exposure time	**First Period**	**Second Period**	**Third Period**	I_{min}	I_{max}	I_{lim}	**Charge Passed**
h	**h**	**h**	**h**	**A**	**A**	**A**	**Q(C=A.s)**
12	1.3	10.7	0.0	1.57×10^{-5}	2.09×10^{-4}	-	3.30
24	5.0	19.0	0.0	3.51×10^{-5}	5.07×10^{-4}	-	15.42
36	7.2	28.8	0.0	1.72×10^{-5}	7.38×10^{-4}	-	31.75
48	6.1	34.5	7.4	4.72×10^{-5}	-	1.58×10^{-3}	89.54
60	2.5	38.1	19.4	5.68×10^{-6}	-	1.03×10^{-3}	114.35
72	2.4	38.2	31.4	6.17×10^{-6}	-	8.77×10^{-4}	126.63
168	7.6	45.1	115.3	4.13×10^{-5}	-	1.33×10^{-3}	461.86
336	1.3	29.9	304.8	1.01×10^{-5}	-	1.31×10^{-3}	792.03
Average	4.2±2.6	37.2±5.6		$(2.23\pm1.65)\times10^{-5}$	-	$(1.23\pm0.28)\times10^{-3}$	

Table 15. Critical parameters of the I vs t responses for 300 mV vs SCE and 10 ft-lb at different immersion times.

Exposure time	**First Period**	**Second Period**	**Third Period**	I_{min}	I_{max}	I_{lim}	**Charge Passed**
h	**h**	**h**	**h**	**A**	**A**	**A**	**Q(C=A.s)**
6	3.6	2.4	0.0	6.80×10^{-5}	8.30×10^{-5}	-	2.33
12	3.8	8.3	0.0	9.40×10^{-5}	2.64×10^{-4}	-	10.87
24	4.7	19.3	0.0	8.30×10^{-5}	6.55×10^{-4}	-	24.02
36	3.2	32.8	0.0	6.60×10^{-5}	-	1.61×10^{-3}	85.92
72	4.3	31.9	35.8	7.01×10^{-5}	-	1.86×10^{-3}	261.57
Average	3.9±0.6	32.4±0.4		$(7.62\pm1.20)\times10^{-5}$	-	$(1.74\pm0.18)\times10^{-3}$	

Based on Figures 60-63 and Tables 12-15, it was found that at a single applied torque (10ft-lb), the duration of the first and second periods decrease when the applied potential increases. It is important to note that, for a single applied potential, the duration of the second period varies only slightly, so long as the specimen is immersed long enough to reach the third period. This indicates that the increase of current during the second period was dependent on time. Additionally, as the applied potential increased, the I_{min}, I_{max}, and I_{lim} values also increased. It was found that when increasing the applied torque from 5 ft-lb to 10 ft-lb, the duration of the first and second period were shorter. For example, the duration of the first period at 5ft-lb was on average 6.2 hours, compared to 4.2 hours for 10ft-lb. This in agreement with Oldfield and Sutton's model predicting that tighter crevices require less time for crevice corrosion initiation to occur [44].

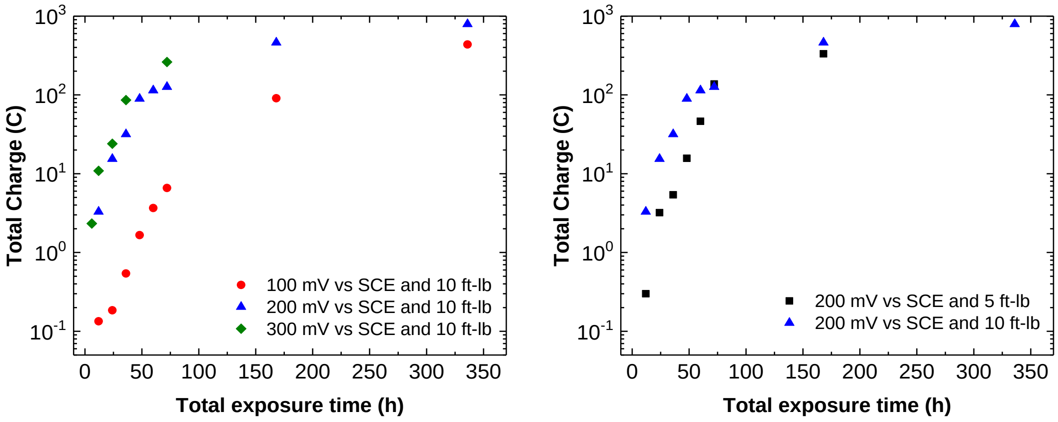

(a) (b)

Figure 67. Total charge passed during anodic polarization of the RCAs (a) at different applied potentials and (b) two different applied torques.

The effect of applied potential and applied torque on the total charge passed is also summarized in Figure 67. At higher applied potentials, the total charge passed increases. This is not surprising since higher currents were obtained at higher applied potentials. As the applied torque was increased from 5 ft-lb to 10 ft-lb (at the 200 mV), the total charge passed increased.

3.3.3. *Crevice Corrosion Damage Profiles*

Optical micrographs (obtained using optical profilometry) of the crevice faces and corresponding damage profiles for all four sets of RCA experiments are shown in Figures 68-71. Figure 68 shows the crevice damage profiles obtained at 100 mV vs SCE and 5 ft-lb at different exposure times. As seen in this figure, at 10 hours, the crevice corrosion initiation clearly occurred at the back of the crevice, far from the crevice mouth, and the crevice corrosion damage was minimal, only 0.5 m deep. It is likely that this etching would not have been noticeable had the assembly not been well polished. At 24 hours, the etching damage continued moving towards the crevice mouth. At 36 hours of immersion, the etching damage appeared to reach its closest point to the crevice mouth, and stopped its outward movement. At 48 hours of immersion, the crevice corrosion damage became deeper and more severe, penetrating into the face of the washer, as seen in the corresponding damage profile for this time. Penetration depths of around 11 microns were reached near the crevice mouth at 48 hours. Increasing the immersion time to 60 and 72 hours, the crevice corrosion damage continued going deeper into the specimen’s face. At longer immersion times, i.e. 1 week of immersion, the damage continued to deepen away from the crevice mouth, as is suggested by the formation of deeper peaks further from the crevice mouth. Penetration depths up to ~40 μm have been found for 1 week of immersion.

Similar trends in initiation and propagation of crevice corrosion were seen under all sets of experiments performed at 10 ft-lb torque (100, 200 and 300 mV vs SCE).

For both the 200 mV vs SCE and 10 ft-lb set and the 200 mV vs SCE and 5ft-lb set, only etching damage, with comparable penetration depth, occurred on the specimens at initial times (12 to 24 hours).

However, for exposure periods longer than 36 hours, the 200 mV vs SCE and 10 ft-lb set displayed crevice corrosion damage deeper into the crevice face than the 5ft-lb set. This suggests that at tighter torque, deeper crevice damage penetration is obtained.

At 300 mV vs SCE (Figure 71), crevice corrosion damage propagation occurred at faster rates than at 100 and 200 mV vs SCE. For example, for 100 mV vs SCE applied potential, a total time of 36 hours was required for initiating and propagating crevice damage, while at 300 mV, only 6 hours were needed to see crevice corrosion damage on the specimen. Additionally, at this higher potential, deeper crevice corrosion attack was observed: for a total immersion time of 72 hours, the maximum penetration depth found was ~50μm, compared to 4 and 33 μm for 100 and 200 mV applied potential sets, respectively.

Table 16 presents a summary of the effect of applied potential and applied torque on the progression of the active front (x_{crit}) and the penetrations depths (*d*) with time.

Table 16. Progression of active front (x_{crit}) and penetration depth (d) as a function of applied potential and applied torque.

Exposure time h	**100 mV 10 ft-lb**		**200 mV 10 ft-lb**		**300 mV 10 ft-lb**		**200 mV 5 ft-lb**	
	x_{crit}, μm	***d, μm***	***x_{crit}, μm***	***d, μm***	***x_{crit}, μm***	***d, μm***	***x_{crit}, μm***	***d, μm***
6					9280	-0.96		
10							7950	-0.33
12			6974	-0.49	6116	-0.41		
24			4168	-1.55	4049	-3.34	4166	-2.06
36	8975	-0.61	3278	-7.75	2226	-13.74	3241	-2.10
48	6594	-1.26	2978	-10.89			3764	-11.05
60	5137	-1.77	2727	-22.36			3095	-10.92
72	4233	-3.87	1517	-33.41	1018	-50.15	2996	-35.18
168	3081	-18.18	2064	-50.70			3591	-36.54
336	2662	-28.80						

As a general trend, it was found that as the applied potential increased, x_{crit} moved closer to the crevice mouth and deeper crevice corrosion damage was obtained. This is consistent with the higher charge passed values obtained at higher applied potentials. Regarding applied torque, x_{crit} moves closer to the crevice mouth and deeper crevice corrosion depths were obtained at 10 ft-lb than at 5 ft-lb.

3.3.3.1. Crevice corrosion damage profiles obtained at 200 mV and 5 ft-lb

10 hours

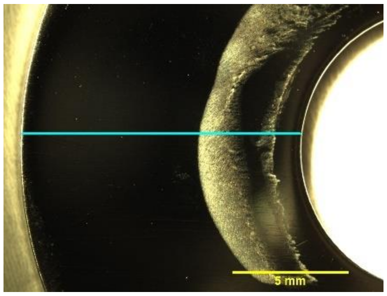

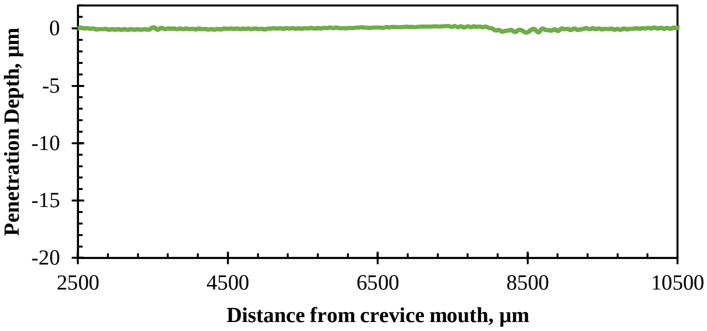

24 hours

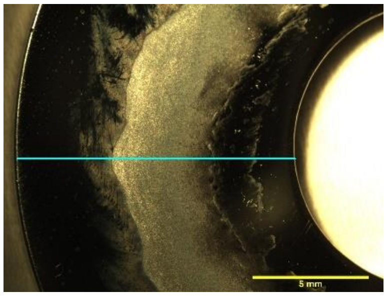

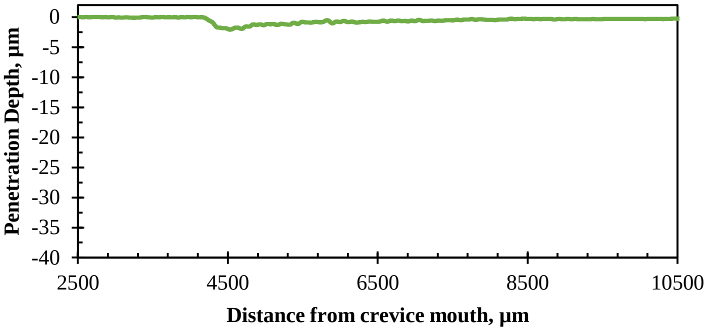

36 hours

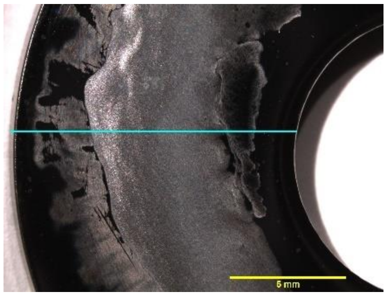

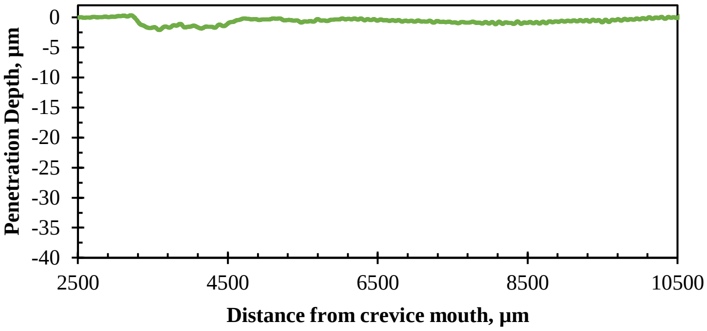

48 hours

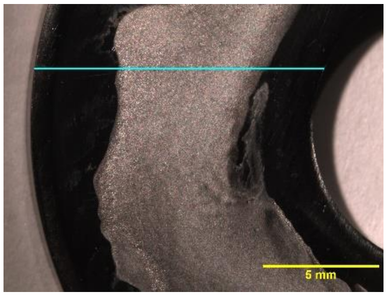

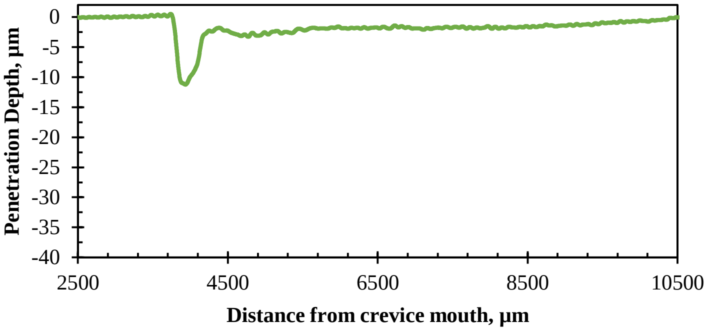

60 hours

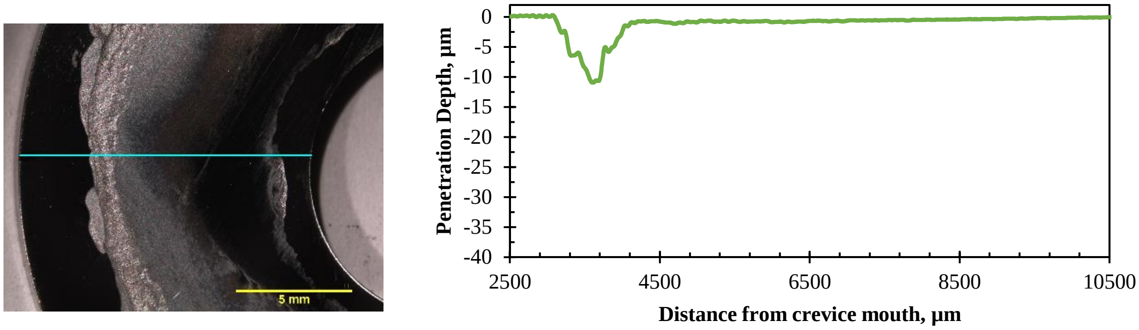

72 hours

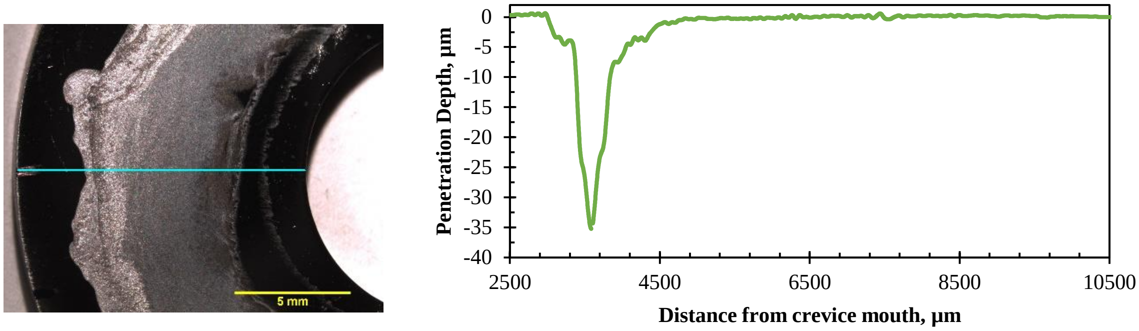

1 week

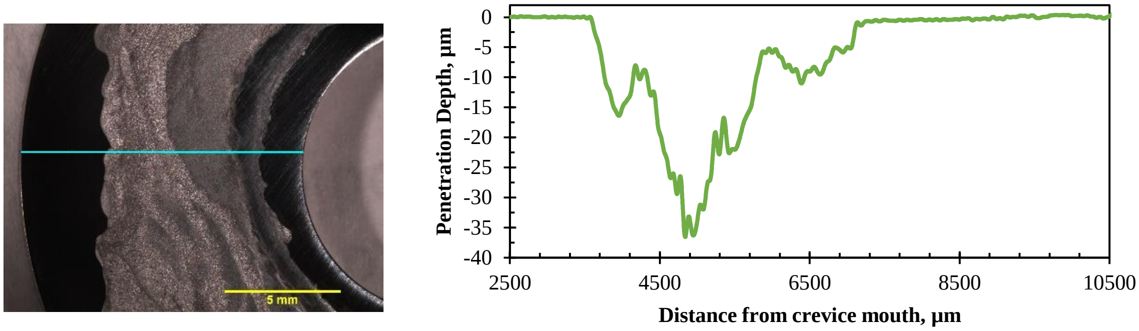

Figure 68. Optical micrographs of crevice faces and their corresponding crevice corrosion damage profiles of specimens polarized at 200 mV vs SCE and 5ft-lb torque.

3.3.3.2. *Crevice corrosion damage profiles obtained at 100 mV and 10 ft-lb*

36 hours

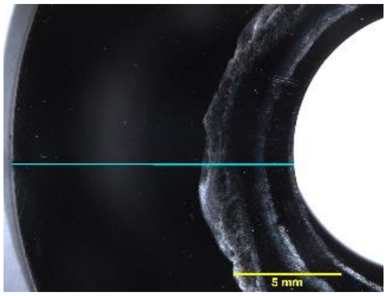

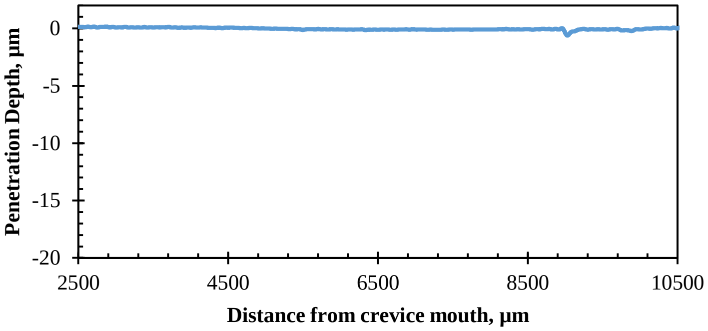

48 hours

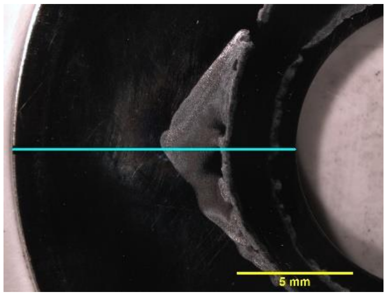

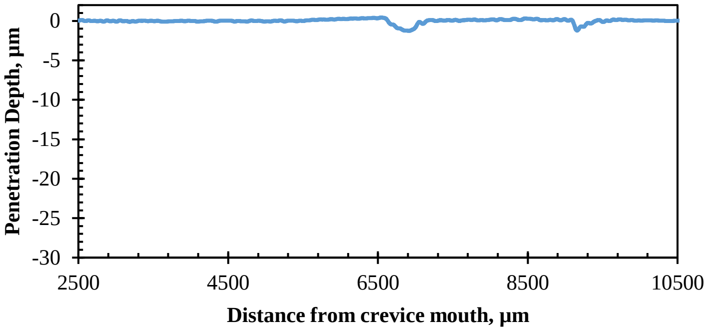

60 hours

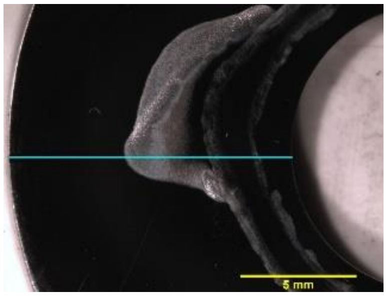

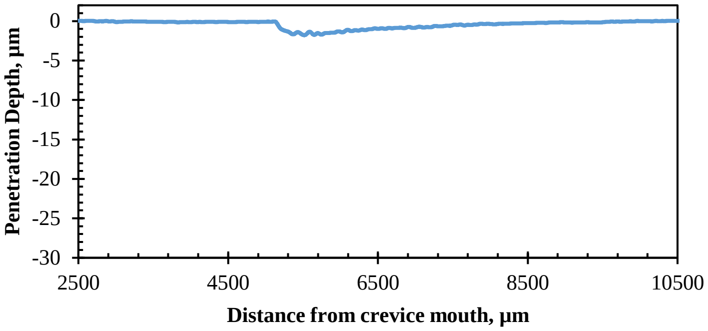

72 hours

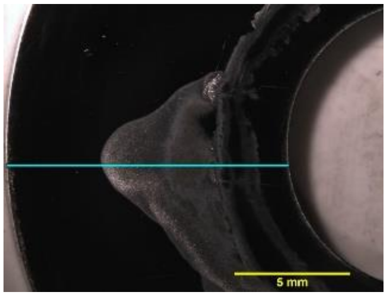

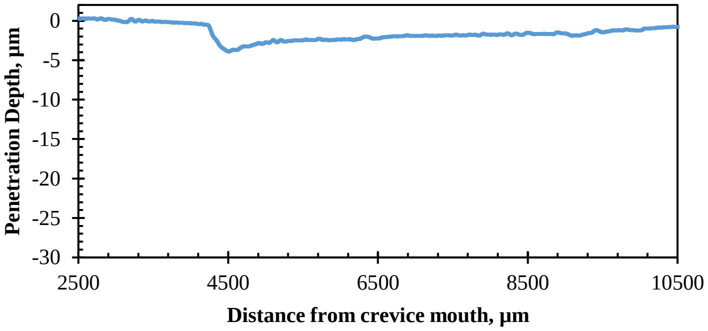

1 week

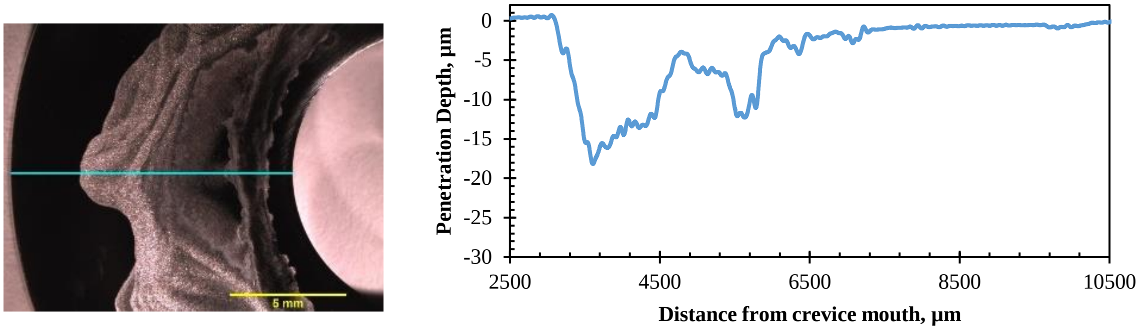

2 weeks

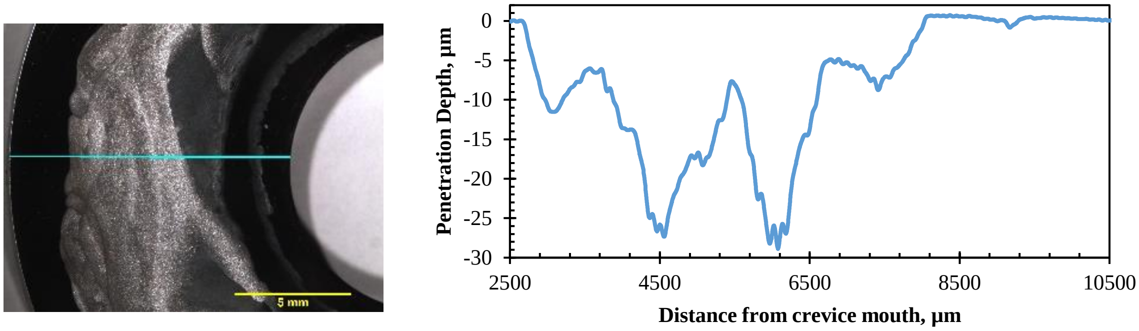

Figure 69. Optical micrographs of crevice faces and their corresponding crevice corrosion damage profiles of specimens polarized at 100 mV vs SCE. Applied torque: 10 ft-lb.

3.3.3.3. Crevice corrosion damage profiles obtained at 200 mV and 10 ft-lb

12 hours

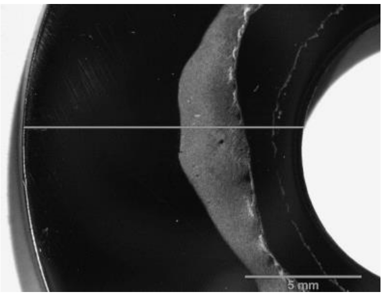

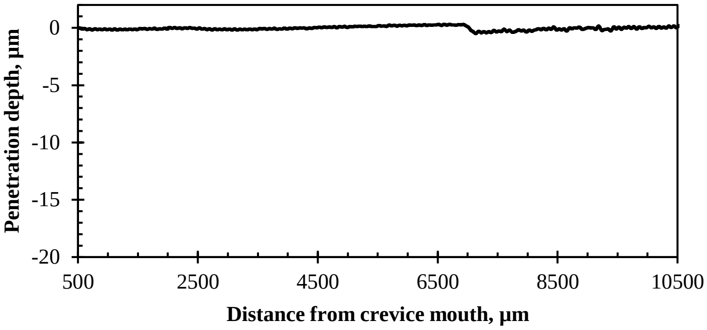

24 hours

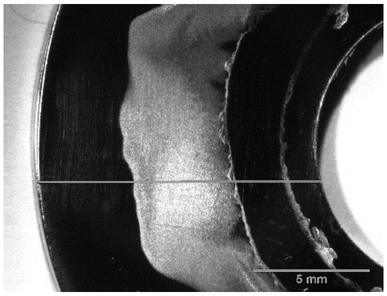

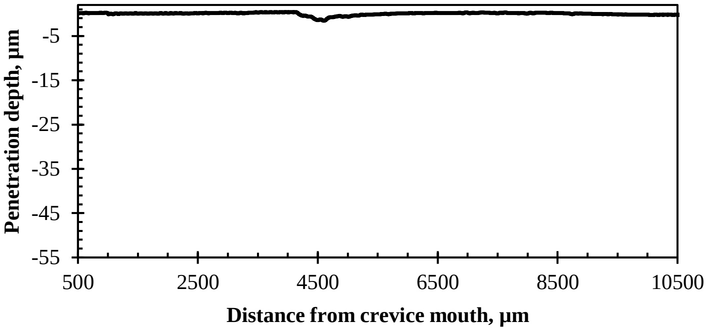

36 hours

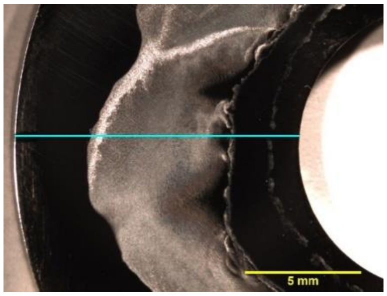

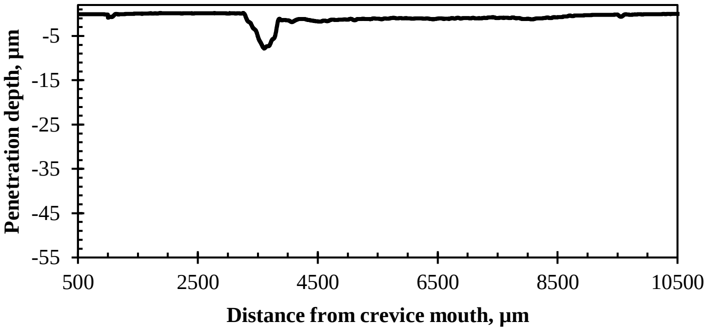

48 hours

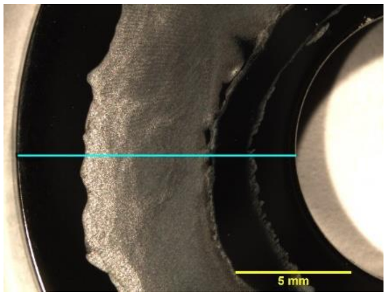

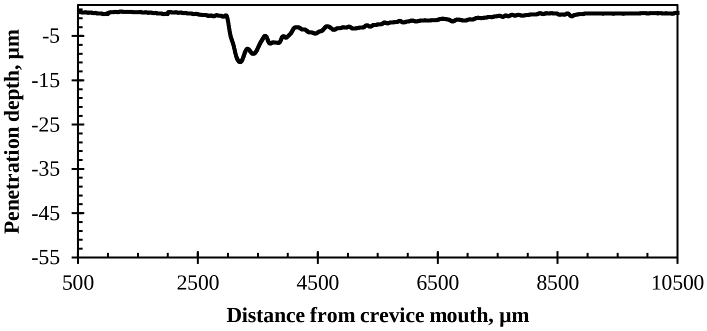

60 hours

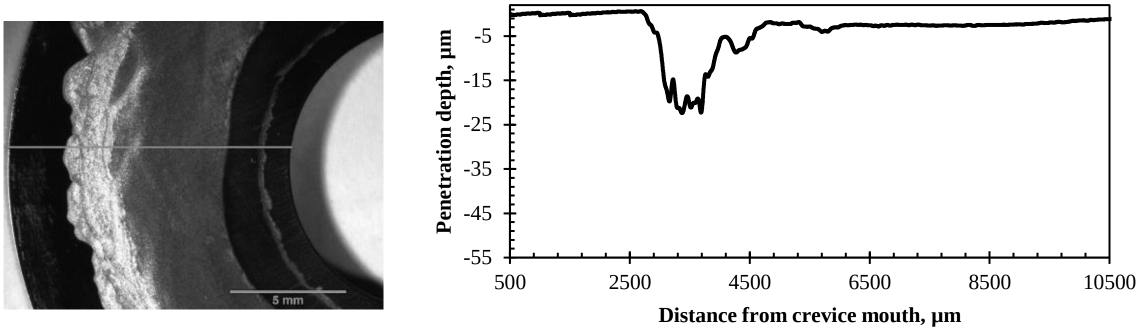

72 hours

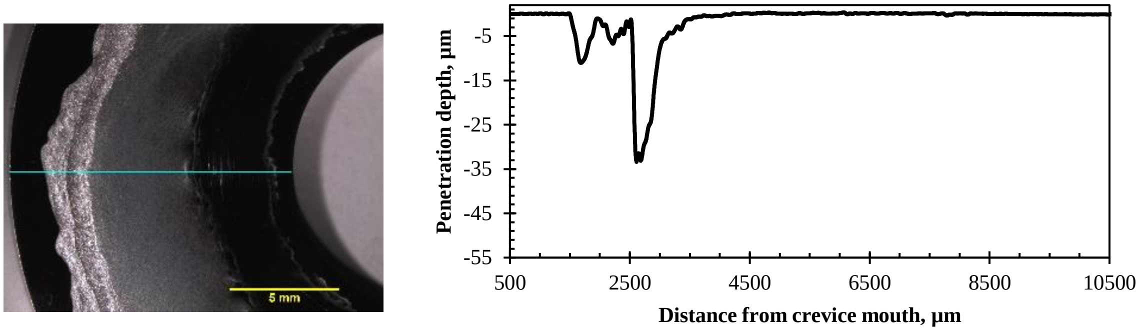

1 week

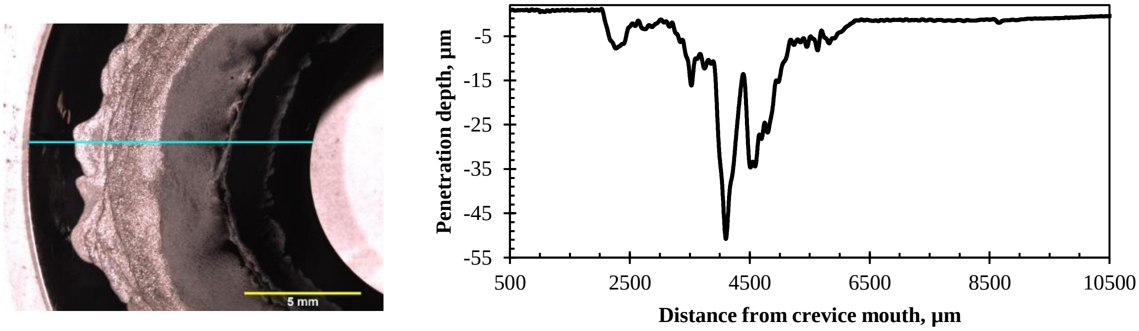

Figure 70. Optical micrographs of crevice faces and their corresponding crevice corrosion damage profiles of specimens polarized at 200 mV vs SCE.

3.3.3.4. *Crevice corrosion damage profiles obtained at 300 mV and10 ft-lb*

6 hours

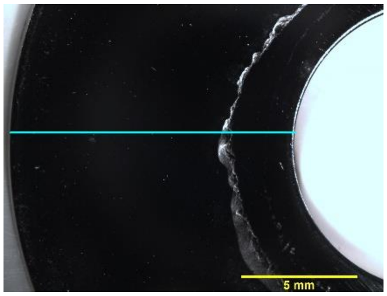

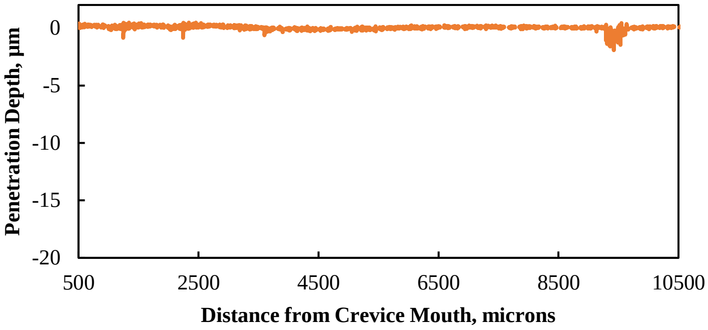

12 hours

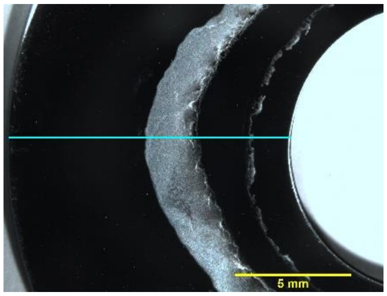

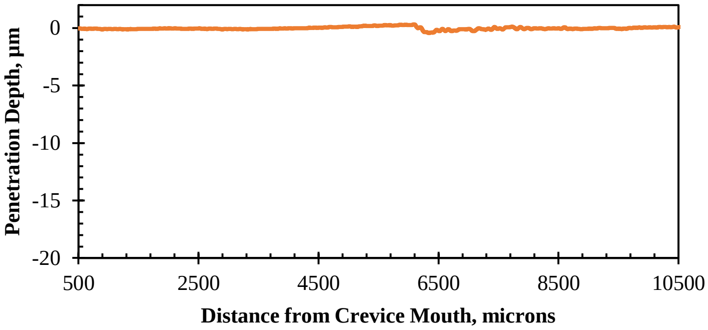

24 hours

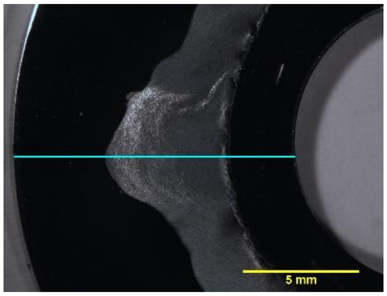

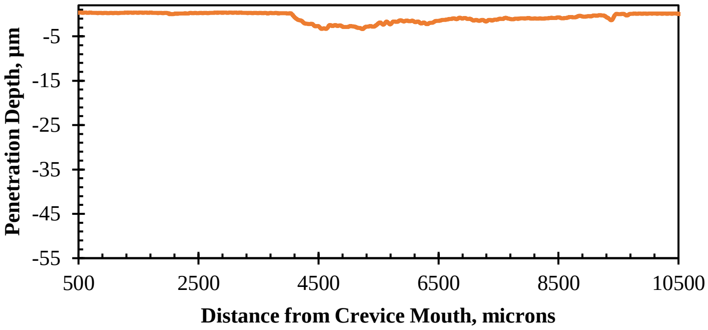

36 hours

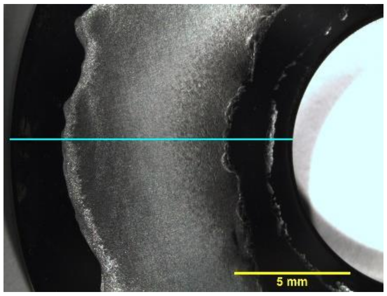

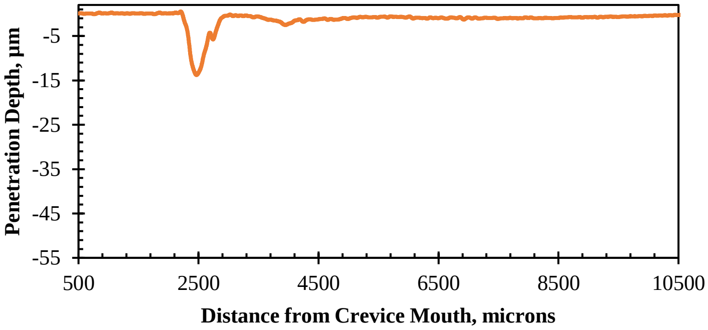

72 hours

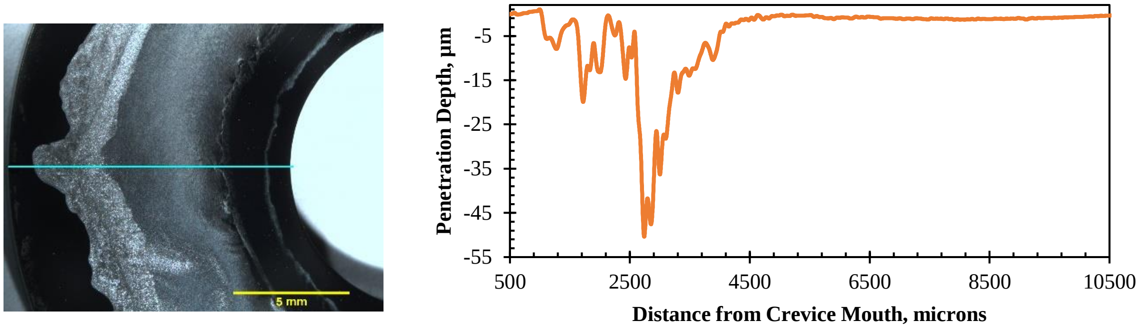

Figure 71. Optical micrographs of crevice faces and their corresponding crevice corrosion damage profiles of specimens polarized at 300 mV vs SCE. Applied torque: 10 ft-lb.

3.3.4. Morphology of Crevice Damage

Using an SEM image of a specimen corroded at 200 mV for a total immersion time of 72 hours, different regions along a scanline drawn on the optical micrograph shown in Figure 72(a) were characterized. A transition of crevice corrosion damage from etching damage to surface brightening is shown in Figures 72(b)-(d).The green and blue squares highlight characteristic regions of etching damage, and the orange square highlights a brightening (or polishing-like) surface morphology. Initially a series of micropits developed and these were aligned with the scratch marks arising from the specimen preparation (Figure 72(a)). At some point the local micropit density increased and coalesced, producing a grain boundary and grain orientation etching effect (Figure 72(b)). Over time, due to the presence of high crevice corrosion rates, further metal dissolution produced a more polished surface (Figure 72(c)).

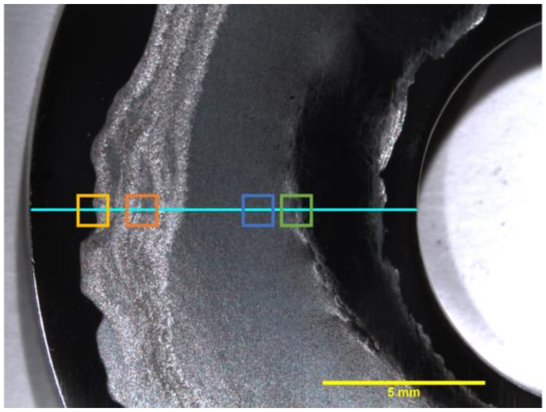

(a)

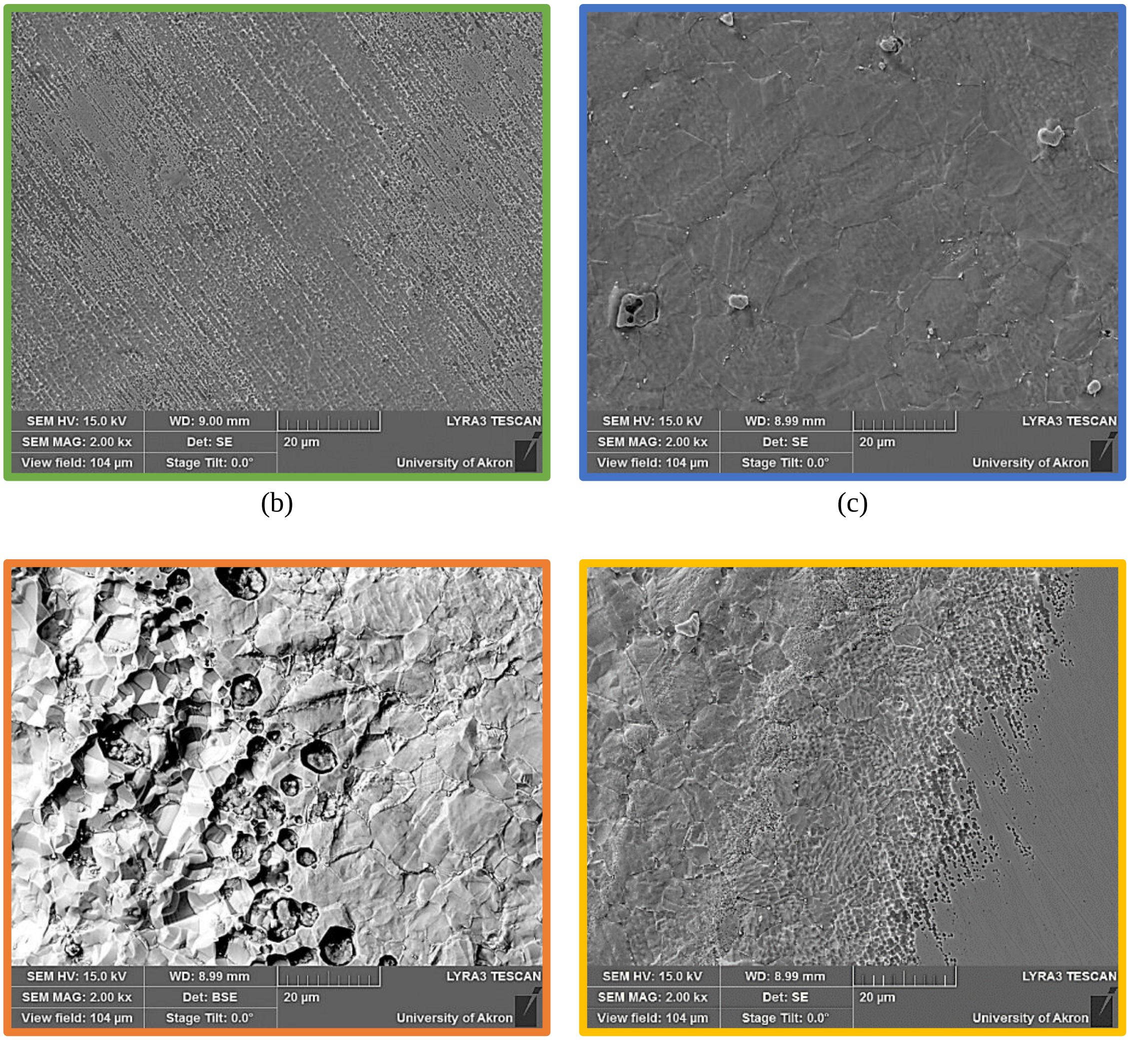

(b) (c)

(d) (e)

Figure 72. Crevice corrosion morphology of a nickel alloy 625 specimen corroded at 200 mV vs SCE and 10 ft-lb torque for a 72-hour period.

It is presumed that a critical pH [103] and metal cation concentration must be reached within the crevice (near the crevice tip) for etching dissolution to occur. At some point, the metal cation concentration within the crevice builds up to a critical value, at which point precipitation of a metal salt occurs, and a brightened surface is seen [104].

3.4. Crevice Corrosion Product Analysis

3.4.1. Crevice corrosion products analysis over time

The composition of the crevice corrosion products was studied using EDS and ICP analyses. During the anodic polarization test at 200 mV vs SCE, between 12 and 18 hours of exposure, light green crevice corrosion products started to form around the crevice mouth of the RCAs as shown in Figure 73(a). At longer exposure times, even more crevice corrosion products accumulated around the crevice mouth, and a yellowish/brown coloration near the crevice mouth started to appear, as shown in Figure 73(b). When the RCA was removed from the solution, the light green crevice corrosion products immediately fell off, but the yellow/brown corrosion products remained around the crevice mouth, see Figure 73(c). It was not possible to collect an image of the RCA at two weeks of exposure without removing the RCA from the solution, as the bulk solution at this exposure time was very cloudy.

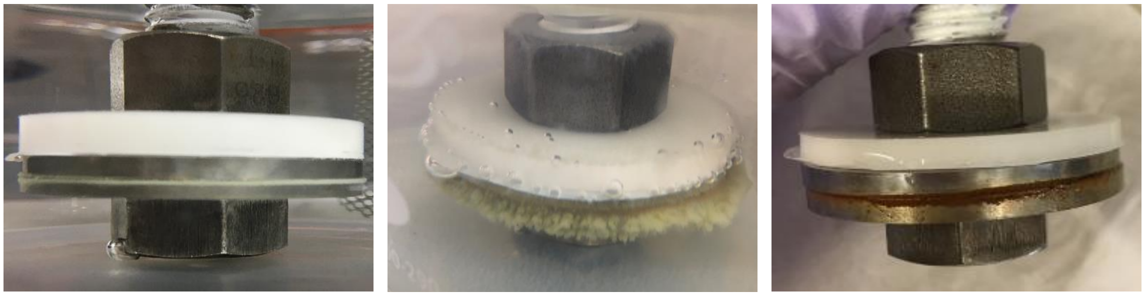

(a) 17 hours

(b) 47 hours

(c) 2 weeks
(removed from solution)

Figure 73. Evolution of crevice corrosion products outside of the crevice mouth of the RCAs at applied potential of 200 mV vs SCE.

Once the anodic polarization test is finished, based on the predetermined time of the test, the RCA was opened for collection of the corrosion products formed on the corroded surfaces of the specimens inside the crevice. At early times, i.e. 24 hours, a light green solution was observed over and around the corroded area inside the crevice, as seen in Figure 74(a). As the immersion time increased, i.e. 48 hours, dark green and some brown crevice corrosion products start to accumulate around the corroded area, and evidence of diffusion of crevice corrosion products was observed around the edges of the washer, as shown in Figure 74(b). At longer immersion times, e.g. 5 days (120 hours), the crevice corrosion products are mostly black/dark brown, and are accumulated around the corroded area (see Figure 74(c)). A light brown/yellowish coloration is seen on the non-attacked area, suggesting the diffusion of some crevice corrosion products out of the crevice.

Following these observations, corrosion products were collected from RCAs corroded for 18 hours, 30 hours, 60 hours, and 2 weeks. These corrosion product specimens were collected from both inside of the crevice (within the corroded region) and outside the crevice (around the crevice mouth).

(a) 24 hours (b) 48 hours (c) 5 days

Figure 74. Evolution of crevice corrosion products formed inside of the crevice on the corroded surface of the specimens of the RCAs at applied potential of 200 mV vs SCE.

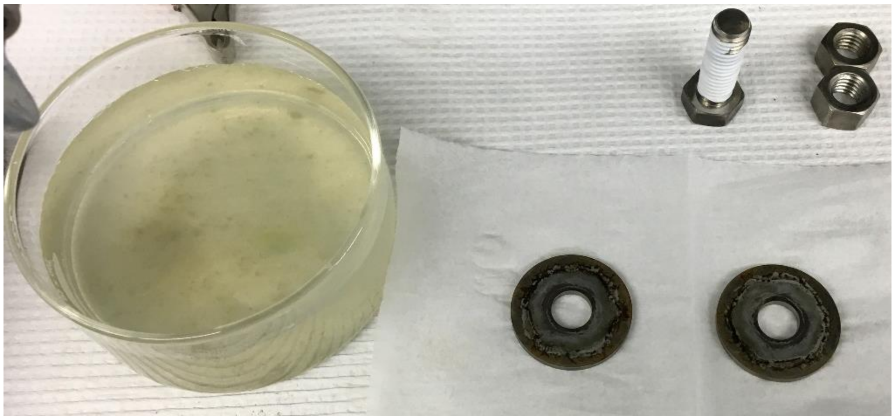

Figure 75. Appearance of the bulk solution after a 78-hour immersion of a RCA anodically polarized at 200 mV vs SCE.

During the anodic potentiostatic polarization, the coloration of the bulk solution changed over time. The clear ASTM ocean water became yellow and cloudy after 24 hours. At longer immersion times, the solution acquired a green color, as shown in Figure 75. The change in coloration of the bulk solution suggests the dissolution of some crevice corrosion products into the bulk solution.

The crevice corrosion products found inside and outside of the RCAs were analyzed using EDS and ICP analyses to study their elemental composition. The procedure for the analysis of crevice corrosion products found inside and outside the crevice is summarized in Figure 76.

The crevice corrosion products found within the crevice were studied in the following manner: (*i*) Crevice corrosion products formed on one of the crevice washers were allowed to dry for subsequent EDS analysis on the specimen, and (*ii*) the crevice corrosion products on the other crevice washer were rinsed with DI water to collect all the corrosion products in solution for subsequent ICP analysis. This collected solution was divided in two to perform two different ICP analyses. A 5% v/v HCl solution was added to the first solution-specimen to ensure that all the corrosion products (as there were some solids) were dissolved in solution. ICP analysis was then performed. The second solution-specimen was first filtered with an 8 μm pore size filter paper to separate the soluble and insoluble corrosion products in solution. The solution collected after filtration was then dissolved into a 5% v/v HCl solution for subsequent ICP analysis. The remaining solids were studied using EDS.

The light/green crevice corrosion products formed around (outside) the RCA were also analyzed using EDS and ICP techniques. These crevice corrosion products were collected with a syringe, and split into two different specimens for these two analyses. The first specimen was dissolved in 5% v/v HCl for subsequent ICP analysis; the second specimen was first filtered with an 8μm pore size filter paper to separate the soluble and insoluble corrosion products, then the solution collected was dissolved in 5% v/v for ICP analysis. The remaining solids were studied using EDS technique.

Bulk solution specimens at the four times under study (18 hours, 30 hours, 60 hours, and 2 weeks) were also collected. Bulk solution specimens were collected with a syringe, and then dissolved in a 5% v/v HCl solution for subsequent ICP analysis.

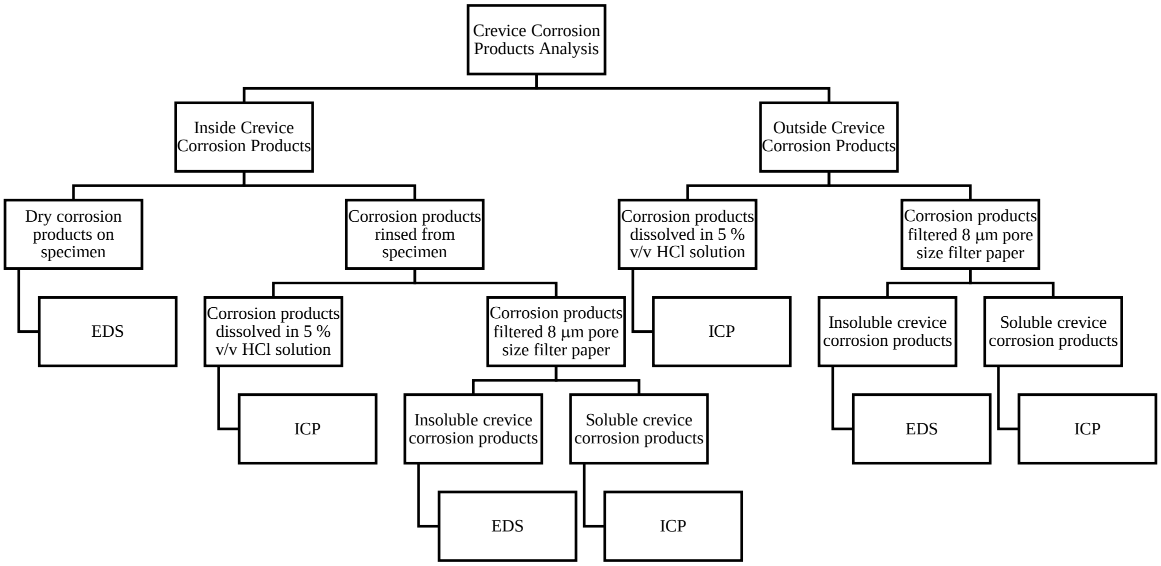

Figure 76.Flow chart for EDS and ICP of crevice corrosion products found inside and outside the RCAs.

3.4.2. EDS Analysis Results

3.4.2.1. EDS analysis of crevice corrosion products found inside of the crevice

A portion of the crevice corrosion products found inside of the crevice were collected and allowed to dry for subsequent EDS analysis. Powder-like solids were collected for all times under study: 18 hours, 30 hours, 60 hours, and 2 weeks of exposure. Figure 77(b) shows the results obtained from EDS in relative wt%. At early times, O, Ni, and Mo content are the most prevalent species in the corrosion products inside the crevice, and as the exposure time increases, Nb content increases. The relative wt% without oxygen content is also shown in Figure 77(a).

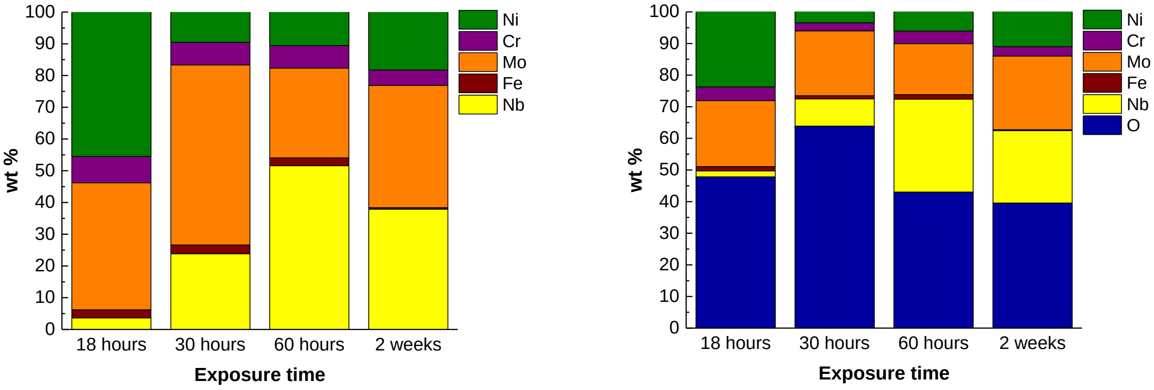

(a) (b)

Figure 77. Quantitative EDS analysis results of crevice corrosion products found inside of the crevice before filtering at different exposure times.(a) Without oxygen content and (b) with oxygen content.

3.4.2.2. <u>EDS Analysis of Crevice Corrosion Products after Filtration</u>

A portion of the crevice corrosion products found inside and outside the crevice were collected and filtered using DI water. The remining (insoluble) crevice corrosion products were studied under EDS. Solids were collected at 30 hours, 60 hours, and 2 weeks of exposure. No solid crevice corrosion products were found at 18 hours of exposure. Figures 75 and 79 summarize the EDS analyses of the crevice corrosion products inside and outside of the crevice, respectively.

The insoluble crevice corrosion products inside the crevice, shown in Figure 78(b), were found to be rich in O, Mo, and Nb. The insoluble crevice corrosion products outside the crevice, shown in Figure 79(b), were found to be rich in O, Cr, and Ni. At 2 weeks of exposure, the crevice corrosion products outside the crevice increased in Nb and Mo content, suggesting that Mo and Nb elements take a longer to diffuse out of the crevice than the other elements.

As a general observation based on Figures 78 and 79, it can be seen that within the crevice, the crevice corrosion products are depleted in Ni and Cr, while Mo and Nb are enriched as the specimen corrodes. On the other hand, the crevice corrosion products found outside are initially depleted in Mo and Nb, and eventually become enriched in these elements.

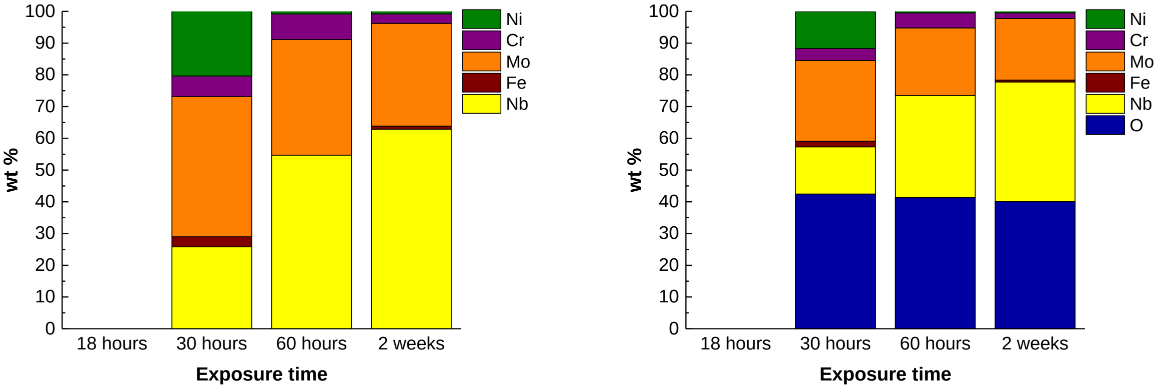

(a) (b)

Figure 78. Quantitative EDS analysis results of crevice corrosion products found inside of the crevice after filtering at different exposure times. (a) Without oxygen content and (b) with oxygen content.

.

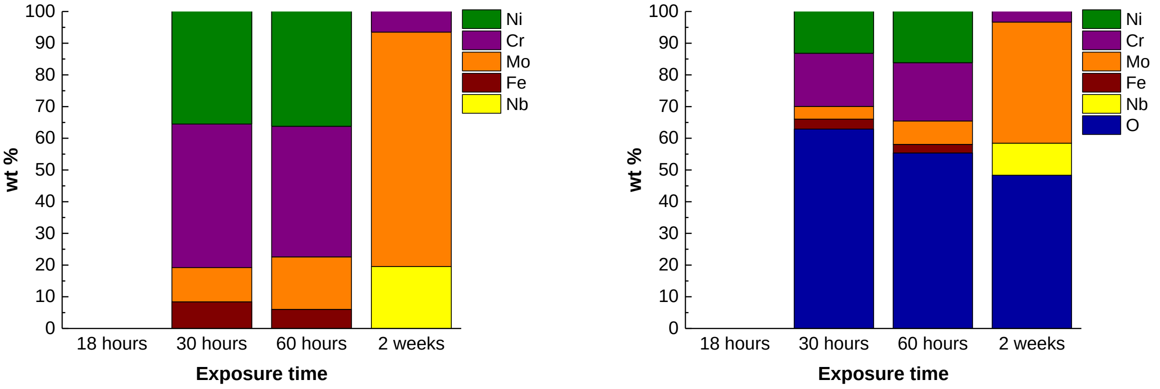

(a) (b)

Figure 79. Quantitative EDS analysis results of crevice corrosion products found outside of the crevice after filtering at different exposure times. (a) Without oxygen content and (b) with oxygen content.

3.4.3. ICP Analysis Results

Crevice corrosion products found inside and outside the crevice were also analyzed using ICP analysis. The ICP analysis results for the crevice corrosion products found inside the crevice are shown in Figure 80. These crevice corrosion products were found to be reach in Ni, Cr, and Mo content. Relatively small amounts of Fe and Nb were found. These results agree with the EDS results presented in Figure 77; however, a relatively higher amount of Nb was detected in the EDS analysis. One of the reasons why a smaller amount of Nb appeared in the ICP analysis is because a relatively acidic solution is needed to dissolve all the Nb cations in solution. Since only a 5 %v/v HCl solution was used, it is likely that not all of the Nb present in the corrosion products was dissolved. This smaller amount of Nb in solution was due to an experimental limitation.

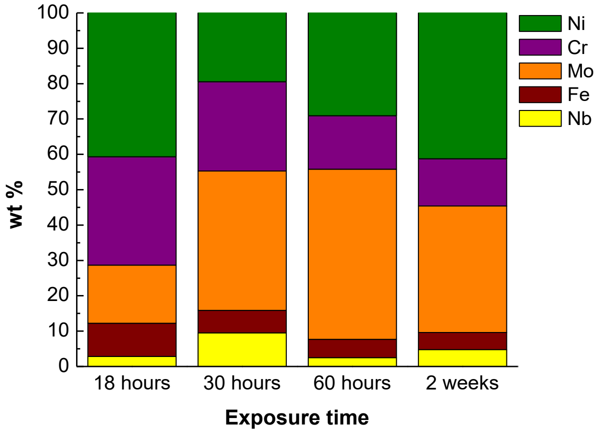

Figure 80. ICP analysis results of crevice corrosion products found inside of the crevice at different exposure times.

Figure 81 shows the ICP results obtained for the crevice corrosion products found outside the crevice. These results are in agreement with the EDS results presented in Figure 79. At early times, the crevice corrosion products found outside the crevice were rich in Ni, Cr, Fe, and Mo. The ICP results at 2 weeks do not show an increase of Nb content. Again, this can be explained in that the solution used to dissolve the crevice corrosion products was not acidic enough to dissolve Nb in solution, so it could not be detected through ICP analysis.

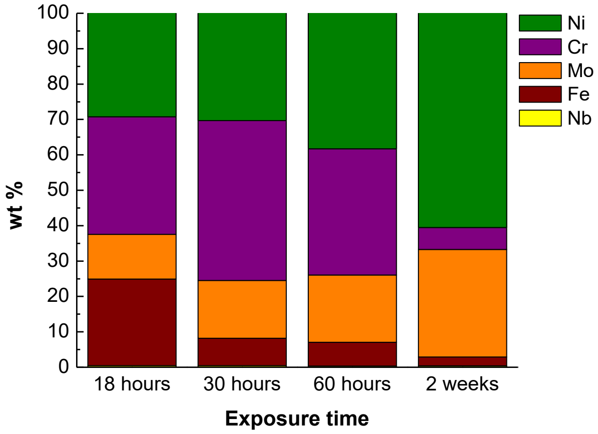

Figure 81. ICP analysis results of crevice corrosion products found outside of the crevice at different exposure times.

ICP Analysis Results of the Bulk Solution

The bulk solution composition was also analyzed; ICP results are shown in Figure 82. It was found that at 18 hours, the bulk solution was rich in Ni, Cr, and Fe, with some Mo content. As the exposure time increased, so did Ni content, becoming the most predominant species in solution at 30 and 60 hours. By 2 weeks of exposure, the bulk solution becomes richer in Cr, Fe, and Mo content. These results suggest that at some point the diffusion of Ni becomes slower, and some other elements, such as Cr and Mo, have a higher chance to diffuse out and dissolve in solution. Only small traces of Nb were detected in solution, suggesting that Nb does not dissolve in the bulk solution.

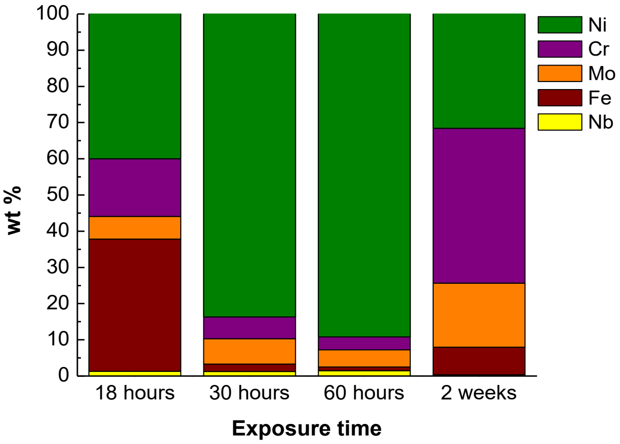

Figure 82. ICP analysis results of the bulk solution at different exposure times.

3.5. Modified T.H.E. Method for Determining the Repassivation Potential

The modified T.H.E. method experiment was performed using a traditional RCA at different exposure times, ranging from 12 to 72 hours in order to determine crevice corrosion repassivation potentials. Once crevice corrosion had propagated for a predetermined period, the potential was stepped down 10 mV every 2 hours. The current vs time responses of the modified T.H.E. experiments are shown in Figures 83-87. In Figure 83 a polarization response for a total of 72 h at a constant potential of 200 mV vs SCE is overlaid as a reference. It can be noticed in this figure, that by 180 mV vs SCE, the total current of the modified T.H.E. experiment starts to deviate from the *I vs t* response obtained at a constant potential of 200 mV vs SCE.

3.5.1. Current vs time Response

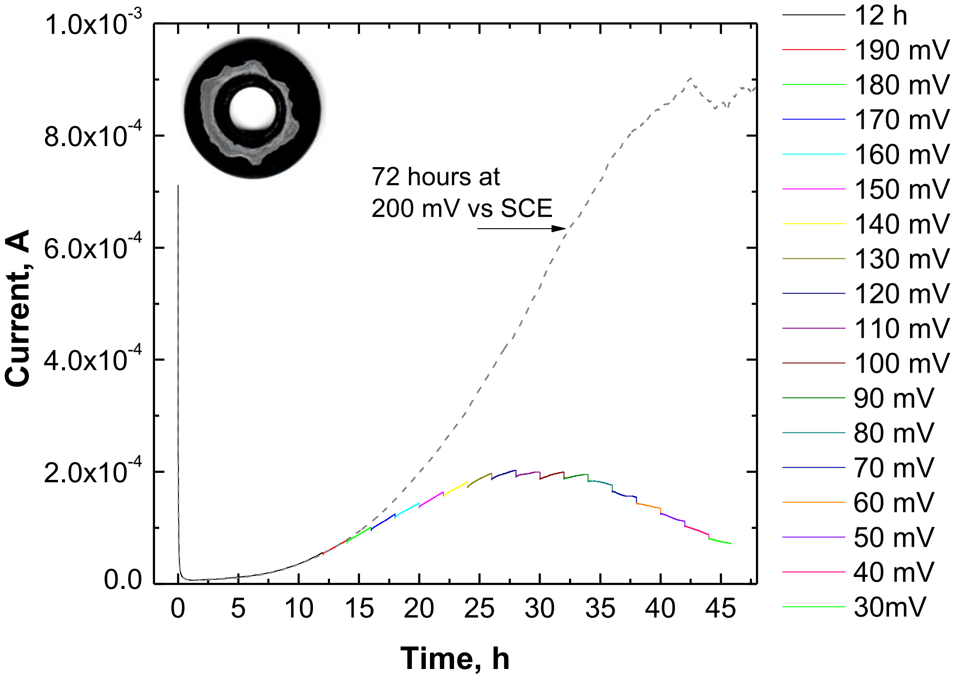

Figure 83. Modified THE method for 12 hours

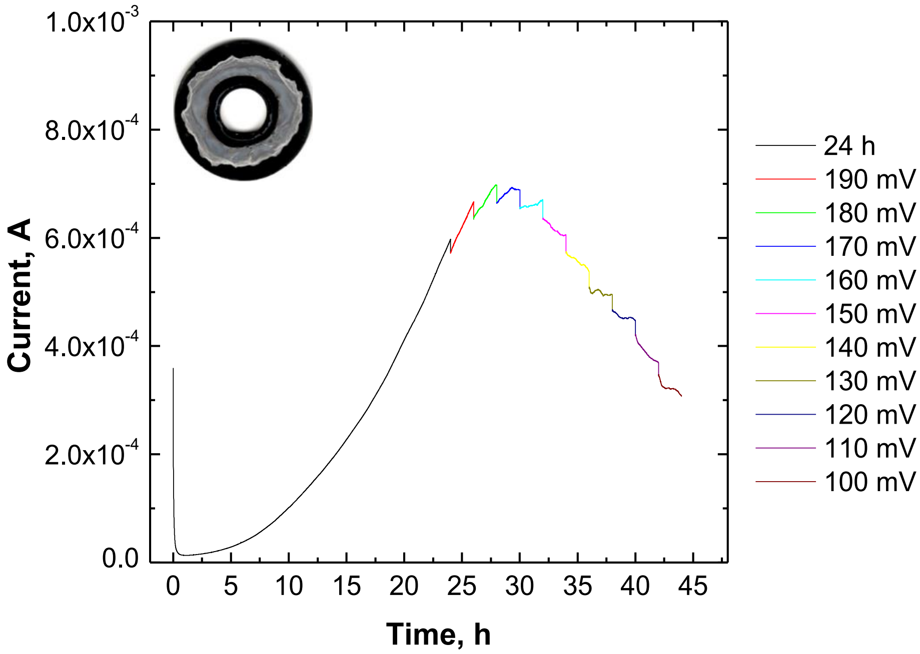

Figure 84. Modified THE method for 24 hours

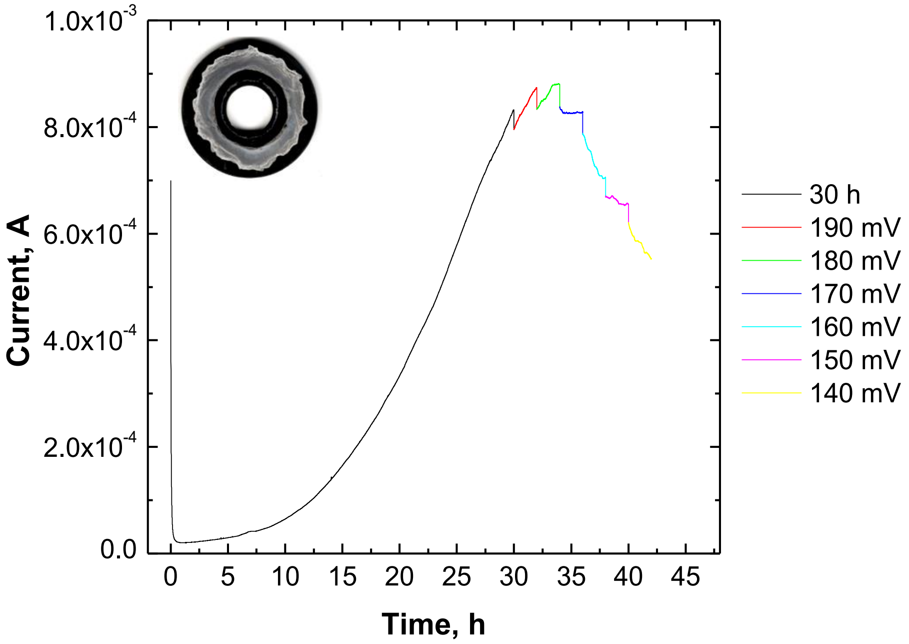

Figure 85. Modified THE method for 30 hours.

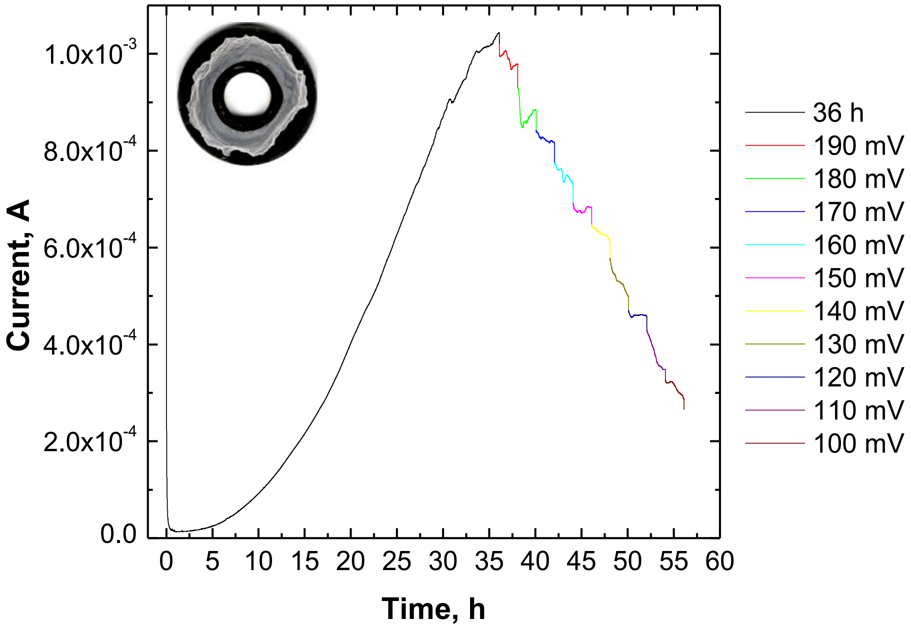

Figure 86. Modified THE method for 36 hours.

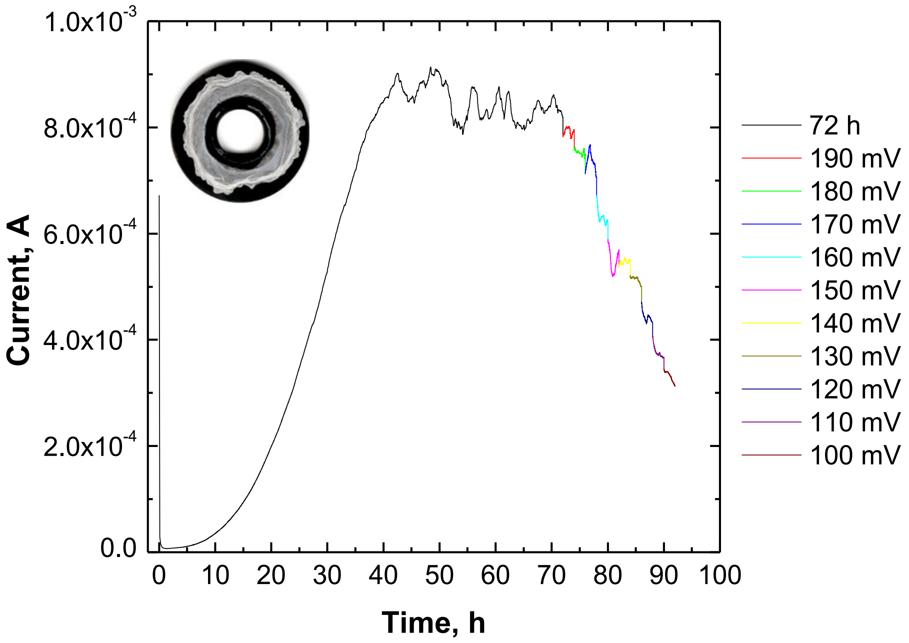

Figure 87. Modified THE method for 72 hours.

Dependent on the exposure time under study, two different *I vs t* responses were found: (1) the current response continued to increase (at a lower rate) over time as the applied potential decreased, and (2) the current response decreased and repassivation occurred after the potential decreased. The first case was observed for the exposure times of 12, 24, and 30 hours; the second case was observed for the exposure times of 36 and 72 hours.

Table 17 summarizes the critical parameters from the T.H.E. experiment: propagation time prior to stepping down the potential, total time of stepping down, total time of exposure, crevice repassivation potential ($E_{rp,crev}$), maximum current reached for each modified T.H.E experiment, movement of the active front (x_{crit}), and penetration depth (*d*).

It was found that at early times, when the active front is far from the crevice mouth, the repassivation potential reached low values. For example, the $E_{rp,crev}$ for 12 hours of propagation time (prior to step-down) was found to be 80 mV vs SCE. At later times, where the extent of crevice corrosion damage was greater and went deeper into the specimen face, and the location of x_{crit} reached its maximum proximity to the crevice mouth, the repassivation potential reached higher values. For example, the $E_{rp,crev}$ for 72 hours of propagation time was 190 mV vs SCE. These results suggest that $E_{rp,crev}$ was found to be dependent on the location of x_{crit}, and the amount of damage prior to initiating the step-down phase of the T.H.E experiment.

Table 17. Critical parameters obtained from the T.H.E. experiment.

Exposure time prior to step-down phase (h)	**Time during step-down phase (h)**	**Total time of exposure (h)**	**$E_{rp,crev}$ (V vs SCE)**	**Max. Current (A)**	**x_{crit} μm**	**d μm**
12	34	46	80	1.96×10^{-4}	4915	-3.44
24	20	44	150	6.85×10^{-4}	3812	-10.40
30	10	40	170	8.81×10^{-4}	3322	-8.18
36	20	56	190	1.02×10^{-3}	2922	-15.17
72	20	92	190	9.01×10^{-4}	2855	-32.85

The crevice corrosion damage profiles obtained at different exposure times during the modified T.H.E. method are shown in Figure 85.

12 hours

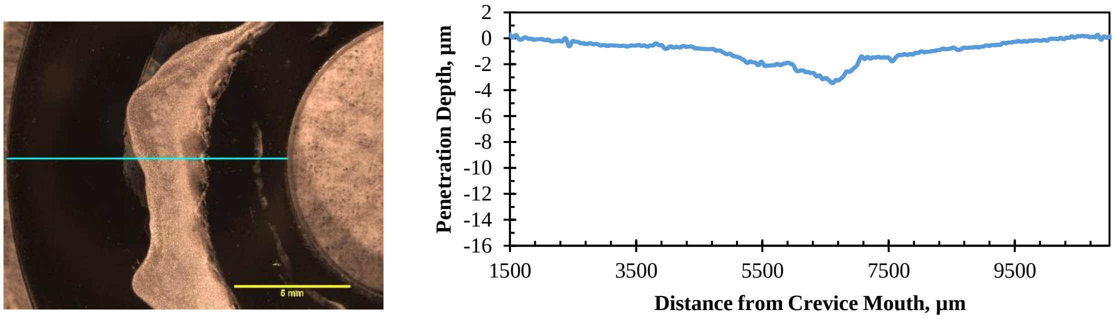

24 hours

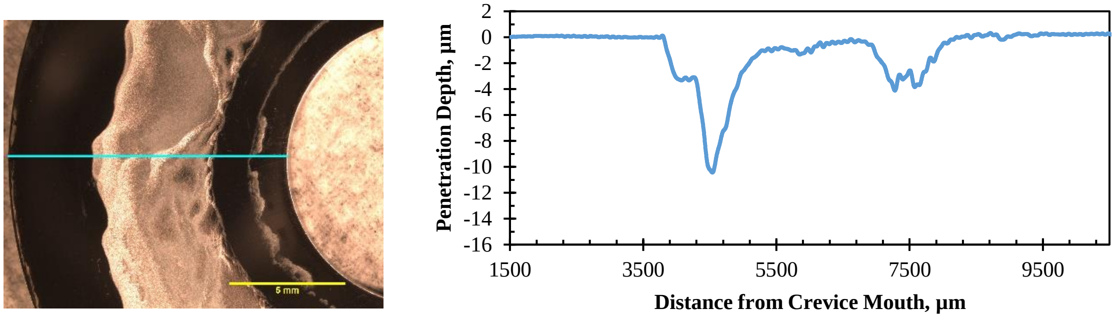

30 hours

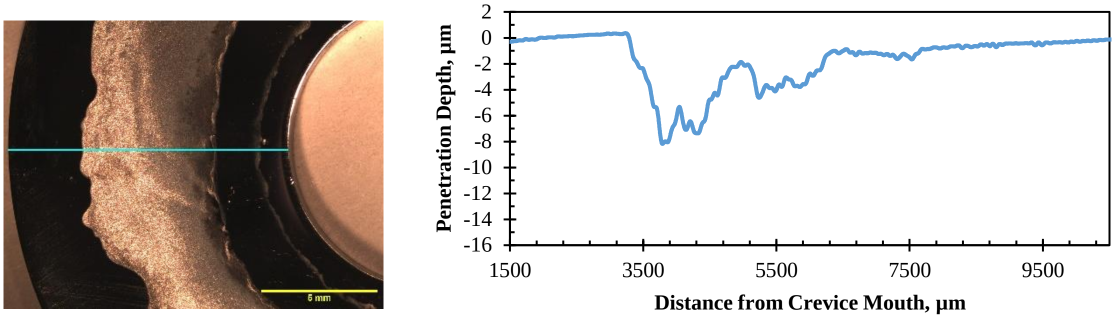

36 hours

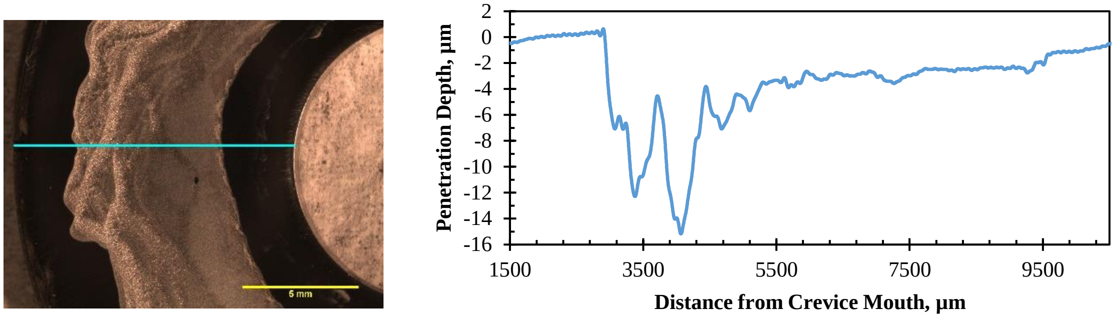

72 hours

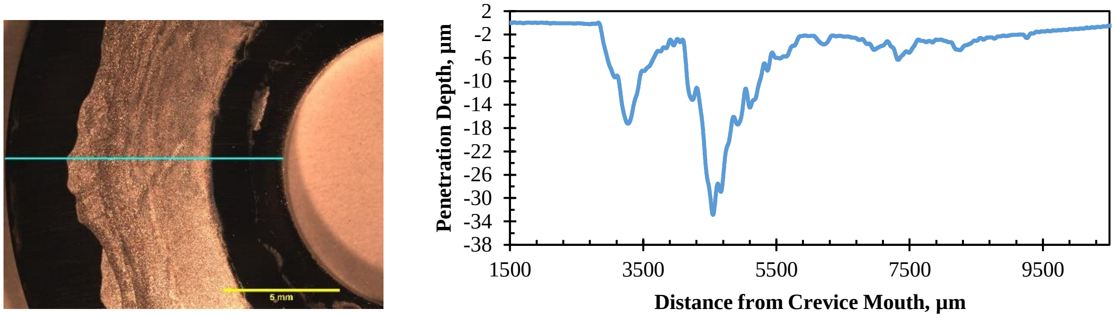

Figure 88. Optical micrographs of crevice face and the corresponding crevice corrosion damage profiles of specimens using the T.H.E method at different exposure times. Applied torque: 10 ft-lb.

3.6. X-ray Computed Tomography for Measuring the Crevice Gap

X-ray computed tomography was performed on two different specimens: one using metal/metal washers and one using metal/non-metal washers. These specimens were polarized at 200 mV vs SCE for a period of 2 weeks. The radiography image and the measurement of the crevice gap of the metal/metal washer is shown in Figure 89. From this figure, it can be noticed that the crevice gap is not completely uniform along the crevice length. The values of crevice gap varied between 20 μm near the crevice tip, to 50 μm near the crevice mouth.

Figure 90 shows the different planes at which the specimen can be analyzed, and the respective reconstructed solid. An attempt to measure the crevice gap given by the metal/acrylic washer was also performed. However, due to the significant difference between the light density of the acrylic material and the high density of the metal washer, the only material that could be observed was the metallic specimen – the acrylic washer was invisible to XCT, see Figure 91. These results also showed a higher resolution image, suggesting that a thinner specimen gives a sharper image.

Figure 89. Crevice gap of metal/metal washer. X-ray image.

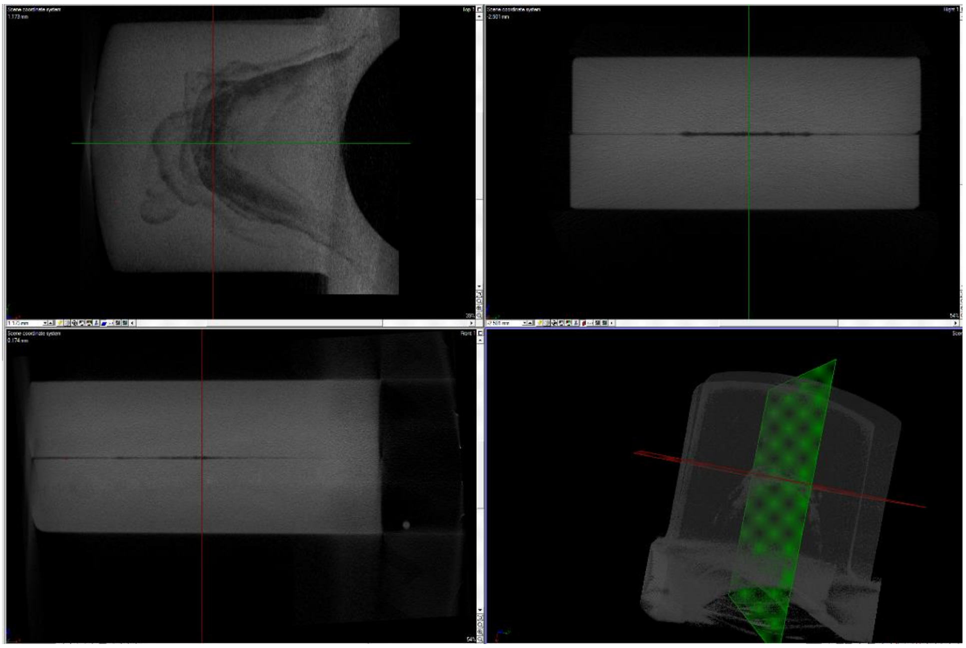

Figure 90. Metal to metal washer, reconstructed solid.

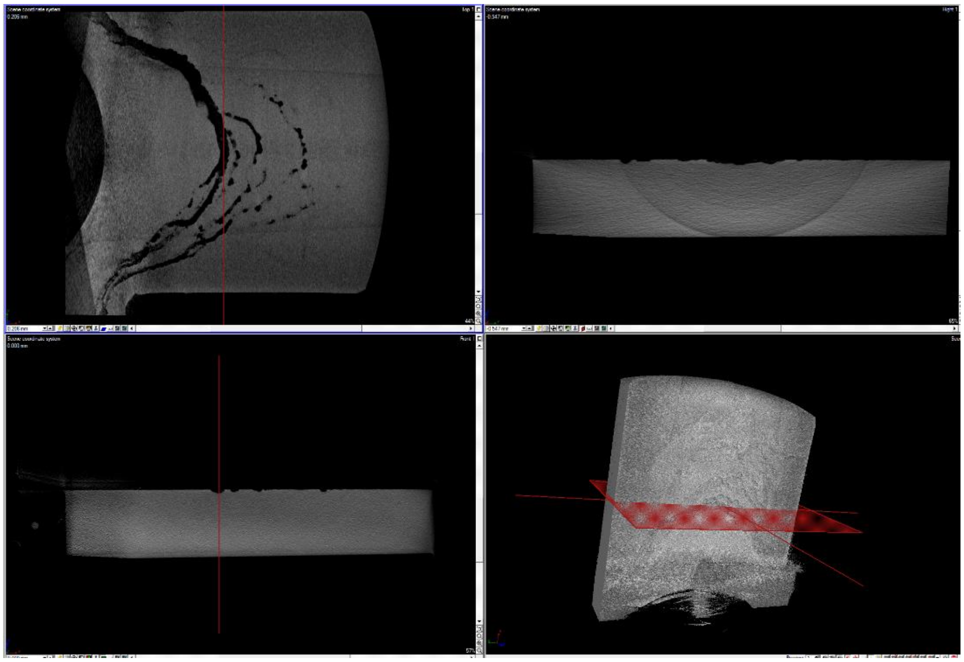

Figure 91. Metal to clear washer, reconstructed solid.

IV. DISCUSSION

4.1. Factors Influencing the Manifestation of an Active to Passive Transition

Here an attempt is presented to address the mechanism by which Mo and Nb salts in solution are responsible for an active to passive transition in alloy 625. One possibility is that these metal salts decrease solution pH, however, calculating pH for these solutions is not straightforward. Previous researchers have used a variety of empirical and theoretical methods to calculate the pH of simple HCl-based solutions as well concentrated metal salt solutions. These equations were summarized in the Background Section in equations 8-13.

In comparison to these methods, the OLI software provides a calculation of pH based on Equation 17 and avoids empirical correlations. The predicted pH values for the NiCrFeMoNb, NiCrFeMo and equivalent chloride (NiCrFe) solutions from the OLI software are shown in Figure 51 as a function of solution concentration. At a given concentration, for example 4.0 m, it can be seen that the NiCrFe solution has a pH of ~ +0.4. Adding Mo, to the solution (4.0 m NiCrFeMo) decreases the pH to ~ -0.4. By adding Nb (4.0 m NiCrFeMoNb), the pH decreases to ~ -0.6. Therefore, the cation speciation directly affects crevice pH. The HCl base solutions, the OLI calculated pH as a function of concentration is also presented in Figure 31.

Oldfield and Sutton defined the CCS as a combination of Cl^- and pH required to raise the anodic current density to 10 µA/cm^2, and they used a semi-empirical relationship, shown in Equation 9, for defining the pH of the solution. As it relates to this study, in Figure 92 the peak current densities as a function of the calculated pH were compared using two different methods for the NiCrFeMo solution: the Oldfield-Sutton relationship in Equation 9 and OLI. As seen in Figure 92, a peak current density of 10 µA/cm^2

is attained for the lowest concentration of salts that was analyzed, i.e. 3.0 m. In addition, for a fixed concentration, the pH values calculated using the Oldfield and Sutton method grossly underestimate the OLI-calculated values. It can be seen that the slopes of the i_{crit} vs pH curves are divergent with the Oldfield-Sutton slope, which has values far more positive than that from the OLI calculation. This difference in the methods is exacerbated when considering cations, such as Nb, that are not accounted for in empirical Oldfield-Sutton equation, such as Nb, as is shown in Figure 92. This further demonstrates the need for a single method for comparing solutions.

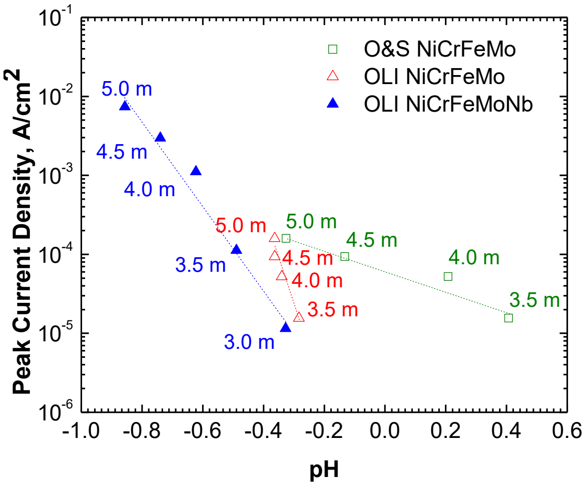

Figure 92. Different metal concentration solutions and their respective pH and peak current density. pH is calculated with OLI software and the Oldfield & Sutton (O&S) equations for pH.

Table 18. Comparison of results of different model crevice electrolytes. Concentration of metal chlorides are given in molality (m).

Crevice Electrolyte	Total (m)	$CrCl_3$	$NiCl_2$	$FeCl_2$	$MoCl_3$	$NbCl_5$	Peak Current (A/cm^2)	pH$_{OLI}$
NiCrFeMoNb	5.0	1.247	3.105	0.253	0.281	0.114	7.4×10^{-3}	-0.87
NiCrFeMo	5.0	1.247	3.105	0.253	0.281	-	1.6×10^{-4}	-0.36
McCafferty[11]	4.7	0.364	3.796	0.212	0.370	-	1.2×10^{-4}	-0.37

Table 18 compares the results obtained by McCafferty and the results obtained in this study for NiCrFeMo and NiCrFeMoNb. The pH values reported in this table for each solution were calculated using the OLI software. McCafferty's solution is comparable to the NiCrFeMo from this study, with similar total molal concentrations and pH values, but has less $CrCl_3$ content than the NiCrFeMo solution. Nevertheless, these solutions have similar peak current density values on the order of 10^{-4} A/cm^2 for equivalent pH. It appears that pH of metal chloride solutions as calculated by OLI is a good predictor of peak current density. However, for the metal salt solution solutions, pH not only represents the concentration of H^+ (as is the case in diluted solutions), but rather is a representation of activity which is controlled by the concentration of all species in solution.

In addition to pH, OLI generates speciation data and predicts both aqueous and solid species in solution. While all the speciation data have been analyzed for the metal salt solutions used in this study, only the concentration of three aqueous species will be discussed here: H_3O^+, free Cl^- and free Mo^{3+} content. The concentration of H_3O^+, and free Cl^- in the NiCrFeMo and NiCrFeMoNb solutions were greater over all solution concentration as compared to the NiCrFe equivalent chloride solution (Figures 57 and 59). However, no correlation was found between these species and the appearance of the active to passive transition in the polarization curves. In addition to H_3O^+ concentration, the activity coefficient γ^{H3O+} also contributes to pH ($pH = -\log(m_{H^+}\, \gamma_{H^+})$). As such, γ^{H3O+} for these solutions was also tabulated. As seen in Figure 58, an increase in γ^{H3O+} for the NiCrFeMoNb solution is predicted at a concentration of approximately 3.0 m dissolved alloy. More interestingly, in this concentration region an increase in Mo^{3+} is also predicted by the OLI software (Figure 60). This concentration coincides with the manifestation of the active to passive transition. Below 3.0 m, the vast majority of the $MoCl_3$ added to solution precipitates as MoO_2. This raises the possibility that Mo^{3+} concentration may be responsible for the active to passive transition in the anodic polarization curve for alloy 625 in these solutions. For comparison, in the NiCrFeMoNb metal salt solution, the Mo^{3+} concentration was almost four times higher than the 3.0 m NiCrFeMo solution, i.e. 0.090 m vs 0.023 m. Therefore, if Mo^{3+} concentration is responsible for the manifestation of the active to passive transition in alloy 625, one would predict that no active to passive transition would occur in a NiCrFeMoNb solution for Mo^{3+} concentration equal to 0.023m. To test this hypothesis OLI was used to calculate the molality of a NiCrFeMoNb solution where the Mo^{3+} concentration was equal to 0.023 m. The molality of solution was found to be 2.4 m

NiCrFeMoNb and the corresponding potentiodynamic polarization curve for alloy 625 in this solution is presented in Figure 93. As seen in this figure, the OCP of the NiCrFeMoNb solution is much higher as compared to 3.0 m and similar to the NiCrFeMo solution, consistent with passivation. More importantly, no active to passive transition was observed for the 2.4 m NiCrFeMoNb solution.

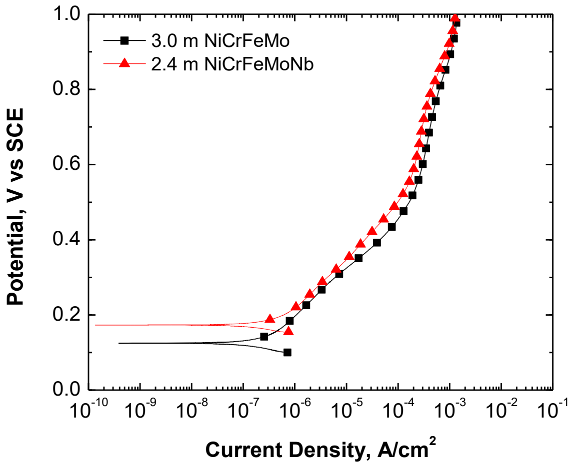

Figure 93. Comparison between a 3.0 m NiCrFeMo ([Mo^{3+}]=0.023m) and a 2.4 NiCrFeMoNb ([Mo^{3+}=0.023m]) metal salt solutions.

From this finding, it can be concluded that the composition of the CCS for alloy 625 is in the range of 2.4-3.0 m NiCrFeMoNb solution, and that Mo^{3+} concentration plays a key factor in the manifestation of an active to passive transition in the CCS. Specifically, niobium in solution lowers the solution pH (e.g. increases [H_3O^+] and γ^{H3O+}, Equation 18), which results in a higher concentration of Mo^{3+} in solution for the equivalent concentration of dissolved alloy. This is consistent with moving from the MoO_2 region in the Pourbaix diagram to the region of Mo^{3+} stability although in that case, pH is defined simply as [H_3O^+].

At this point it could be proposed that an alloy's susceptibility to crevice corrosion is directly proportional to the pH of the critical crevice solution that develops. That is, if an alloy contains an element (metal cation) that produces a more aggressive solution than a comparable alloy that does not contain that element, it will be more susceptible to crevice corrosion. To test this theory, OLI was used to calculate pH values of metal salt solutions for nickel alloys G3, C-276, and C-22. The chemical composition for these alloys is shown in Table 19.

Table 19. Weight Percent (wt%) composition of different nickel alloys.

Element / **Alloy**	**Ni**	**Cr**	**Fe**	**Mo**	**Nb**	**W**	**Co**
G-3	51	22	20	7	-	-	2
625	61	21	5	9	4	-	-
C-22	58	22	4	13	-	3	-
C-276	58	16	6	16	-	4	-

Although each of these alloys has Ni, Cr, and Mo in their composition, alloys C-22 and C-276 have W in their chemical composition as well, and Alloy G3 has Co as part of its chemistry. While the thermodynamic data needed to solve Equation 18 is readily available for Ni, Cr, Fe, and Mo, the same is not true for W, Co, and Nb (found in alloy 625) as discussed above. For Nb, Nb(V) is likely the stable species within the crevice environments. Lower oxidation states of Nb, such as Nb(IV) and Nb(III) exist as well, but are only stable at potentials that are much lower than the stability domain of water; they would not be a realistic approximation of dissolution products. As such, they were not considered. In the absence of data for $NbCl_5$, a ‘pseudo niobium (V) chloride’ was used by combining Nb_2O_5 and HCl as described by Equation 15. For W, a similar approach to that of Nb_2O_5 was used. WCl_4 is known to exist, and it is likely to be a corrosion product because it contains W at the lowest oxidation state; however, there is not enough data in the literature to model WCl_4. Thus, the dissolution of WCl_4 was treated as the combination of [WO_2 + 4HCl] for the OLI simulation. In the case of alloy G3, $CoCl_2$ is the likely corrosion species, and, similarly to Nb and W, this addition was treated as [CoO + 2HCl].

As shown in Figure 94, the calculated pH values of 625, C-276, C-22, and G3 decrease as the molality of the solution increases. Using the pH of the 4.0 m solution as a reference and the general trend that crevice corrosion resistance increases in the order G3<625<C22<C276 [22], [29], there does not appear to be a correlation between crevice corrosion susceptibility and critical crevice solution pH. On the contrary, from the trend in pH in Figure 94, one might predict that G3 would be the most resistant to crevice corrosion. That is, pH at this concentration decreased in the order G3>C22>C276>625.

In addition to these observations, in Figure 94 it can be noticed that for concentrations ≤ 4.0 m the trend in pH is similar for all alloys, indicating that Ni, Cr, and Mo are dominating the pH calculation. Moreover, for alloys containing W or Nb, a sharp decrease in pH was observed at molalities > 4.0 m, as compared to G-3, which contains Co. To explore whether or not this was an effect of W and Nb, or the result of the additional HCl needed to create the 'pseudo metal chlorides' (WO_2 and Nb_2O_5 required 4 and 5 moles of HCl respectively, as compared to only 2 moles of HCl for CoO), the solutions of alloy C-22, C-276, and 625 were simulated with 2 moles of HCl (rather than 4 and 5). However, this resulted in trends in pH that were very similar as those observed in Figure 94. Thus, it appears that the calculated decrease in pH cannot be attributed solely to the HCl added for the simulation.

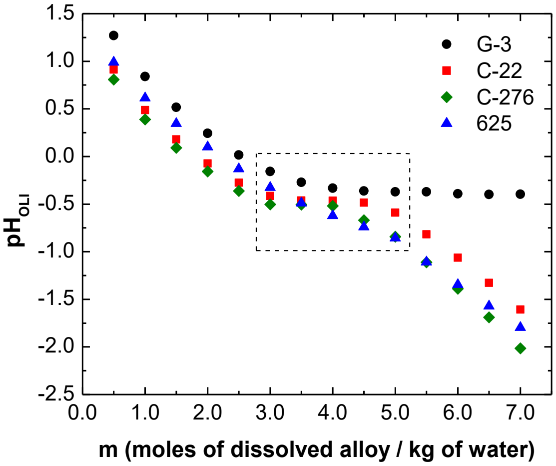

Figure 94. Comparison of OLI-predicted pH values for nickel alloys G-3, C-22, C-276 and 625 as a function concentration assuming stoichiometric dissolution.

4.1.1. Correlations Between HCl and Base and Metal Salt Solutions

Figure 95 compares i_{crit} values from the polarization curves of alloy 625 in HCl-based solutions against those for alloy 625 in NiCrFeMoNb solutions as a function of OLI- pH (0.1 m to 5.6 m). As can be seen in this figure, the trend between peak current density is different for pH greater than -0.7 as compared to pH less than -0.7. This appears to be a real observation and not an effect of the calculation as the relationship between pH and HCl concentration does not deviate over this concentration range (Figure

51, HCl). We are unsure why the peak current density deviates at pH -0.7 however, this holds true when we analyze the data from other investigators and for other alloys (Figure 96). It may be that below some threshold HCl concentration, the relatively small increase in current density just above the open circuit potential is not a true active to passive transition. This was certainly the case for alloy C 276 in the data from Lillard and Scully [22].

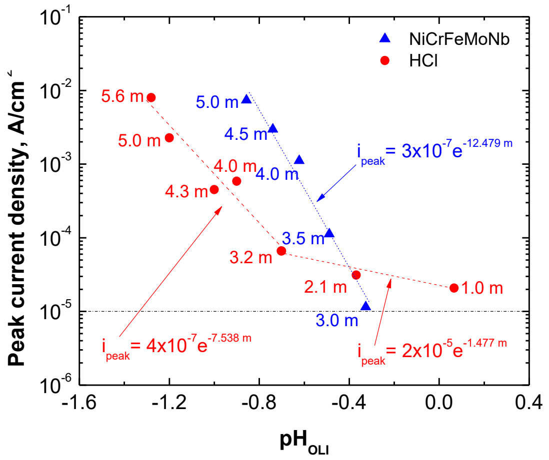

Figure 95. Comparison of peak current densities between HCl and Stoichiometric Solutions for nickel alloy 625. pH values were calculated using OLI software.

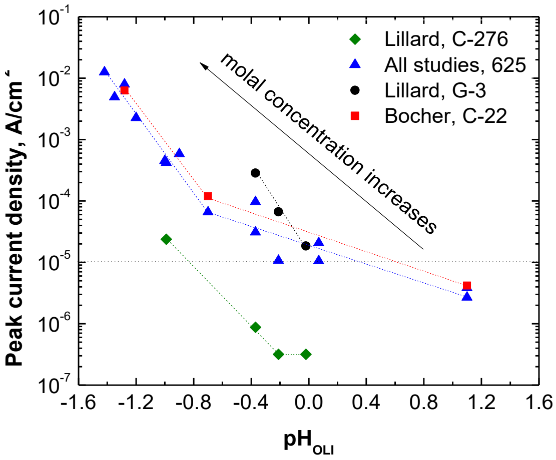

Figure 96. Comparison of peak current densities of different nickel alloys in HCl-based solutions. pH was calculated using OLI software.

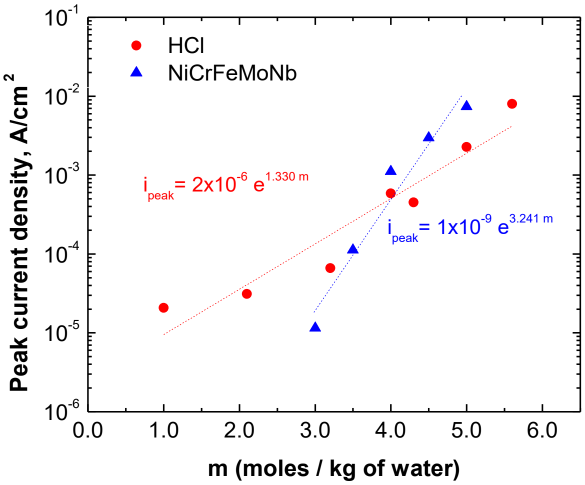

Figure 97. Comparison of peak current densities for nickel alloy 625 in HCl and the NiCrFeMoNb metal salt solution as a function of solution concentration.

Given the difficulty of accurately measuring pH, preparing solutions of determined HCl concentration may be a more useful method for obtaining peak current densities. This concept is demonstrated in Figure 97. As seen in this figure, the relationship between peak current density and HCl molality can be fitted to a single exponential relationship over the entire concentration range. For comparison, the data for the NiCrFeMoNb solution is again presented in Figure 97.

Although it is ideal to determine the polarization response of alloy 625 in solutions containing metal cations, this can be time consuming, costly, and not practical. Given that the polarization curves are similar for NiCrFeMoNb and HCl-based solutions with pH<-0.7 (Figure 95), a relationship for predicting NiCrFeMoNb peak current densities using HCl-based solutions may be useful. For the NiCrFeMoNb metal salt solutions, the relationship between peak current density and solution concentration is shown in Figure 19 and given by:

$$i_{salt} = 1 \times 10^{-9}\, e^{3.2 \cdot m_{salt}} \qquad \text{Equation 22}$$

where i_{salt} is the peak current density, and m is the total metal salt concentration in molal, assuming stoichiometric dissolution.

For the HCl base solutions:

$$i_{HCl} = 3 \times 10^{-6}\, e^{1.3 \cdot m_{HCl}} \qquad \text{Equation 23}$$

where i_{HCl} is the peak current density, and m is the HCl concentration in molal. Equating the HCl and metal salts relationships, $i_{salt} = i_{HCl}$, the following relationship is obtained:

$$m_{salt} = 0.41\, m_{HCl} + 2.5 \qquad \text{Equation 24}$$

Therefore, if one chose to use HCl-based solutions to simulate the response of alloy 625 in a crevice, Equation 24 relates the peak current density at a given HCl concentration to the equivalent stoichiometric metal salt concentration (both in molal).

4.2. Precipitation of Metal Oxides within the Crevice

As described in the Results Section 3.4., during the RCA experiments light green deposits around the outside edge of the RCA were found after long periods of exposure. When crevices were opened after the test, additional crevice corrosion products were found on the metal surface inside the crevice. EDS and ICP analysis on both types of crevice corrosion products were performed.

As a general trend it was found that: (*i*) over time the crevice corrosion products inside the crevice became enriched in Mo, Nb, and O, and (*ii*) the crevice corrosion products found outside, around the mouth of the specimen become enriched in Ni, Cr, Mo, and O. This behavior can be explained with the aid of the Pourbaix diagram for each one of the species under study, see Figure 1. Assuming that the potential of the crevice wall down the length of the crevice is 0 V vs SCE and that a pH of the crevice solution reaches a value of 0, the most stable species for Ni, Cr, and Fe are Ni^{+2}, Cr^{+3}, and Fe^{+2}. These species are highly soluble in acidic conditions, so it can be expected that they diffuse out of the crevice, and either dissolve in solution or precipitate around the crevice mouth of the specimen due to the drastic change of pH encountered in the bulk solution. Mo^{3+} becomes stable at pH values <-0.28. At slightly higher pH values it can exists as $MoO_{2(s)}$ or the soluble species $Mo(OH)_2^+$. Thus, soluble and solid species could exist within the crevice depending on the pH. Some of the soluble Mo may move towards the crevice mouth and precipitate out as $MoO_{2(s)}$ around the crevice mouth upon reaching the higher pH solution at the exterior of the crevice. Nb is expected to have a different behavior. At all pH values, even extreme pH conditions, the most stable species of Nb^{5+} is $Nb_2O_{5(s)}$, a solid. Thus, Nb is found in the internal crevice corrosion products.

EDS and ICP results obtained at 18 hours (Figures 77 and 80) suggest that alloy 625 dissolves preferentially, as the relative concentration of the elements are not in the stoichiometric ratio in which they appear in the alloy. However, it is plausible that as soon as the alloy dissolves, the highly soluble cations migrate and diffuse out at fast rate, causing the solution that remains within the crevice to appear non-stoichiometric. This interpretation is supported by the higher relative wt% of the highly soluble cations in the bulk solution outside the crevice. Considering this, it appears that when alloy 625 actively dissolves, it follows a stoichiometric dissolution, as was proposed by Shan and Payer [67] for alloy 22.

A proposed mechanism of the evolution of crevice corrosion products over time, including consideration of diffusion and migration, is as follows: At early times, i.e. 18 hours, Ni, Cr, Fe, and Mo cations move out of the crevice via diffusion and migration, leaving Nb and possibly Mo solids on the metal surface (Figure 98 (a)). As the soluble species reach the crevice mouth, the drastic change of pH, i.e. pH=8.2, causes a portion of these to precipitate in the form of oxide/hydroxide precipitates: $Cr(OH)_3$, $Fe(OH)_2$ and MoO_2. As time progresses, i.e. 30 hours, the volume of Ni, Cr, Fe, and Mo cations passing through the crevice mouth is such that the precipitate becomes noticeable. As this same time, the bulk solution starts becoming rich in Ni content, since in the bulk solution pH, Ni^{2+} is a soluble species (Figure 98(b)). The absence of Nb content in the corrosion products outside of the crevice at early times (18 and 30 hours) is because Nb exists as a stable precipitate inside the crevice, likely Nb_2O_5.

By 60 hours of exposure, when the crevice corrosion damage reaches a critical distance x_{crit}, near the crevice mouth and higher dissolution rates are attained, solid crevice corrosion products (i.e. MoO_2 and Nb_2O_5) start to accumulate near the crevice mouth at higher rate, and the soluble crevice corrosion products continue to diffuse out. The bulk solution at this point still contains a significant amount of Ni^{2+} dissolved in solution (Figure 98 (c)). At x_{crit}, the crevice corrosion damage does not continue moving forward since it is not possible to maintain a CCS this close to the crevice mouth.

As time progresses, high dissolution rates are attained causing the buildup of solid crevice corrosion products at x_{crit}. At this point crevice corrosion damage begins going deeper into the face of the specimen behind x_{crit}, and starts moving towards the crevice tip. As the specimen continues corroding near the crevice mouth, soluble cations continue diffusing out of the crevice, causing a higher volume of precipitates to form around the crevice mouth. Eventually, some of the solids formed around the specimen fall off and stay as precipitates in solution. This might explain why a higher amount of Cr, Fe and Mo were detected in the bulk solution after 2 weeks of immersion (Figure 98 (d)). Regarding Mo content, it is possible that some of this element is present in the bulk solution as MoO_4^{-2}, which becomes stable at the pH of the bulk solution. The small presence of Nb content in the crevice corrosion products found outside the crevice after 2 weeks of immersion can be attributed to the short diffusion path at this time between the corrosion site and the crevice mouth. As other elements diffuse out, some Nb_2O_5 can be dragged out as well.

(a) 18 hours

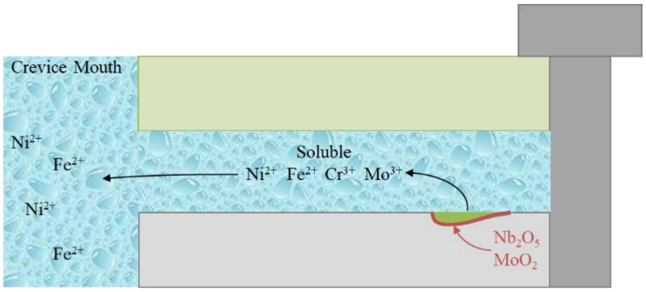

- Alloy 625 actively dissolves.
- Soluble cations diffuse out of the crevice.
- Small amounts of Nb precipitate as Nb_2O_5 and some amount of Mo may precipitate as MoO_2.

(b) 30 hours

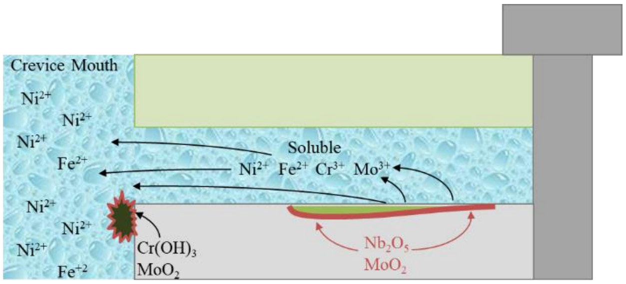

- As time increases, the volume of soluble cations increases, and some of them start to precipitate out when reaching the bulk solution.
- Nb continues precipitating as Nb2O5 on the metallic surface.

(c) 60 hours

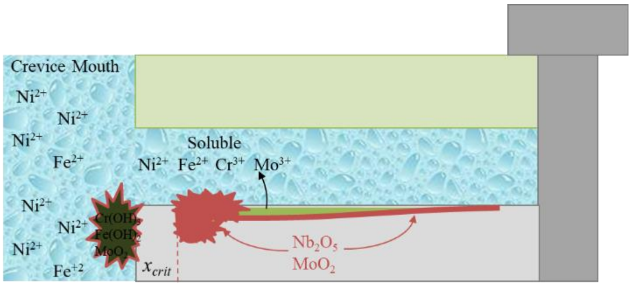

- Crevice corrosion damage reaches x_{crit}.
- Bulk solution becomes richer in Ni^{2+}.

(d) 2 weeks

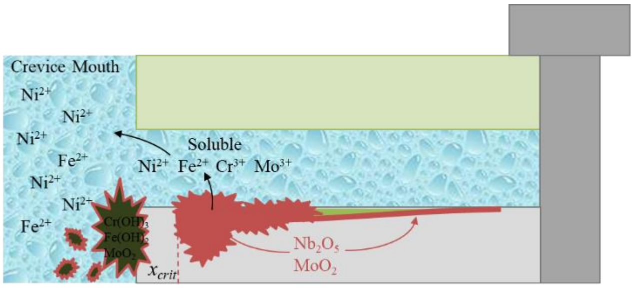

- High dissolution rates are attained near the crevice leading to higher precipitation of solid corrosion products and diffusion of soluble corrosion products.
- Crevice corrosion precipitates from around the crevice start to fall in off in solution.

Figure 98. Evolution of corrosion products over time during crevice corrosion of alloy 625.

4.3. Stages of Crevice Corrosion

Crevice corrosion in nickel alloy 625 was studied under potentiostatic control in an ocean water environment using a Remote Crevice Assembly (RCA). Three different applied potentials were used: 100, 200 and 300 mV vs SCE. All experiments were carried out at room temperature. As a general trend it was found that increasing applied potentials showed more extensive damage and deeper penetration at similar exposure times. Higher applied potentials showed deeper damage near to the mouth, as compared to lower potentials. Additionally, the total charge passed values was larger at higher potentials, as is summarized in Tables 12-16 and Figure 67. Similar results have been reported by Martin et al. in their study of the crevice corrosion in alloy 625 [65], [66]. An attempt to elucidate the mechanism of how crevice corrosion in alloy 625 occurs when exposed to an ocean water environment is presented in this section.

Based on the crevice corrosion damage profiles and the *I vs t* curves obtained from the anodic potentiostatic data, and analysis of crevice corrosion products over time, we have proposed a mechanism for crevice corrosion in nickel alloy 625 in an ocean water environment, separated into three different stages: Stage I – *CCS development and initiation of crevice corrosion*, Stage II – *Movement of the active front*, and Stage III – *Stable crevice corrosion propagation*. These stages are represented in Figure 99. This general trend in the *I vs t* response has been found to be typical for all three applied potentials under study.

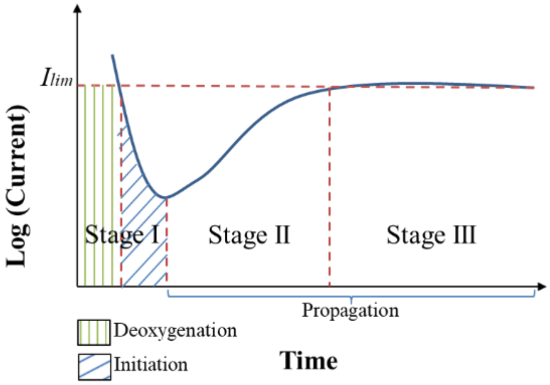

Figure 99. Illustration of I vs t *curve trend with the respective stages of crevice corrosion.*

A mathematical modeling effort for determining the spatial and temporal potential, current and damage profiles for nickel alloy 625 considering these three different stages has been developed by Stenta et al. [105], [106].

4.3.1. Stage I – Development of a Critical Crevice Solution and Initiation of Crevice Corrosion

During Stage I, the *I vs t* curves are characterized by a rapid decrease in the current values. At t=0, anodic and cathodic reactions occur at the same rate both within the crevice and on the boldly exposed surface. As a result, an oxide film forms and thickens over the entire surface, both inside and outside the crevice, and the total current decreases [44], [107]. The difference in oxygen content and cathodic current density between the outer surface and the interior of the crevice becomes large. Within the crevice, cathodic reactions are limited by the depleting oxygen content, while anodic reactions continue to occur. The continuous release of metal cations within the crevice (i.e. Ni^{2+}, Cr^{3+}, Fe^{2+}, Mo^{3+}, and Nb^{5+}) and their subsequent hydrolysis reactions result in a decreasing pH in the crevice solution. Due to the increase of metal cations in solution and the increase of cell current, Cl^- migrates into the crevice. The result is an acid solution rich in metal chlorides. Both the H^+ and the Cl^- increase the rate of anodic reaction, causing the passive film to begin dissolving and become unstable [108]. The acidification and the increase of chloride content of the crevice solution produces a CCS sufficient to cause the activation of anodic sites, and crevice corrosion initiates. In all instances (more than 30 observations), it was always found that the initiation of crevice corrosion damage occurred near the tip of the crevice, far from the crevice mouth.

Due to the large depth-to-gap aspect ratio found in the RCAs, i.e. 1.27cm/0.005cm, it is very likely that the diffusion and migration of species (mass transport), rather than a potential drop (IR) down the length of the crevice, are the predominant factors in this stage. This concurs with the mathematical model of Watson and Postelwaite [59], where the CCS theory predicts that the most severe attack will occur at the deepest part of the crevice, i.e., at the most occluded portion.

4.3.1.1. Depletion of Oxygen within the Crevice

Over time the dissolved oxygen within the crevice is depleted since the reduction process occurs faster than the diffusion of oxygen into the crevice. The reduction reaction that occurs is: $O_2 + 2H_2O + 4e^- \rightarrow 4OH^-$. As proposed by Oldfield and Sutton [44], the time required for the depletion of oxygen (t_d) during Stage I, ignoring any diffusion, can be calculated with the following expression:

$$t_d = \frac{nF[O_2]_0}{i_{pass}} g \qquad \text{Equation 25}$$

where, *n* is the number of equivalents per mol for oxygen reduction reaction, *F* is the Faraday's constant *F*=96485 C/mol, $[O_2]_0$ is the initial concentration of oxygen in moles/cm^3, *g* is the average crevice gap for a metal/insulator crevice (or half the average gap for a metal/metal crevice) in cm, and i_{pass} is the passive current density in A/cm^2.

Using $[O_2]_0$= 2×10^{-7} moles/cm^3, i_{pass} =1×10^{-6} A/cm^2, and *g* =0.005 cm, the deoxygenation time was estimated to take ~ 385.9 s (6.43 min). This agrees with optical microscope observations of RCA specimens polarized at 200 mV vs SCE for 5 min; at 5 min, the specimen remains passive with no signs of crevice corrosion attack.

4.3.1.2. Initiation of Crevice Corrosion

After deoxygenation occurs, crevice corrosion damage attack is observed near the crevice tip of the RCA specimens within the first 10-15 min of anodic polarization. The total current continues to decrease during Stage I. Figure 100 shows (a) the *I vs t* response and (b) the respective crevice corrosion damage attack obtained for a total exposure period of 45 min (0.75 h). Similar results were obtained from the time-lapse video specimen at 300 mV (Figure 101), where crevice corrosion damage is visually observed at 10 min, even as the total current response continues to decrease. In 300 mV specimen, however, the total current started to increase after 30 min of anodic polarization.

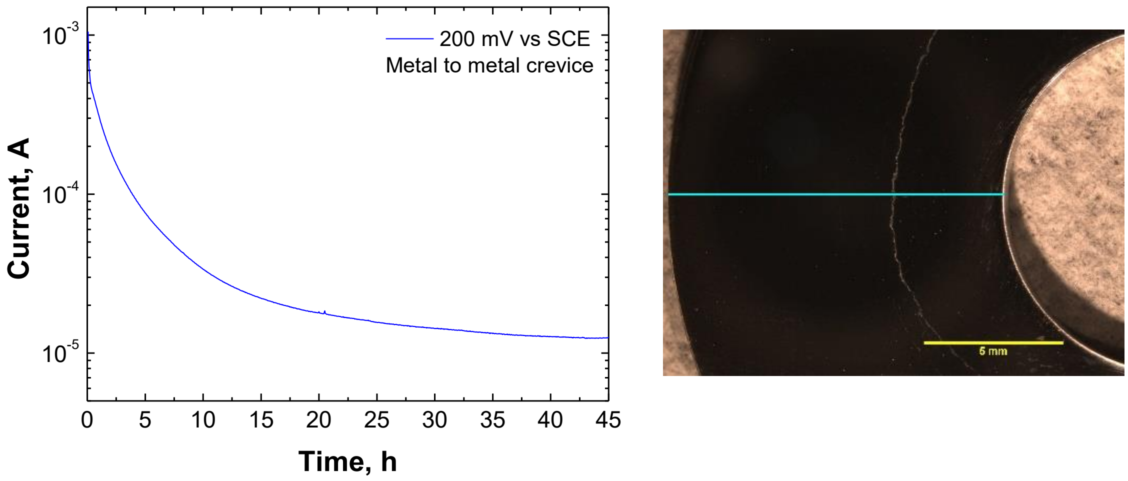

(a) (b)

Figure 100. (a) I vs t *curve and (b) optical micrograph of crevice corrosion attack obtained on a RCA specimen polarized at 200 mV vs SCE for 45 min. Applied torque: 10 ft-lb.*

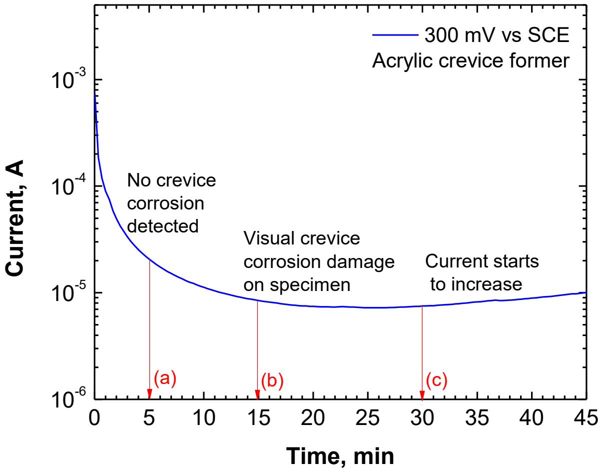

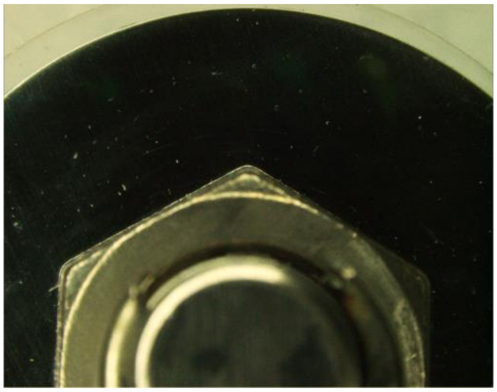

(a) Exposure time: 5 min. No visual damage

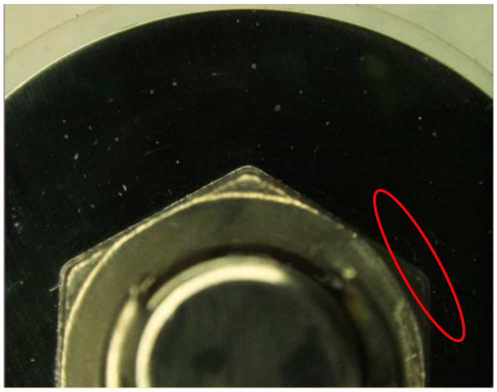

(b) Exposure time: 10 min. Visual crevice corrosion damage on specimen.

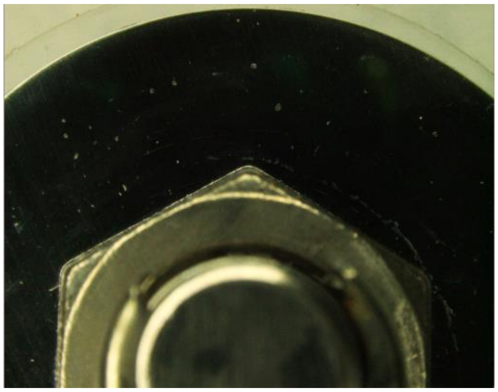

(c) Exposure time: 30 min. Current starts to increase.

Figure 101. I vs t *curve of anodic polarization of a RCA specimen polarized at 300 mV vs SCE for 60 hours. Applied torque: 10 ft-lb.*

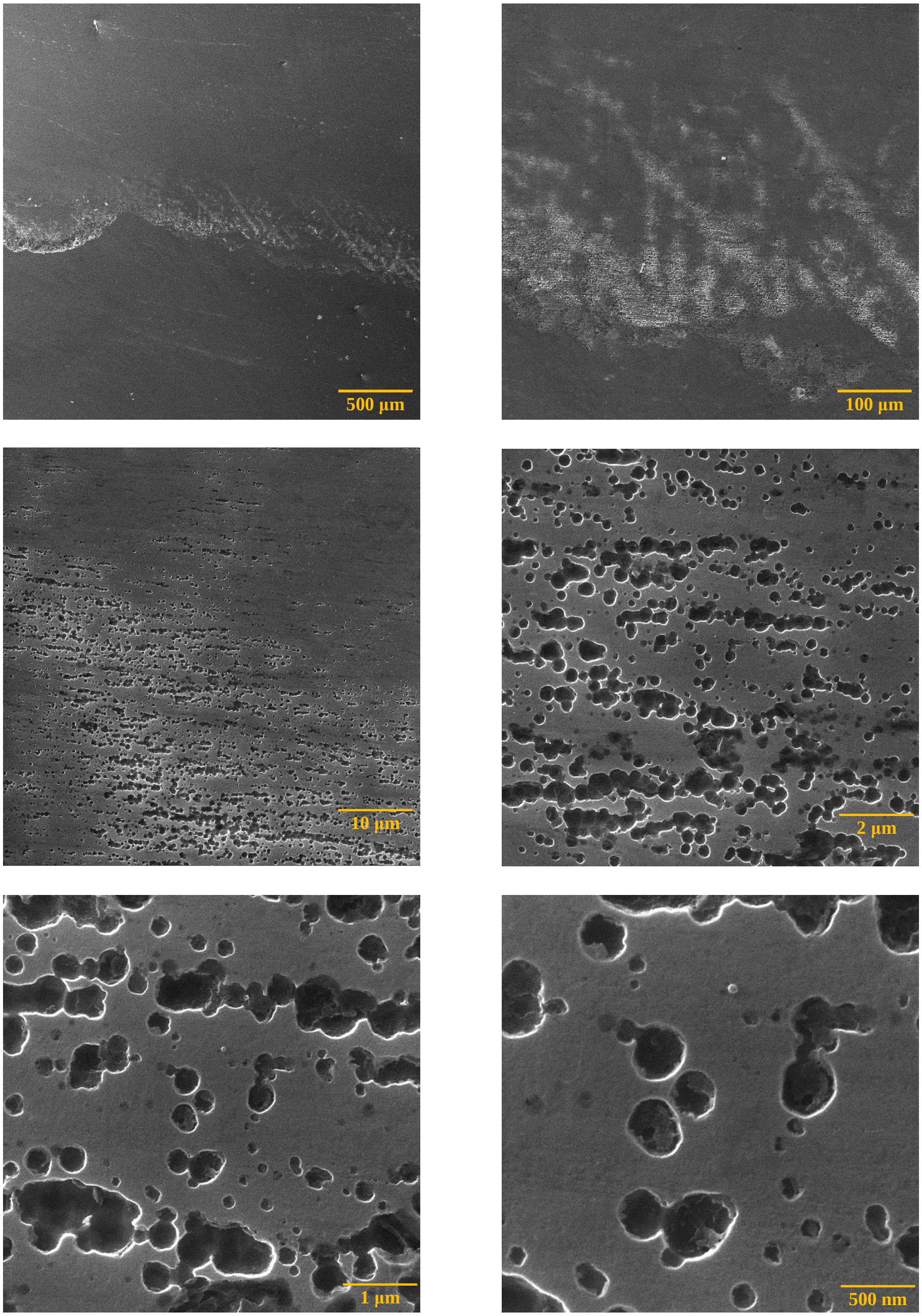

Figure 102. SEM images of crevice corrosion attack obtained on a RCA specimen polarized at 200 mV vs SCE for 45 min. Applied torque: 10 ft-lb.

When magnifying the crevice corrosion damage shown in Figure 100 (b) with the aid of SEM, there appears to be etching damage consistent with attack by concentrated acid, see Figure 102. This indicates that the critical crevice solution (CCS) has already formed. When magnified at 100 kX, the diameter of pits can be seen to vary between 100-500 nm. These observations are in agreement with studies done in Alloy 600 and alloy 625 and its susceptibility to crevice corrosion [45], [109]. It is interesting to note that even though there is some damage caused on the specimen surface, the total current continues to decrease at this time. It is likely that the anodic current produced by this etching damage is several orders of magnitude smaller than the total passive current density i_{pass} of the RCA specimen, thus masking its contribution.

In this study, Stage I is considered to be the period at which the total current reaches the minimum value in the *I vs t* curve, as illustrated in Figure 99. Thus, during Stage I, two important subsequent events occur: (*i*) the deoxygenation within the crevice and (*ii*) the development of the CCS. The deoxygenation event requires less than 10 min. During initiation, the total current continues to decrease until a CCS within the crevice forms and the total anodic current is high enough to perceive an increase in the total current response.

4.3.2. Stage II – Crevice Corrosion Propagation: Movement of the Active Front

Once anodic sites have been activated and the formation of a CCS occurs in the back of the crevice, both the active front and the CCS solution start moving towards the crevice mouth and eventually out of the crevice via diffusion. As the active front moves, the CCS solution increases in volume and concentration due to its autocatalytic nature. The ions produced in the oxidation reactions occurring at the metal surface move through the solution under the influence of two gradients: the concentration gradient and the potential gradient. It was found that at early times during this stage, changes to the potential gradient (in the less noble direction) had a small effect on the propagation current. In pitting corrosion, it has been found that the current density response is independent of the applied potential in the diffusion control regime [33], [110]–[112]. Also, at early times, it was found that the crevice repassivation potential was on the order of 80 mV vs SCE. As the active front and the CCS move towards the crevice mouth, the depth of the crevice (or diffusion length) decreases, and an increase in the current density occurs. At some point, the CCS and active area reach a critical point of maximum approach to the crevice mouth, x_{crit}, at which forward propagation stops (Figure 103). This distance has been explained as the point at which it is no longer possible to maintain the CCS from a mass transport standpoint [44], [45], [58]. At x_{crit}, it was found that changes to the potential gradient had a large effect on the propagation current. When crevice corrosion damage reached x_{crit} the crevice repassivation potential was found to be much higher, on the order of 170-190 mV vs SCE.

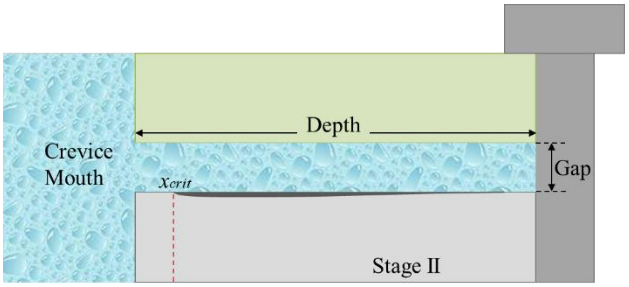

Figure 103. Stage II of crevice corrosion. The active front and CCS reach a critical distance (x_{crit}) near the crevice mouth.

4.3.2.1. Critical Distance (x_{crit}) and Limiting Current (I_{lim}) at Different Applied Potentials

It was found that different applied potentials had an effect on the distance of maximum approach (x_{crit}) to the crevice mouth and the maximum current (I_{lim}), as is summarized in Table 20. At higher applied potentials, I_{lim} was higher and x_{crit} moved closer to the crevice mouth.

Table 20. x_{crit} and I_{lim} values as a function of applied potential.

Applied Potential (mV vs SCE)	**Distance of maximum approach from crevice mouth, x_{crit} (µm)**	**I_{lim} (A)**
100	2920±364	$(5.23\pm2.71)\times10^{-4}$
200	2218±360	$(1.23\pm0.28)\times10^{-3}$
300	1692±416	$(1.74\pm0.18)\times10^{-3}$

According to the mass transport consideration of the Oldfield and Sutton model [44], [45], the active site where crevice corrosion initiates occurs a critical distance from the crevice mouth, deep inside the crevice, as a long diffusion path aids in the development of a CCS. This is consistent with the results presented in this work, as is shown in Stage I, where crevice corrosion initiates near the crevice tip. However, as crevice corrosion propagates, and the CCS also moves over time, a new critical crevice distance is attained closer to the crevice mouth, now with a shorter diffusion length. The distance of maximum approach to the crevice mouth is referred in this text as x_{crit}.

As the active front of crevice corrosion and the CCS move towards the crevice mouth, the dissolution rate also increases. Thus, the dissolution rate becomes a key factor for maintaining a CCS near the crevice mouth. Therefore, x_{crit} is the critical diffusion length necessary to maintain a CCS near the crevice mouth and it is dependent on the dissolution rate. Based on the time-lapsed video results, it was found that x_{crit} also correlated with the maximum current (I_{lim}) obtained on the I *vs* t curve. As the crevice corrosion propagated, the current remained nearly constant at I_{lim} (Stage III). Thus, when x_{crit} stops its movement toward the crevice mouth, this marks the end Stage II and the beginning of Stage III.

4.3.2.2. Current Density and Corroded Area Calculations

During Stage II, as the total current increased over time, the total corroded area due to crevice corrosion also increased. With the aid of the time-lapse video, it was possible to track the evolution of corroded area over time, and a calculation of the current density with time and spatial location within the crevice was possible. The calculations shown in this section are based on the results obtained from the RCA specimen polarized at 300 mV vs SCE for 60 hours, see Figure 61.

Observations of the corroded area over time indicated that once crevice corrosion initiated in tip of the crevice, it moved towards the crevice mouth. Based on visual analysis, the anodic reaction in the area left behind appears to shut off. An image analysis of the moving active front is shown in Figure 104. The area of the active front, Δ_A, can be calculated as the difference in images between any two video time steps, t_1 and t_2.

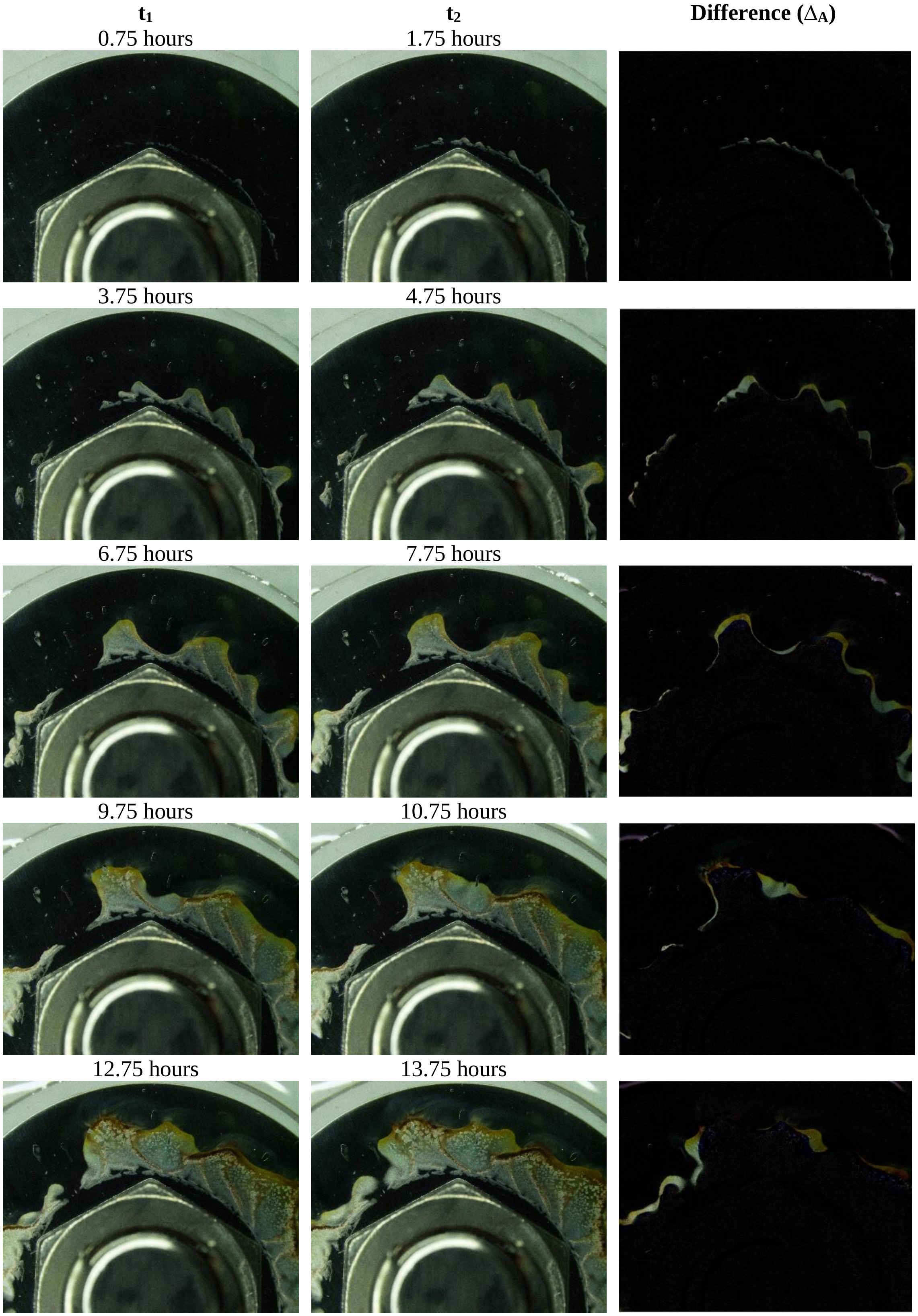

Figure 104. Moving front of crevice corrosion damage over time.

In this study, only a section of the washer could be used for determining the corroded area over time, as illustrated in Figure 105. The area of the sector under study can be calculated as follows:

$$A_{sector} = \frac{\theta \pi r^2}{360} \qquad \text{Equation 26}$$

where θ=100° and r=1.905 cm.

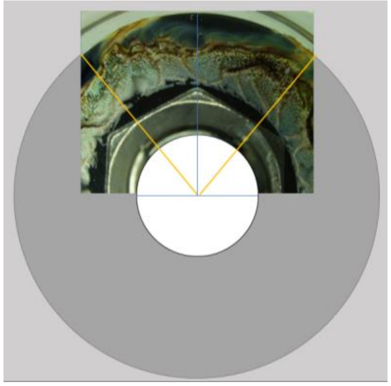

Figure 105. Section of corroded area under study. $A_{sector}=\pi\theta r^2/360$, *with* θ=100° *and r=1.905 cm.*

It is important to note here that the current response obtained during the anodic potentiostatic polarization reflects the response of the total area of the specimen. Since only one portion of the total specimen was used for studying crevice corrosion propagation, as shown in Figure 105, it is necessary to correct the delta-corroded-area (ΔA) values. It was assumed that the whole specimen would corrode at the same rate as the sector under study. This holds true, since the whole specimen corroded radially, as shown in Figure 61. To perform this correction, the ratio between ΔA and area of the sector was calculated according to Equation 27:

$$r = \frac{\Delta A_{corroded}}{A_{sector}} \qquad \text{Equation 27}$$

Thus, the total delta-corroded-area (ΔA_t) can be calculated as follows:

$$\Delta A_t = r \times A_{specimen} \qquad \text{Equation 28}$$

where $A_{specimen}$ is the area of the whole specimen with a value of 10.17 cm^2.

Once the total delta corroded area (ΔA_t) for each time step (Δt) was calculated, the current density of the active front was calculated as follows:

$$i_{active\ front} = \frac{I}{\Delta A_t} \qquad \text{Equation 29}$$

where I is the total current obtained from the anodic polarization curve at Δt=900 s, starting from 0.75 hours.

The total corroded area over time, and the corresponding calculated current density of the active front, for the first 17 hours of anodic polarization are shown in Figure 106. As seen in this figure, the current density of the active front increases as time progresses. Implications of these findings on the CCS concentration and the *IR*-drop along the length of the crevice will be discussed later in this text.

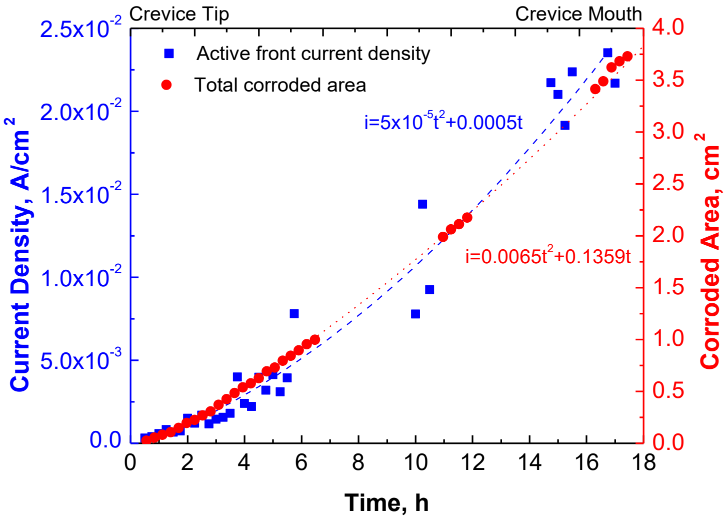

Figure 106. Total corroded area and active front current density vs time. From time lapse video of specimen polarized at 300 mV vs SCE for 60 hours and 10 ft-lb torque. Δt=900 s.

The calculation of the current density allows for the measurement of the corrosion rate at which crevice corrosion is occurring. From this current density, it was possible to calculate the corresponding mass loss. The corresponding charge passed was compared to the experimental *I vs t* curve in Figure 61. The experimental charge passed was 1.9 C equal to a mass loss of 0.50 mg. The mass loss that would occur at the active front in these calculation is 0.42 mg, indicating that the active front assumption is a reasonable mechanism for crevice corrosion propagation in Stage II.

4.3.2.3. Current Density vs Crevice Depth Calculations

An attempt at calculating the current density vs spatial location within the crevice is presented here. Since the geometry used in RCA experiments was circular, an equivalent radius (r_{eq}), which is the distance from the active site to the crevice mouth, based upon the crevice corrosion damage over time, was calculated using the following equation:

$$r_{eq} = \sqrt{\frac{A_{corroded}}{\pi}} + 0.635 \qquad \text{Equation 30}$$

where $A_{corroded}$ is the total corroded area in cm^2 as time progresses. The calculation of the depth (x) of the active site is then calculated as:

$$x = 1.905 - r_{eq} \qquad \text{Equation 31}$$

The current density of the active front down the crevice length is shown in Figure 107. Using Equation 31, the distance of x_{crit} from the crevice mouth at 17 hours of exposure was estimated to be 0.143 cm. As obtained from the time lapse video, the average distance of x_{crit} from the crevice mouth at 17 hours of exposure was 0.233 cm. Based on this, the estimated distance based on an equivalent radius calculation (such as Equation 31) seems to be a good approximation of the distance obtained from visual observation, with a difference of less than 1 mm.

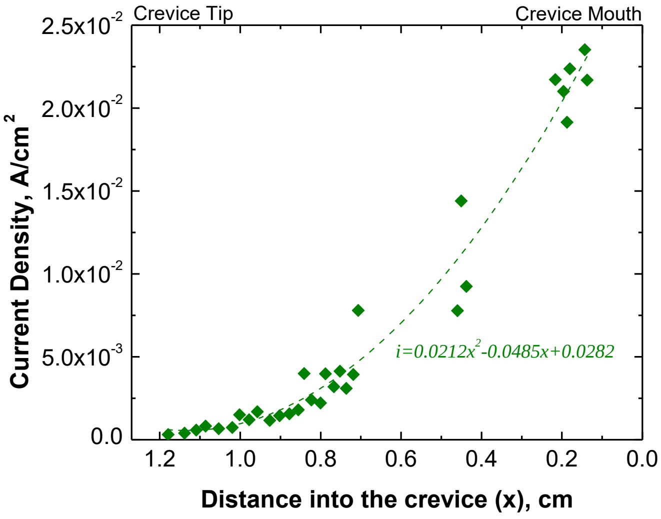

Figure 107. Current density of the active front along the crevice depth.

4.3.2.4. *Calculation of the IR-drop Down the Length of the Crevice*

The calculation of the current density vs position within the crevice (Figure 107), also allows for the calculation of the IR-drop down the length of the crevice, which can be estimated using Equation 32.

$$E = E_{app} - IR \qquad \text{Equation 32}$$

where E_{app} is the applied potential, *I* is the total current, and *R* is the resistance of the solution. *R* was calculated according to the following equation:

$$R = \frac{\rho L}{A_{crevice}} \qquad \text{Equation 33}$$

where ρ is the resistivity of the solution in Ω.cm, *L* is the crevice depth, and $A_{crevice}$ is the cross-sectional area of the crevice ($A_{crevice} = 2\pi rg$). The value of resistivity used for all calculations was the resistivity of the experimental 3.0 m NiCrFeMoNb solution, i.e. ρ =16.6 Ω.cm. Four different values of crevice gap were also used: 10, 30, 60, and 90 μm. Real crevice gaps measured with the aid of X-ray computed tomography were within 20-50 μm.

Results of the corrected potential (Equation 32) down the length of the crevice at different crevice gaps (10-90 μm), as a function of crevice depth and current density, are shown in Figures 108 and 109. It is important to note that in Figure 89 each data point represents the potential obtained at a specific time and location within the crevice; the figure does not represent a single moment in time. For example, at 4.5 hours of exposure and ~0.8 cm into the crevice, the potential of the crevice wall was calculated as ~–13 mV vs SCE.

As a general trend, Figures 108 and 109 show that the potential of the crevice wall changes significantly as crevice gap decreases. Similar results were reported in experimental studies of crevice corrosion of nickel by Abdulsalam and Pickering [54]. When the crevice gap reaches values of 30 μm and larger, the IR-drop becomes small and the potential of the crevice wall flattens. The results obtained for a crevice gap of 60 μm (as shown in Figure 90) are shown over the polarization responses of nickel alloy 625 in NiCrFeMoNb stoichiometric solutions in Figure 110.

The results shown in Figure 108 for 30 and 60 μm crevice gaps (which were typical crevice gap values in the RCAs) show that during Stage II, the *IR*-drop was not higher than 170 mV and 85 mV, respectively. Assuming that a 4.0 m NiCrFeMoNb solution is formed near the crevice tip, this calculated *IR*-drop is not enough to lower the potential of the crevice wall to the potential (E_{crit}) at which active dissolution of the alloy occurs (see Figure 110).

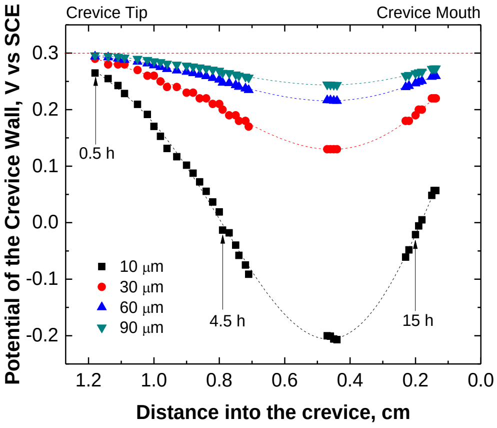

Figure 108. Potential of the crevice wall vs distance within the crevice assuming different crevice gaps (10-90 μm).

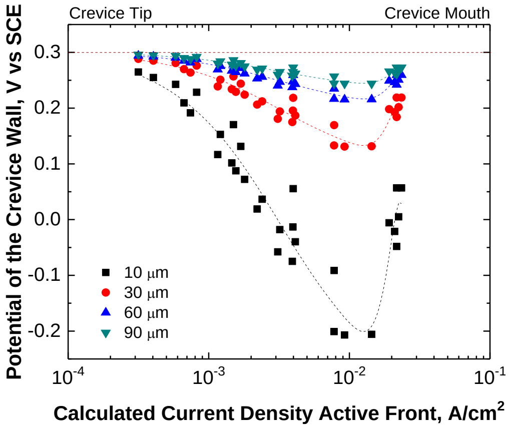

Figure 109. Potential of the crevice wall vs calculated current density of active front assuming different crevice gaps (10-90 μm).

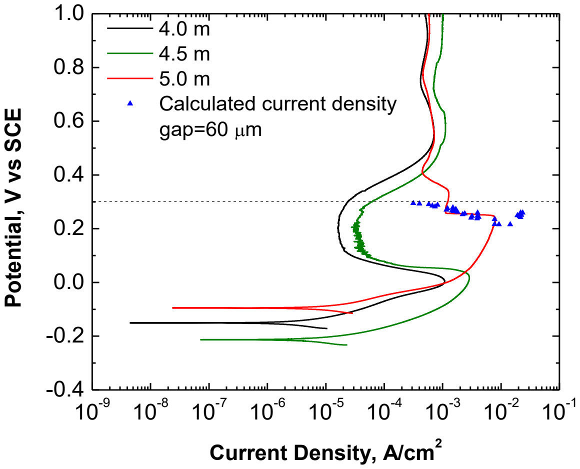

Figure 110. Calculated current density using g=60 μm vs experimental current densities obtained in NiCrFeMoNb solutions.

4.3.2.5. Concentration of the Active Front Calculations

An estimate of the concentration of the solution obtained within the crevice can be calculated based on the information obtained from the current density calculations as a function of distance along the crevice length (Figure 107). However, several simplifications were made. The first simplification is to combine the effect of all the cations into one hypothetical species, i.e. Me^{n+}. In the case of alloy 625, the cations considered were Ni^{2+}, Cr^{3+}, Fe^{2+}, Mo^{3+}, and Nb^{5+}, and the average valence number was n=2.37. The diffusion length is the crevice depth (x), and the diffusion coefficient was assumed constant with a value of $D=7.2\times10^{-6}$ cm^2/s. Hydrolysis reactions of the different cations are not considered.

The positive ion current produced by the oxidation of cations occurring at the metal surface diffuses through the solution under the influence of two driving forces, namely the concentration gradient and the potential gradient, as is given by the Nernst-Einstein equation below [110]:

$$\frac{I}{AnF} = -D\left[\frac{\partial C}{\partial x} + \bar{C}\frac{nF}{RT}\,D\,\frac{\partial \varphi}{\partial x}\right] \qquad \text{Equation 34}$$

However, in this study, the potential gradient in solution has been shown to have a small contribution (Figure 110). Isaacs [113] has shown that in potentiostatic experiments almost all the potential drop is attributed to a thin resistive layer present on the electrode surface. In their studies of pitting corrosion, Frankenthal and Pickering [114], [115] also observed that most of the potential drop was attributed to the formation of hydrogen bubbles on the metal/solution interface. Equation 34 can be simplified to:

$$\frac{i}{nF} = -D\,\frac{\partial C}{\partial x} \qquad \text{Equation 35}$$

where i is the current density, n is the valance number, and F=96485 C/equiv.mol.

Based on the current density vs distance plot presented in Figure 88, the current density i can be written as a function of crevice depth according to the following function:

$$i(x) = 0.0212x^2 - 0.0485x + 0.0282 \qquad \text{Equation 36}$$

Thus, Equation 35 can be solved to determine the concentration of the metal cations in solution, based only on diffusion. The boundary condition for solving Equation 35 was C=2.3 M (2.5 m) at $x=L$.

As a note, Equation 36 comes from experimental data of crevice corrosion damage that occurred from 0.75 to 17 hours. At 0.75 h, a CCS was already formed, and active dissolution was occurring. Based on the experimental CCS study presented in Section 4.1, it was found that a critical concentration of NiCrFeMoNb solution with a minimum concentration of 2.5 m was necessary to cause activation of alloy 625. Therefore, it was assumed that, at the tip of the crevice, a solution with this concentration was already formed. As such, this concentration was selected as the boundary condition to solve Equation 35.

Results of the concentration profile along the crevice length *x*, i.e. *i=f(x)*, are shown in Figure 111. Additionally, the concentration profile as a function of the current density, i.e. *i=f(c)*, is shown in Figure 112. The saturation limit of a NiCrFeMoNb stoichiometric solution was predicted by OLI-software to be 5.5 m (4.4 M), and is shown on Figure 111 and 112 as a reference.

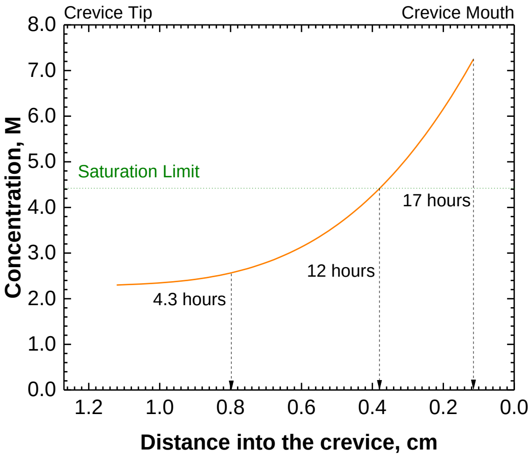

Figure 111. Concentration of the active front in molar as function of distance and time.

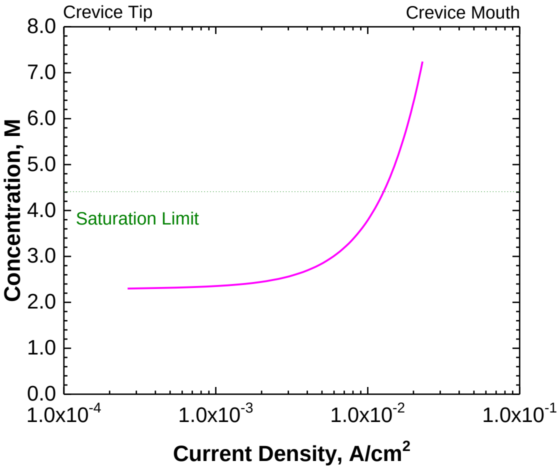

Figure 112. Concentration of the active front in molar as a function of current density.

Figures 111 shows that as the active front moves towards the crevice mouth, changes in the composition of the CCS occur, increasing the metal concentration of cations in solution. This, in turn, makes the solution pH decrease, and increases the concentration of Cl^-, as has been demonstrated in the OLI calculations in section 3.2. As seen in this figure, the saturation limit is reach at around 12 hours, which corresponds to a distance of approximately 0.38 cm from the crevice mouth. Additionally, from the time lapse video (see Figure 62), precipitation of crevice corrosion products can also be seen at this time.

The increase in both the current density and the concentration of the CCS as the active front moves towards the crevice mouth suggest that, over time, the shape and magnitude of current densities of the polarization curve changes. This differs from the traditional *IR**-model and the mixed *CCS-IR**-model, where it is assumed that once E_{crit} is reached, crevice corrosion stabilizes at a single rate determined by the active peak (i_{crit}) of the polarization curve.

4.3.3. Stage III – Stable Crevice Corrosion Propagation

This is the third stage of crevice corrosion, and occurs when both x_{crit} and the maximum current value from the *I vs t* curve are reached. At x_{crit}, the active area cannot support further movement of the CCS toward the crevice mouth, and propagation vertical to the surface (penetration depth) occurs at an increased rate, as is depicted in Figure 113. At this point, the rate of dissolution is higher than the diffusive transport, resulting in solution saturation and precipitation of corrosion products, and, quite possibly, a Ni base salt film. The current here remains at a constant value I_{lim}, and stable crevice corrosion propagation is achieved.

Studies on pitting corrosion of nickel and stainless steels using a 1D artificial pit electrode experiment have shown that, in sufficiently deep pits, high currents in the bottom of the pit lead to the supersaturation of metal cations and the subsequent precipitation of a salt film on the dissolving metal. Once a salt film forms on the metal surface, the dissolution rate stays constant and the corrosion rate is limited by the dissolution of the salt film, i.e. the anodic dissolution of the metal/alloy transitions to diffusion control [38], [110], [112], [116]–[118]. Isaacs [116] has shown that the salt film displays ohmic resistance which is controlled by its thickness. An increase of the salt film thickness increases the salt film's resistance, causing the pit bottom to reside at lower potentials (*IR*-drop).

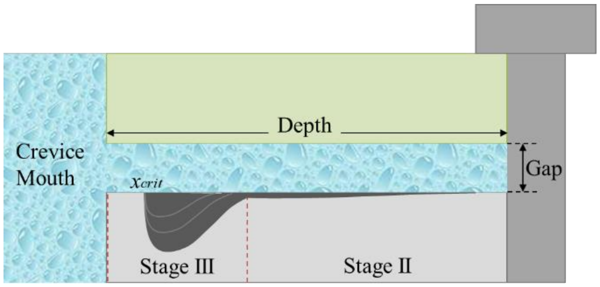

Figure 113. Crevice corrosion propagation damage during Stage III

Crevice corrosion morphology of RCA specimens during Stage III also showed that crevice corrosion morphology at x_{crit} transitions from surface etching to surface brightening (see Figure 72). Studies of nickel specimens by Datta & Landolt [104], [119] showed that high dissolution rates and the formation of a salt film on the surface lead to surface brightening. A significant amount of crevice corrosion products, oxides and metal salts, were found near the crevice tip when the specimens were opened and analyzed. These products were also observed during the time lapse video during Stage III. The crevice corrosion products found on the surface at x_{crit} where characterized mainly as Mo and Nb oxides.

4.3.3.1. Crevice Repassivation

The main objective of using the modified T.H.E. experiment in this study was to determine the repassivation potential of crevice corrosion of alloy 625. Studies of crevice corrosion repassivation potentials of nickel alloy 22 using the T.H.E. method had been done by Evans et al.; however, it was found that the amount of charge passed during anodic polarization to grow the localized corrosion did not influence the value of repassivation potential [97]. In this study, when RCA specimens were studied at different exposure times (or charge passed) it was found that the repassivation potential varied significantly, ranging from 80 mV vs SCE up to 190 mV vs SCE. The lower the charge passed, the lower the repassivation potential.

From the modified T.H.E. results, it was found that during Stage II, when the active front is placed at distances far from the crevice mouth, the propagation rate was dependent on the potential; i.e. when decreasing the potential gradient (in the less noble direction), the propagation of crevice corrosion was also decreased, and crevice corrosion continued moving towards the crevice mouth. This behavior was observed in RCA specimens that were propagated for 12 hours, as is shown in Figure 83. This behavior was also observed in RCA specimens that were propagated for 24 hours and 30 hours, as is shown in Figures 84 and 85. When the CCS is located near the crevice tip, two different fluxes start playing an important role in crevice corrosion propagation: (*i*) the diffusion flux of the metal cations, and (*ii*) the dissolution rate of the metal cations that occur between the metal/CCS interface. Near the crevice tip, it was found that current density and the CCS concentration are both low. As the applied potential decreases, the dissolution rate also decreases; however, at early times, the crevice length is large enough to prevent the dissolution of the CCS via diffusion, and crevice corrosion continues occurring at a lower rate. As the applied potential continues to decrease, the current density (dissolution rate) is not high enough to maintain a critical concentration of CCS, causing crevice corrosion repassivation.

Modified T.H.E. experiments were also performed during stage III. Once the active front reaches x_{crit} during Stage III, where high dissolution rates are necessary to maintain a CCS, it was found that small changes in the applied potential (in the less noble direction) cause the propagation rate to decrease, and repassivation of the crevice occurs. Thus, when the active front is closer to x_{crit}, small changes in the applied potential gradient, also in the less noble direction, resulted in a decrease of the propagation rate and eventual repassivation. When a salt film is formed at the crevice surface in Stage III, two different mass transport fluxes have to be taken into consideration: (*i*) the flux or rate of dissolution of the metal cations that occurs between the metal/salt film interface, and (*ii*) the flux or rate of dissolution of the salt film at the salt film/solution interface. This later flux also determines the diffusion of metal cations outside the crevice [108], [120]. At steady state crevice corrosion propagation, i.e. at a constant current, these two fluxes are equal, and the thickness of the salt film remains constant. However, if the applied potential is decreased, the rate of dissolution of the metal cations decreases and the salt film equilibrium is lost. The anodic dissolution rate becomes lower than the diffusion flux, resulting in a decrease of the salt film thickness and, in turn, a decrease of the salt film resistance. If the applied potential continues to decrease, the salt film eventually dissolves, and the anodic dissolution rate is not fast enough to maintain the CCS near the crevice mouth; since the diffusion length is short, the rate of diffusion becomes faster than the dissolution rate and the CCS diffuses, causing crevice corrosion repassivation.

From pitting corrosion studies of nickel and stainless steels, it has been found that there is a critical potential below which a salt film becomes unstable, and eventual pitting repassivation occurs [33], [117], [121]. The modified T.H.E. results obtained from the RCA specimens indicate that by stepping down the potential by 10 to 20 mV, the stability of a salt film is lost, and crevice corrosion repassivates. A combined effect of both mass transport and the stability of a salt film could explain the repassivation of crevice corrosion found in the RCA specimens.

Based on the observations of crevice corrosion damage profiles, it was found that applied potential plays a key role on crevice corrosion propagation and/or repassivation depending of the proximity of the active front to the crevice mouth. A summary of the repassivation potentials from the T.H.E. data is shown in Figure 114. As can be seen in this figure, during Stage II there is a dependence of $E_{rp,crev}$ on the propagation time and location of x_{crit}. This concept was also demonstrated, for pitting studies in stainless steels, by Srinivasan and Kelly [111], [120].

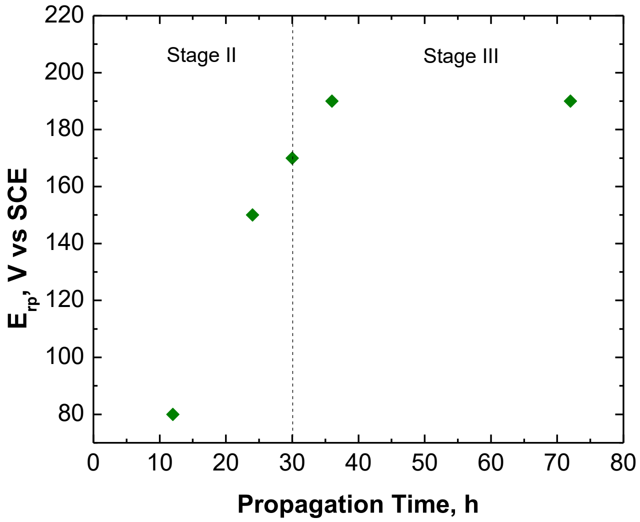

Figure 114. Repassivation potential ($E_{rp,crev}$) as a function of propagation time obtained from the modified T.H.E. method. Crevice corrosion was propagated at 200 mV vs SCE.

Based on Figure 114, the repassivation of crevice corrosion can be explained in the following manner: At early times, when the extent of crevice corrosion damage is small and the active front is far from the crevice mouth, the dissolution rate is the lowest, but the diffusion rate is the lowest here as well (see Figure 106). Although the dissolution is low, a CCS can still be maintained, even as the T.H.E. step-downs begin, due to the low diffusion rate, and the current density continues to increase, but at a lower rate with each stepdown. At some point during the stepping down, the applied potential becomes so low that a CCS can no longer be maintained, and crevice corrosion repassivates. As the concentration of the CCS decreases, the polarization curves changes, as is illustrated in Figure 155.

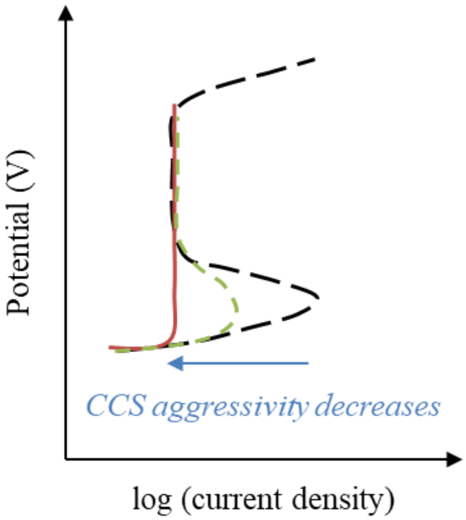

Figure 115. Evolution of polarization curve as the CCS concentration decreases

As the active front continues moving towards the crevice mouth, the current density values increase. At the same time, a shorter diffusion path is obtained, and higher diffusion rates are expected. Due to the increase in diffusion this close to the crevice mouth, the dissolution rate needed to maintain a CCS is much higher than deeper in the crevice, and a small change in the potential will have a large effect on the current density value. Thus, after only a few T.H.E. step-downs, crevice corrosion near the mouth repassivates. Repassivation potential can be defined as the potential at which the current density is no longer sufficient to maintain a CCS when confronted with the diffusion rate at a given distance from the crevice mouth.

4.3.3.2. Etching vs brightening damage

Based on the morphology of crevice corrosion over time, it was found that etching damage occurred at low current densities, and the chemistry change within the crevice caused the dissolution of the passive layer. Brightening of the surface occurred at high current densities, which promote the precipitation of a salt layer arising from mass transport limitations. Similar findings were proposed by Laycock and Newman [33] in their pitting studies on stainless steels. They proposed that any pit growing at an applied potential above the E_T (i.e. the transition potential between diffusion control and IR control) will have a salt film, and the dissolution rate will be determined by diffusion control. At lower potentials, the pit will grow in the active state. Pit growth in active state is believed to be responsible for the etch pits found at low potentials; on the other hand, the commonly observed polished morphology is due to the formation of a salt film on the surface [103], [121]. In his studies, Sato [121] made the distinction between these two different types of pitting morphology, and proposed that polished pits could only form when a critical concentration of chlorides was maintained within the occluded cell.

4.3.4. Mass Transport vs IR-control in Crevice Corrosion Propagation of RCAs of Nickel Alloy 625

Crevice corrosion in nickel alloy 625 was studied at three different applied potentials: 100, 200, and 300 mV vs SCE. If crevice corrosion is purely based on the *IR**-model, different applied potentials at the crevice mouth will affect the position of crevice corrosion initiation (x_{crit}) down the length of the crevice. This means that the position of i_{peak} on the polarization curve is found to shift farther inside (near the crevice tip) as the applied potential is increased because a greater ohmic drop is required to place the metal surface in the active region of the polarization curve, assuming a fixed solution concentration within the crevice. Based on this, as the potential is increased, the maximum attack (penetration depth) would be predicted to stay mostly constant as the x_{crit} position moves towards the tip [53]. However, based on the crevice corrosion damage profiles obtained at different applied potentials, it was found that as the potential increases, the crevice corrosion damage (x_{crit}) moves closer to the crevice mouth, and the penetration depth increases. These results contradict the *IR**-model and mixed *IR*-CCS* model for crevice corrosion propagation and suggest that a different mechanism is ruling crevice corrosion damage propagation in RCAs of alloy 625. Based on the results presented in this study, crevice corrosion was controlled by mass transport and applied potential. During Stage I, the depletion of oxygen occurs, leading to the formation of a CCS in the deepest part of the crevice. As time progresses, the CCS moves via diffusion (with propagation rate controlled by potential), until it reaches a distance of maximum approach near the crevice mouth (x_{crit}), where crevice corrosion transitions to Stage III. During this final stage, the dissolution rates reach a limiting current value, I_{lim}, and crevice corrosion damage starts going deeper into the specimen. The dissolution rate during this stage is controlled by the dissolution of the salt film formed on the surface and subsequent diffusion of the metal cations out of the crevice. In all three stages of crevice corrosion of alloy 625, mass transport and applied potential play a significant role.

V. CONCLUSIONS

5.1. Artificial Crevice Solutions

In this work, crevice corrosion propagation in alloy 625 has been studied by examining the polarization response of the alloy in metal salt solution that simulate the environment that develops inside the crevice. The effects of minor alloying additions Mo and Nb have been investigated as well as the role of Cl^- concentration using three separate solutions. From the results of these tests the following conclusions were drawn:

- The chloride salts of Mo and Nb dissolved in solution have the effect of lowering the OCP values and revealing an active to passive transition in the polarization curve of nickel alloy 625. Stoichiometric solutions with no Mo and Nb, but with an equivalent chloride content, did not show an active to passive transition or lower OCP. As such, it is concluded that Cl^- does not play a primary role in the manifestation of an active to passive transition inside the crevice.
- Metal salt solutions typically displayed higher peak current densities as compared to HCl-based solutions of similar calculated pH. From this, it is concluded that metal cation speciation and not pH alone, is responsible for the active to passive transition within crevices of alloy 625.
- From solution speciation calculations, the manifestation of an active to passive transition in alloy 625 was correlated with the concentration of Mo^{3+}. Further, the threshold Mo^{3+} concentration necessary for an active passive transition is between 0.023 m and 0.09 m.
- Based on calculated pH values of solutions that may develop in crevices of nickel alloys C-22, 625, G-3, and C-276, susceptibility to crevice corrosion in these alloys does not appear to be related to the severity of the critical crevice solution that develops in the crevice.

5.2. Precipitation of Metal Oxides within the Crevice

In this study crevice corrosion products from RCAs exposed at immersion times ranging from 18 hours to 2 weeks were examined. The following conclusion were drawn:

- Over time, the crevice corrosion products found inside the crevice became enriched in O, Mo, and Nb content due to the formation of insoluble corrosion products such as MoO_2 and Nb_2O_5.
- Over time, the crevice corrosion products found outside the crevice (around the crevice mouth) became enriched in Ni, Cr, Fe, and Mo, due to the formation of insoluble precipitates such as $Ni(OH)_2$, $Fe(OH)_2$, $Cr(OH)_3$, and MoO_2.
- At early times, the bulk solution was enriched in soluble species such as Ni^{2+} and Fe^{2+}. As time progressed, i.e. from 30 to 60 hours, Ni^{2+} was the main soluble species. By 2 weeks of immersion Cr and Mo insoluble species were found in the bulk solution. The presence of Cr and Mo precipitates is attributed to the high anodic rates near the crevice mouth, causing the precipitation of solids in the bulk solution.
- The active dissolution of alloy 625 follows a stoichiometric dissolution. As soon as the alloy dissolves, the highly soluble cations migrate and diffuse out of the crevice, leaving insoluble crevice corrosion products within the crevice. This is supported by a high relative wt% of the highly soluble cations dissolved in the bulk solution and found in the precipitate around the outside of the crevice mouth.

5.3. Stages of Crevice Corrosion

- Based upon the anodic potentiostatic polarization responses (*I vs t* curves) and crevice corrosion damage morphology, it was proposed that crevice corrosion occurs in three different stages. During Stage I, a CCS develops, and initiation of crevice corrosion occurs near the crevice tip. Two important subsequent events occur during stage I: (*i*) deoxygenation within the crevice, and (*ii*) initiation of crevice corrosion. During Stage II, propagation of crevice corrosion occurs. The active front moves towards the crevice mouth until reaching a distance of maximum approach near the crevice mouth (x_{crit}). During this stage, it was found that the current density and the concentration of the CCS increases as the active front moves towards the crevice mouth. Finally, during stage III, stable crevice corrosion propagation occurs, and crevice corrosion damage commences deeper into the crevice face near the crevice mouth.

- Based on the morphology of crevice corrosion, at early times characterized by low current densities, the formation of a critical crevice solution within the crevice caused the dissolution of the passive film and etching damage was observed. At high current densities, the precipitation of a salt layer occurs, and brightened surfaces were obtained.
- As the applied potential increased, the maximum current value (I_{lim}) also increased. These higher dissolution rates became a key factor for maintaining a critical crevice solution near the crevice mouth.
- The calculated current densities of the active front increases as it moves towards the crevice mouth. The highest current density value is reached at a critical distance near the crevice mouth (x_{crit}).
- Typical crevice gaps of RCAs, were within 20-50 μm. Calculations of *IR*-drop in RCAs based upon these crevice gap values showed that the *IR*-drop along the crevice distance remains small and nearly constant.
- The concentration of the crevice solution increases as the active front moves over time. At some point, the concentration of the solution reaches the saturation limit of 4.4 M, which corresponds to the precipitation of $NiCl_2$.
- For alloy 625, the repassivation potential for crevice corrosion ($E_{rp,crev}$) increased as the crevice damage moved towards the crevice mouth (x_{crit} decreased). Once a minimum x_{crit} near the crevice mouth was reached, $E_{rp,crev}$ remained at a constant value.
- The dependence of $E_{rp,crev}$ on crevice depth was explained by assuming that a critical crevice solution composition inside the crevice was necessary to maintain stable crevice damage propagation. As the active front moves towards the crevice mouth, the crevice depth decreases, and

the current density (dissolution rate of the alloy) needed to maintain a CCS increases. As such, $E_{rp,crev}$ can be defined as the potential at which the dissolution rate is no longer sufficient to maintain a CCS in the face of the diffusion rate at a given distance from the crevice mouth.

BIBLIOGRAPHY

[1] P. Schmuki, "From Bacon to barriers: A review on the passivity of metals and alloys," *J. Solid State Electrochem.*, vol. 6, no. 3, pp. 145–164, 2002.

[2] D. D. Macdonald, "Passivity- the key to our metals-based civilization," *Pure Appl. Chem.*, vol. 71, no. 6, pp. 951–978, 1999.

[3] H. Sun, X. Wu, and E. H. Han, "Effects of temperature on the protective property, structure and composition of the oxide film on Alloy 625," *Corros. Sci.*, vol. 51, no. 11, pp. 2565–2572, 2009.

[4] H. H. Strehblow, "Breakdown of passivity and localized corrosion: Theoretical concepts and fundamental experimental results," *Mater. Corros.*, vol. 35, no. 10, pp. 437–448, 1984.

[5] H. Böhni, "Localized Corrosion of Passive Metals," *Uhlig's Corros. Handb. Third Ed.*, pp. 157–169, 2011.

[6] D. A. Jones, *Principles and Prevention of Corrosion*, 2nd. ed. New Jersey: Pretince Hall, Inc., 1995.

[7] J. Horvath and H. H. Uhlig, "Critical Potentials for Pitting Corrosion of Ni , Cr-Ni , Cr-Fe , and Related Stainless Steels," *J. Electrochem. Soc.*, vol. 115, no. 8, pp. 791–795, 1968.

[8] E. E. Stansbury and R. A. Buchanan, *Fundamentals of Electrochemical Corrosion*. ASM international, 2000.

[9] Z. Szklarska-Smialowska, *Pitting and Crevice Corrosion*. NACE International, 2005.

[10] C. A. C. Sequeira, D. S. P. Cardoso, L. Amaral, B. Šljukić, and D. M. F. Santos, "On the performance of commercially available corrosion-resistant nickel alloys: a review," *Corros. Rev.*, vol. 0, no. 0, pp. 187–200, 2016.

[11] J. S. Lee, R. I. Ray, and B. J. Little, "UNS N06625: A Current Review of the Literature," *Mater. Perform.*, vol. 45, no. 9, pp. 36–40, 2006.

[12] C. Thomas and P. Tait, "The Performance of Alloy 625 in Long-term Intermediate Temperature Applications," *Int. J. Press. Vessel. Pip.*, vol. 59, no. 1–3, pp. 41–49, 1994.

[13] L. R. Davies-Smith, J. D. Lane, and T. Riley, "Effect of Niobium on Marine Crevice Corrosion Resistance of Inconel Alloy 625," *Br. Corros. J.*, vol. 22, no. 2, pp. 90–94, 1987.

[14] E. McCafferty, F. D. Bogar, E. D. Thomas, C. a. Creegan, K. E. Lucas, and a. I. Kaznoff, "Crevice Corrosion Propagation on Alloy 625 and Alloy C276 in Natural Seawater," *Corros.*, vol. 53, no. 10, pp. 755–761, 1997.

[15] H. Alves and U. Heubner, "Aqueous Corrosion of Nickel and its Alloys," *Shreir's Corrosion*. pp. 1879–1915, 2010.

[16] P. Ganesan, C. M. Renteria, and J. R. Crum, "Versatile Corrosion Resistance of INCONEL Alloy 625 in Various Aqueous and Chemical Processing Environments," *The Minerals, Metals & Materials Society*. pp. 663–680, 1991.

[17] X. He and D. S. Dunn, "Crevice Corrosion Penetration Rates of Alloy 22 in Chloride-Containing Waters," *Corrosion*, vol. 63, no. 2, pp. 145–158, 2007.

[18] C. E. Stevens and R. W. Ross, "Production, fabrication, and performance of alloy 625 clad steel for aggressive corrosive environments," *J. Mater. Energy Syst.*, vol. 8, no. 1, pp. 7–16, 1986.

[19] F. G. Hodge and B. E. Wilde, "Effect of Chloride Ion on the Anodic Dissolution Kinetics of Chromium-Nickel Binary Alloys in Dilute Sulfuric Acid," *Corrosion*, vol. 26, no. 6, pp. 246–250, 1970.

[20] M. Moriya and M. B. Ives, "The Structure of Anodic Films Formed on Nickel and Nickel-13 w/o Molybdenum Alloy in pH 2.8 Sodium Sulfate Solution," *Corrosion*, vol. 40, no. 2, pp. 62–72, 1984.

[21] V. Mitrovic-Scepanovic and M. B. Ives, "The Nature of Anodic Films on Nickel and Single Phase Nickel-Molybdenum Alloys," *J. Electrochem. Soc.*, vol. 127, no. 9, pp. 1903–1908, 1980.

[22] R. S. Lillard, M. P. Jurinski, and J. R. Scully, "Crevice Corrosion of Alloy 625 in Chlorinated ASTM Artificial Ocean Water," *Corrosion*, vol. 50, no. 4, pp. 251–265, 1994.

[23] J. R. Hayes, J. J. Gray, A. W. Szmodis, and C. A. Orme, "Influence of Chromium and Molybdenum on the Corrosion of Nickel-Based Alloys," *Corrosion*, vol. 62, no. 6, pp. 491–500, 2005.

[24] P. Jakupi, F. Wang, J. J. Noël, and D. W. Shoesmith, "Corrosion Product Analysis on Crevice Corroded Alloy-22 Specimens," *Corros. Sci.*, vol. 53, no. 5, pp. 1670–1679, 2011.

[25] N. Ebrahimi, P. Jakupi, J. J. Noel, and D. W. Shoesmith, "The Role of Alloying Elements on the Crevice Corrosion Behaviour of Ni-Cr-Mo Alloys," *Corrosion*, vol. 71, no. 12, pp. 1441–1451, 2015.

[26] A. C. Lloyd, J. J. Noël, S. McIntyre, and D. W. Shoesmith, "Cr, Mo and W Alloying Additions in Ni and their Effect on Passivity," *Electrochim. Acta*, vol. 49, pp. 3015–3027, 2004.

[27] W. Z. Friend, *Corrosion of Nickel and Nickel Base Alloys*. New York, 1980.

[28] B. A. Shaw, P. J. Moran, and P. O. Gartland, "The Role of Ohmic Potential Drop in the Initiation of Crevice Corrosion on Alloy 625 in Seawater," *Corros. Sci.*, vol. 32, no. 7, pp. 707–719, 1991.

[29] A. K. Mishra and D. W. Shoesmith, "Effect of Alloying Elements on Crevice Corrosion Inhibition of Nickel-Chromium-Molybdenum-Tungsten Alloys Under Aggressive Conditions: An Electrochemical Study," *Corrosion*, vol. 70, no. 7, pp. 721–730, 2014.

[30] J. W. Oldfield, "Corrosion Initiation and Propagation of Nickel Base Alloys in Severe Sea Water Applications," in *CORROSION/95, Paper No. 266*, 1995.

[31] G. S. Frankel, "Pitting Corrosion of Metals," *J. Electrochem. Soc.*, vol. 145, no. 6, pp. 2186–2198, 1998.

[32] Z. Szklarska-Smialowska, "Mechanism of pit nucleation by electrical breakdown of the passive film," *Corros. Sci.*, vol. 44, no. 5, pp. 1143–1149, 2002.

[33] N. J. Laycock and R. C. Newman, "Localised Dissolution Kinetics, Salt Films and Pitting Potentials," *Corros. Sci.*, vol. 39, no. 10–11, pp. 1771–1790, 1997.

[34] R. B. Inturi and Z. Szklarska-Smialowska, "Dependence of the pitting potential of Al alloys on solubility of alloying element oxides," *Corros. Sci.*, vol. 34, no. 4, pp. 705–710, 1993.

[35] K. Sasaki and G. T. Burstein, "The generation of surface roughness during slurry erosion-corrosion and its effect on the pitting potential," *Corros. Sci.*, vol. 38, no. 12, pp. 2111–2120, 1996.

[36] H. Böhni, "Breakdown of Passivity and Localized Corrosion Processes," *Langmuir*, vol. 3, no. 6, pp. 924–930, 1987.

[37] G. S. Frankel, "On the Pitting Resistance of Sputter-Deposited Aluminum Alloys," *J. Electrochem. Soc.*, vol. 140, no. 8, p. 2192, 1993.

[38] G. T. Gaudet, W. T. Mo, T. A. Hatton, J. W. Tester, and J. Tilly, “Mass Transfer and Electrochemical Kinetic Interactions in Localized Pitting Corrosion,” *AIChE J.*, vol. 32, no. 6, pp. 949–958, 1986.

[39] J. R. Galvele, “Transport Processes and the Mechanism of Pitting of Metals,” *J. Electrochem. Soc.*, vol. 123, no. April, p. 464, 1976.

[40] N. Rashidi, S. Alavi-soltani, and R. Asmatulu, “Crevice Corrosion Theory , Mechanisms and Prevention Methods,” *Proc. 3rd Annu. GRASP Symp.*, pp. 215–216, 2007.

[41] B. G. Ateya and H. W. Pickering, “Significance of the aspect ratio in crevice corrosion,” *Electrochem. Soc. Proc.*, vol. 99, no. 42, pp. 710–715, 1999.

[42] R. G. Kelly, “Crevice Corrosion,” in *ASM Handbook*, vol. 13, 2003, pp. 275–307.

[43] M. G. Fontana and N. D. Greene, *Corrosion Engineering*, Second Edi. New York: McGraw-Hill, 1978.

[44] J. W. Oldfield and W. H. Sutton, “Crevice Corrosion of Stainless Steels I. A mathematical Model,” *Br. Corros. J.*, vol. 13, no. 1, pp. 13–22, 1978.

[45] J. W. Oldfield and W. H. Sutton, “Crevice Corrosion of Stainless Steels: II. Experimental Studies.,” *Br. Corros. J.*, vol. 13, no. 3, pp. 104–111, 1978.

[46] J. W. Oldfield, T. S. Lee, and R. M. Kain, “The Role of Oxygen Reduction and Hydrogen Evolution in Crevice Corrosion of Stainless Steels,” in *Corrosion chemistry within pits, crevices and cracks*, London: HMSO, 1987, pp. 89–105.

[47] J. W. Oldfield and W. H. Sutton, “New Technique for Predicting the Performance of Stainless Steels in Sea Water and Other Chloride-Containing Environments,” *Br. Corros. J.*, vol. 15, no. 1. pp. 31–34, 1980.

[48] H. W. Pickering, “The role of electrode potential distribution in corrosion processes,” *Mater. Sci. Eng.*, vol. 198, pp. 213–223, 1995.

[49] A. Valdes-Moldon, “Thesis,” *Pennsylvania State Univ.*, 1987.

[50] H. W. Pickering, “The Significance of the Local Electrode Potential within Pits, Crevices and Cracks,” *Corros. Sci.*, vol. 29, no. 2–3, pp. 325–341, 1989.

[51] H. W. Pickering, “Important Early Developments and Current Understanding of the IR Mechanism of Localized Corrosion,” *J. Electrochem. Soc.*, vol. 150, no. 5, pp. 1–13, 2003.

[52] K. Cho, M. I. Abdulsalam, and H. W. Pickering, “The Effect of Electrolyte Properties on the Mechanism of Crevice Corrosion in Pure Iron,” *J. Electrochem. Soc.*, vol. 145, no. 6, pp. 1862–1869, 1998.

[53] M. I. Abdulsalam and H. W. Pickering, “Effect of the Applied Potential on the Potential and Current Distributions Within Crevices in Pure Nickel,” *Corros. Sci.*, vol. 41, no. 2, pp. 351–372, 1998.

[54] M. I. Abdulsalam and H. W. Pickering, “The Effect of Crevice-Opening Dimension on the Stability of Crevice Corrosion for Nickel in Sulfuric Acid,” *J. Electrochem. Soc.*, vol. 145, no. 7, pp. 2276–2284, 1998.

[55] H. W. Pickering, K. Cho, and E. Nystrom, “Microscopic and Local Probe Method for Studying Crevice Corrosion and Its Application to Iron and Stainless Steels,” *Corros. Sci.*, vol. 35, no. 1–4, pp. 775–783, 1993.

[56] K. Cho and H. W. Pickering, “The Role of Chloride Ions in the IR>IR* Criterion for Crevice Corrosion in Iron,” *J. Electrochem. Soc.*, vol. 138, no. 10, pp. 56–58, 1991.

[57] P. J. Moran and B. A. Shaw, “Mechanisms of crevice corrosion in chlorinated environments,” 1989.

[58] R. S. Lillard and J. R. Scully, “Modeling of the Factors Contributing to the Initiation and Propagation of the Crevice Corrosion of Alloy 625,” *J. Electrochem. Soc.*, vol. 141, no. 11, pp. 3006–3015, 1994.

[59] M. Watson and J. Postlethwaite, “Numerical simulation of crevice corrosion of stainless steels and nickel alloys in chloride solutions,” *Corrosion*, vol. 46, no. 7, pp. 522–530, 1990.

[60] G. F. Kennell, R. W. Evitts, and K. L. Heppner, “A critical crevice solution and IR drop crevice corrosion model,” *Corros. Sci.*, vol. 50, no. 6, pp. 1716–1725, 2008.

[61] L. Stockert and H. Bohni, “Susceptibility to Crevice Corrosion and Metastable Pitting of Stainless Steels,” *Mater. Sci. Forum*, vol. 44–45, pp. 313–328, 1989.

[62] B. A. Kehler, G. O. Ilevbare, and J. R. Scully, “Crevice Corrosion Stabilization and Repassivation Behavior of Alloy 625 and Alloy 22,” *Corrosion*, vol. 57, no. 12, pp. 1042–1065, 2001.

[63] B. A. Kehler, G. O. Ilevbare, and J. R. Scully, “Comparison of the Crevice Corrosion Resistance of Alloys 625 and C22,” *196th Meet. Electrochem. Soc.*, 1999.

[64] B. A. Kehler and J. R. Scully, “Role of Metastable Pitting in Crevices on Crevice Corrosion Stabilization in Alloys 625 and 22,” *Corrosion*, vol. 61, no. 7, pp. 665–684, 2005.

[65] F. J. Martin, K. E. Lucas, and E. a. Hogan, “Experimental procedure for crevice corrosion studies of Ni-Cr-Mo alloys in natural seawater,” *Rev. Sci. Instrum.*, vol. 73, no. 3 I, p. 1273, 2002.

[66] F. J. Martin, P. M. Natishan, K. E. Lucas, E. a. Hogan, a. M. Grolleau, and E. D. Thomas, “Crevice corrosion of alloy 625 in natural seawater,” *Corrosion*, vol. 59, no. 6, pp. 498–504, 2003.

[67] X. Shan and J. H. Payer, “Characterization of the Corrosion Products of Crevice Corroded Alloy 22,” *J. Electrochem. Soc.*, vol. 156, no. 9, pp. C313–C321, 2009.

[68] F. Bocher, F. Presuel-Moreno, N. D. Budiansky, and J. R. Scully, “Coupled multielectrode investigation of crevice corrosion of AISI 316 stainless steel,” *Electrochem. Solid State Lett.*, vol. 10, no. 3, pp. C16–C20, 2007.

[69] F. Bocher, F. Presuel-Moreno, and J. R. Scully, “Investigation of Crevice Corrosion of AISI 316 Stainless Steel Compared to Ni–Cr–Mo alloys Using Coupled Multi-electrode Arrays,” *J. Electrochem. Soc.*, vol. 155, no. 5, pp. C256–C268, 2008.

[70] N. D. Budiansky, F. Bocher, H. Cong, M. F. Hurley, and J. R. Scully, “Use of Coupled Multi-Electrode Arrays to Advance the Understanding of Selected Corrosion Phenomena,” *Corrosion*, vol. Conference, no. 6677, 2006.

[71] F. Bocher, R. Huang, and J. R. Scully, “Prediction of Critical Crevice Potentials for Ni-Cr-Mo Alloys in Simulated Crevice Solutions as a Function of Molybdenum Content,” *Corrosion*, vol. 66, no. 5, pp. 55002-1-55002–15, 2010.

[72] J. Mankowski and Z. Szklarska-Smialowska, “Studies on accumulation of chloride ions in pits growing during anodic polarization,” *Corros. Sci.*, vol. 15, no. 6–12, pp. 493–501, 1975.

[73] P. Wang, A. Anderko, and R. D. Young, “A speciation-based model for mixed-solvent electrolyte systems,” *Fluid Phase Equilib.*, vol. 203, no. 1–2, pp. 141–176, 2002.

[74] P. Wang, R. D. Springer, A. Anderko, and R. D. Young, “Modeling phase equilibria and speciation in mixed-solvent electrolyte systems,” *Fluid Phase Equilib.*, vol. 222–223, pp. 11–17, 2004.

[75] P. Wang, A. Anderko, R. D. Springer, and R. D. Young, “Modeling phase equilibria and speciation in mixed-solvent electrolyte systems: II. Liquid-liquid equilibria and properties of associating electrolyte solutions,” *J. Mol. Liq.*, vol. 125, no. 1, pp. 37–44, 2006.

[76] C. C. Chen and L. B. Evans, “A local composition model for the excess Gibbs energy of aqueous

electrolyte systems," *AIChE J.*, vol. 32, no. 3, pp. 444–454, 1986.

[77] V. Abovsky, Y. Liu, and S. Watanasiri, "Representation of nonideality in concentrated electrolyte solutions using the Electrolyte NRTL model with concentration-dependent parameters," *Fluid Phase Equilib.*, vol. 150–151, pp. 277–286, 1998.

[78] B. Sander, A. Fredenslund, and P. Rasmussen, "Calculation of vapour-liquid equilibria in mixed solvent/salt systems using an extended UNIQUAC equation," *Chem. Eng. Sci.*, vol. 41, no. 5, pp. 1171–1183, 1986.

[79] E. A. Macedo, P. Skovborg, and P. Rasmussen, "Calculation of phase equilibria for solutions of strong electrolytes in solvent-water mixtures," *Chem. Eng. Sci.*, vol. 45, no. 4, pp. 875–882, 1990.

[80] M. C. Iliuta, K. Thomsen, and P. Rasmussen, "Extended UNIQUAC model for correlation and prediction of vapour-liquid-solid equilibria in aqueous salt systems containing non-electrolytes. Part A. methanol-water-salt systems," *Chem. Eng. Sci.*, vol. 55, no. 14, pp. 2673–2686, 2000.

[81] J. Li, H.-M. Polka, and J. Gmehling, "A gE model for single and mixed solvent electrolyte systems 1. Model and results for strong electrolytes," *Fluid Phase Equilib.*, vol. 94, no. 1922, pp. 89–114, 1994.

[82] F. J. Martin and P. M. Natishan, "Metallurgical and morphological considerations for seawater crevice corrosion of alloy 625," *Electrochem. Soc. Proc.*, vol. 14, pp. 311–318, 2004.

[83] J. W. Oldfield, "Test techniques for pitting and crevice corrosion resistance of stainless and nickel-base alloys in chloride containing environments," *Nickel Dev. Inst.*, vol. 32, no. 3, 1987.

[84] "ASTM Standard G78, 2015, Standard Guide for Crevice Corrosion Testing of Iron-Base and Nickel-Base Stainless Alloys in Seawater and Other Chloride-Containing Aqueous Environments." ASTM International, West Conshohocken, PA, 2015.

[85] J. W. Oldfield, "Crevice Corrosion of Stainless Steels - The importance of Crevice Geometry and Alloy Composition," *Bull. du Cercle d'Etudes des Metaux*, vol. 14, no. 9, pp. 134–147, 1980.

[86] R. M. Kain and T. S. Lee, "Recent developments in test methods for investigating crevice corrosion," in *Laboratory Corrosion Tests and Standards*, vol. ASTM STP 8, G. S. H. and R. Baboian, Ed. West Conshohocken, PA: ASTM International, 1985, pp. 299–323.

[87] T. S. Lee, "A method for quantifying the initiation and propagation stages of crevice corrosion," *Electrochem. Corros. Testing, ASTM STP*, vol. 727, pp. 43–68, 1981.

[88] P. Jakupi, J. J. Noel, and D. W. Shoesmith, "Crevice corrosion initiation and propagation on Alloy-22 under galvanically-coupled and galvanostatic conditions," *Corros. Sci.*, vol. 53, no. 10, pp. 3122–3130, 2011.

[89] K. G. Mon, P. Pasupathi, A. Yilmaz, and R. B. Rebak, "Stifling of Crevice Corrosion in Alloy 22 During Constant Potential Tests," *Lawrnce Livemore Natl. Lab.*, 2005.

[90] M. A. Rodríguez, R. M. Carranza, and R. B. Rebak, "Effect of potential on crevice corrosion kinetics of alloy 22," *Corrosion*, vol. 66, no. 1, pp. 0150071–01500714, 2010.

[91] K. J. Evans, A. Yilmaz, S. D. Day, L. L. Wong, J. C. Estill, and R. B. Rebak, "Using electrochemical methods to determine alloy 22's crevice corrosion repassivation potential," *Jom*, vol. 57, no. 1, pp. 56–61, 2005.

[92] D. S. Dunn, N. Sridhar, and G. A. Cragnolino, "Long-Term Prediction of Localized Corrosion of Alloy 825 in High-Level Nuclear Waste Repository Environments," *Corros.*, vol. 52, no. 2, pp. 115–124, 1996.

[93] B. E. Wilde and E. Williams, "The use of current/voltage curves for the study of localized corrosion

and passivity breakdown on stainless steels in chloride media," *Electrochim. Acta*, vol. 16, no. 11, pp. 1971–1985, 1971.

[94] "ASTM Standard G61, 1986 (2014), Standard Test Method for Conducting Cyclic Potentiodynamic Polarization Measurements for Localized Corrosion Susceptibility of Iron-, Nickel-, or Cobalt-Based Alloys." ASTM International, West Conshohocken, PA, 2014.

[95] R. Baboian, Ed., *Corrosion Tests and Standards: Application and Interpretation*, 2nd editon. West Conshohocken, PA: ASTM international, 2005.

[96] S. Tsujikawa and Y. Hisamatsu, "On the Repassivation Potential for Crevice Corrosion," *Boshoku Gijutsu (Corrosion Eng.*, vol. 29, pp. 37–40, 1980.

[97] K. J. Evans, L. L. Wong, and R. B. Rebak, "Determination of the crevice repassivation potential of alloy 22 by a potentiodynamic-galvanostatic-potentiostatic method," *Transp. Storage, Dispos. Radioact. Mater.*, vol. 483, pp. 137–149, 2004.

[98] "ASTM Standard G192, 2008 (2014), Standard Test Method for Determining the Crevice Repassivation Potential of Corrosion-Resistant Alloys Using a Potentiodynamic-Galvanostatic-Potentiostatic Technique." ASTM International, West Conshohocken, PA, 2014.

[99] "ASTM Standard G48, 2011 (2015), Standard Test Methods for Pitting and Crevice Corrosion Resistance of Stainless and Related Alloys by Use of Ferric Chloride Solution." ASTM Internaltional, West Conshohocken, PA, 2015.

[100] "ASTM Standard D1141, 1998 (2013), Standard Practice for the Preparation of Substitute Ocean Water." ASTM International, West Conshohocken, PA, 2013.

[101] H. Villarraga-Gómez, "X-ray Computed Tomography for Dimensional Measurements," *Digital Imaging 2016*, no. October. pp. 44–57, 2016.

[102] A. Ramsey and H. Villarraga-Gómez, "The inspection and quality control of metal AM parts with X-ray Computed Tomography (micro CT)," *Met. Addit. Manuf.*, vol. 3, no. 2, pp. 1–7, 2017.

[103] N. Sato, "The stability of pitting dissolution of metals in aqueous solution," *J. Electrochem. Soc.*, vol. 129, no. 2, pp. 260–264, 1982.

[104] M. Datta and D. Landolt, "On the Role of Mass Transport in High Rate Dissolution of Iron and Nickel in ECM electrolytes—I. Chloride Solutions," *Electrochim. Acta*, vol. 25, no. 10, pp. 1255–1262, 1980.

[105] A. Stenta *et al.*, "Species-Dependent Crevice Corrosion Modeling of Ni-625," *Corrosion*, vol. 72, no. 11, pp. 1328–1341, 2016.

[106] A. J. Stenta, "Species-Dependent Modeling Of Crevice Corrosion Systems." The University of Akron (Dissertation), Akron, OH, p. 242, 2015.

[107] G. Karlberg and G. Wranglen, "On the mechanism of crevice corrosion of stainless Cr steels," *Corros. Sci.*, vol. 11, no. 7, pp. 499–510, 1971.

[108] J. Soltis, "Passivity breakdown, pit initiation and propagation of pits in metallic materials - Review," *Corros. Sci.*, vol. 90, pp. 5–22, 2015.

[109] S. J. Mulford and D. Tromans, "Crevice Corrosion of Nickel-Based Alloys in Neutral Chloride and Thiosulfate Solutions," *Corrosion*, vol. 44, no. 12, pp. 891–900, 1988.

[110] J. W. Tester and H. S. Isaacs, "Diffusional Effects in Simulated Localized Corrosion," *J. Electrochem. Soc.* , vol. 122, no. 11, pp. 1438–1445, 1975.

[111] J. Srinivasan and R. G. Kelly, "One-Dimensional Pit Experiments and Modeling to Determine

Critical Factors for Pit Stability and Repassivation," *J. Electrochem. Soc.*, vol. 163, no. 13, pp. C759–C767, 2016.

[112] J. Srinivasan, M. J. Mcgrath, and R. G. Kelly, "A High-Throughput Artificial Pit Technique to Measure Kinetic Parameters for Pitting Stability," *J. Electrochem. Soc.*, vol. 162, no. 14, pp. 725–731, 2015.

[113] H. S. Isaacs, "The Behavior of Resistive Layers in the Localized Corrosion of Stainless Steel," *J. Electrochem. Soc.*, vol. 120, no. 11, p. 1456, 1973.

[114] H. W. Pickering and R. P. Frankenthal, "On the Mechanism of Localized Corrosion of Iron and Stainless Steel I. Electrochemical Studies," *J. Electrochem. Soc.*, vol. 119, no. 10, pp. 1297–1304, 1972.

[115] R. P. Frankenthal and H. W. Pickering, "On the Mechanism of Localized Corrosion of Iron and Stainless Steel II. Morphological Studies," *J. Electrochem. Soc.*, vol. 119, no. 10, pp. 1304–1310, 1972.

[116] H. S. Isaacs, "In Situ X-Ray Microprobe Study of Salt Layers during Anodic Dissolution of Stainless Steel in Chloride Solution," *J. Electrochem. Soc.*, vol. 142, no. 4, p. 1111, 1995.

[117] N. Sridhar and D. S. Dunn, "In situ study of salt film stability in simulated pits of nickel by Raman and electrochemical impedance spectroscopies," *J. Electrochem. Soc.*, vol. 144, no. 12, pp. 4243–4253, 1997.

[118] C. S. Brossia, D. S. Dunn, and N. Sridhar, "The Role of Metal Salt Film Formation on Localized Corrosion Stabilization," *Cent. Nucl. Waste Regul. Anal.*

[119] M. Datta and D. Landolt, "Surface Brightening during High Rate Nickel Dissolution in Nitrate Electrolytes," *J. Electrochem. Soc.*, vol. 122, no. 11, pp. 1466–1472, 1975.

[120] J. Srinivasan, C. Liu, and R. G. Kelly, "Geometric Evolution of Flux from a Corroding One-Dimensional Pit and Its Implications on the Evaluation of Kinetic Parameters for Pit Stability," *J. Electrochem. Soc.*, vol. 163, no. 10, pp. C694–C703, 2016.

[121] N. Sato, "The Stability of Localized Corrosion," *Corros. Sci.*, vol. 37, no. 12, pp. 1947–1967, 1995.